

**MICROSTRUCTURAL VISCO-ELASTIC MODELS FOR
CARBONATES AND RELATED POROUS MEDIA**

Nassir Omardeen Osman



Thesis for the degree of Master
of Reservoir Geophysics

Department of Earth Science

University of Bergen

February 23, 2021

Abstract

Rock physics modelling and inversion is indispensable in reservoir characterization and beyond. Microstructural models can be implemented to explain the measured real field visco-elastic properties of both carbonates and other porous media. This work presents both synthetic and real data inversion, and aims to evaluate microstructural visco-elastic models for carbonates, and further implement simulated annealing (SA) in rock physics and investigate.

On account of that, visco-elastic generalized Xu-White model is been employed, for forward modelling, in which different perturbations in the microstructural parameters has been performed. This has been effectively employed to obtain the ultimate match with the real data, presented in this thesis. Dynamic version of the T-matrix that use a Lippmann-Schwinger type of integral and consistent with the Brown-Korringa relation, has been employed to count for the frequency-dependent effects of the fully saturated communicating, inclusion of, cavities. The swift variant of SA called Very Fast Simulated Annealing (VFSA) is been used to minimize the data mismatch.

The forward modelling results corresponding to different perturbations in the microstructural parameters can lead to optimum understanding of the behaviour of the microstructural models. Since VFSA coefficients must be selected in a proper way, upper and lower bounds of the microstructural initial model has been selected, to optimally perform the synthetic inversion models. Several models has been evaluated and their ability to explain the measured velocity and attenuations of P- and S-waves at sonic and ultrasonic frequencies. Model error test (ME) and uncertainty estimation, has been investigated to obtain the optimal understanding of the complexity, associated with carbonates. After all, only the real data inversion of the Portland top, using four different pore-types, showed the power of VFSA in the rock physics inversion, and that it can provide quite good match to real data.

Acknowledgments

This master's thesis was conducted at the Department of Earth Science, the Faculty of Mathematics and Natural Sciences, at the University of Bergen.

First of all, I would like to express my sincere gratitude and recognition to Prof. Morten Jakobsen, who supervised me professionally during my MSc degree. Prof. Jakobsen also provided me with the Matlab code that has been used to produce most of the results. Thank you for allowing me to learn from and to modify on your Matlab code. A great appreciation to Professor Clive McCann and experimental rock physicist Jeremy Sothcott for the permission to use the real data. I am grateful that you made the opportunity to have an empirical input parameters, in my thesis, possible. Thank you very much.

To my friend, Mahmoud ElTayieb, thank you for all the great support, I admired the learning environment that I realized because of you. Big thanks to Mr. Jonas Holm Erstad and my friend Aung Htun Lin for all the beneficial discussions and for proofreading my thesis.

I would like to recognize the emotional and moral affirmation from my parents. Finally, I also acknowledge the support that my wife offered me.

Bergen, February 23, 2021

Nassir Osman

Preface

The admission of this thesis, originally, is intended to be on reservoir geology in the PTEK-program from the Department of Physics and Technology, however I was given the supervisor in the Geophysics-group of the Department of the Earth Science at the University of Bergen. The work presented in this thesis is more geophysics than geology, however rock physics is, in fact, at the intersection of this two disciplines.

Last but not least, I would like to thank the Department of Physics and Technology for the admission and the great people on the administration of the university for all the technical guidances, which made this work possible.

Bergen, February 23, 2021

Nassir Osman

Contents

1	Introduction	1
1.1	Carbonates and Related Porous Media	1
1.2	Sonic and Ultrasonic Measurements on Carbonates	2
1.2.1	Sample Description	2
1.2.2	Velocity and Attenuation Measurements	3
1.3	Microstructural Visco-elastic Models	7
1.4	Rock Physics Modelling and Inversion	9
1.5	Applications to Seismic Reservoir Characterization	12
1.6	Main goals, Scope of the work, and Outline	12
1.6.1	Main Goals and Motivation	12
1.6.2	Scope of the Work and Limitations	13
1.6.3	Thesis Outline	13
2	Rock Physics Modelling	15
2.1	T-matrix Approach to Effective Stiffnesses	15
2.2	Visco-elastic Effects due to Squirt Flow	17
2.2.1	Fluid Substitution	20
2.3	Numerical Results and Discussion	21
2.3.1	Models with Two Different Pore-Types	21
2.3.2	Fluid Substitution of Model with Two Pore-Type	24
2.3.3	Models with Three Pore-Types	24
2.3.4	Fluid Substitution of Model with Three Pore-Type	25
2.4	Concluding Remarks	25
3	Rock Physics Inversion	59
3.1	The Non-linear Inverse Problem	59
3.2	Optimization by Simulated Annealing	60
3.3	Inversion of Synthetic Data	63

3.3.1	Inversion using Two Pore-type	64
3.3.2	Inversion using Three Pore-type	67
3.4	Inversion of Real Data	67
3.4.1	Inversion using Two Different Pore-Type	67
3.4.2	Inversion using Three Different Pore-Type	69
3.4.3	Inversion using Four Different Pore-Type	70
4	Discussion, Conclusions and Suggestions for Future Work	101
4.1	Discussion	101
4.2	Conclusions	102
4.3	Suggestions for Future Work	103
	Appendices	107
A	The G-tensor	107
B	Orientation averaging	108

List of Figures

- 1.1 SEM of the Portland limestone sample, the sample is an Oolitic porous grain-stone with large inter-granular pores and blocky calcite cement between the ooids. The ooids are rounded to sub-rounded, 250 – 750 μm in diameter. **a)** Lower power of the sample, at the scale of 100 μm , showing the matrix made of ooids, large inter-granular pores and the local cement and **b)** Close up of the sample, at the scale of 10 μm , showing the ooids made of microspar with abundant porosity (Jakobsen et al., 2021). 3

- 1.2 The resonant bar apparatus: a) Pressure apparatus used to subject the samples to elevated temperatures and hydrostatic confining pressure and to regulate the sample pore fluid pressure. b) Block diagram of electronic apparatus used for resonant rod measurements.(need reference) 4

- 1.3 The pulse-echo method: a) Schematic diagram of the pulse-echo (reflection) method for measuring attenuation. b) Examples of P and S-wave pulse traces, where TR denotes sample-top reflection, BR denotes sample-bottom reflection, SMR denotes sample multiple reflection, and BMR denotes buffer multiple reflection (Assefa et al., 1999). 5

- 1.4 Measured data of the Portland limestone (top) sample at sonic and ultrasonic frequencies as in table 1.1: (a) P-wave velocity (red triangle) and S-wave velocity (blue squares),(b) P-wave attenuation (red triangle) and S-wave attenuation (blue squares). The errorbars, red (p-wave), blue (S-wave) represent the probability distribution, with the middle data value in the middle of it. 8

1.5	<p>Sketched illustration of the models with different sets of communicating cavities: a) the pores are connected to each other ($\alpha_1 = 0.15$ and $\alpha_2 = 0.05$), b) the complexity of this model has been increased, by adding a flatter compliant ($\alpha_3 = 0.001$) to the model in (a), again, the pores are connected to each other, c) a new sets of compliant pore is added (pore type 4), pore type 4 are connected to each other (with dashed lines), however, isolated with respect to pore types 1-3. While pore types 1-3 are connected to each other, but isolated with respect to pore type 4.</p>	10
1.6	<p>Wave induced fluid flow (squirt flow) caused by a seismic wave propagation, using a model of two layers: a) two layer velocity model b) acoustic wave propagation from a shot point (red star), for the sake of simplicity constant density was assumed c) a representative volume element, used as the effective homogeneous medium d) the real heterogeneous medium (micro scale) of the model at time t, demonstrating the squirt flow mechanism, in which the fluid flow from the compliant soft pores (pore type 2) to the more rounded stiffer pores (pore type 1).</p>	11
1.7	<p>Simulate annealing minimization and its criteria of finite probability of jumping out of local minima, and, simultaneously, settle into the global minimum.</p>	11
2.1	<p>Theoretical predictions of the velocity and attenuation spectra of a rock model with two types of pores, versus synthetic data. This is the reference model (Xu-White model), and it is water saturated. The model parameters are: [$\alpha_1 = 0.15, \alpha_2 = 0.05, \phi_2 = 0.00556, \tau_1 = \tau_2 = 1 \times 10^{-7}$ s].</p>	26
2.2	<p>The effect of a negative perturbation of α_2 on the velocity and attenuation spectra of a rock model with two types of pores, using Xu and White model as a reference model, with model parameters of: [$\alpha_1 = 0.15, \alpha_2 = 0.0375, \phi_2 = 0.0056, \tau_1 = \tau_2 = 1 \times 10^{-7}$ s].</p>	27

2.3	The minimum perturbation of α_2 , and how it affects the velocity and attenuation spectra of a rock model with two types of pores, using Xu and White model as a reference model, with model parameters of [$\alpha_1 = 0.15, \alpha_2 = 0.025, \phi_2 = 0.00556, \tau_1 = \tau_2 = 1 \times 10^{-7}$ s].	28
2.4	The effect of a positive perturbation of α_2 on the velocity and attenuation spectra of a rock model with two types of pores, using Xu and White model as a reference model, with model parameters of [$\alpha_1 = 0.15, \alpha_2 = 0.0625, \phi_2 = 0.00556, \tau_1 = \tau_2 = 1 \times 10^{-7}$ s].	29
2.5	The maximum perturbation of α_2 , and how it affects the velocity and attenuation spectra of a rock model with two types of pores, using Xu and White model as a reference model, with model parameters of [$\alpha_1 = 0.15, \alpha_2 = 0.075, \phi_2 = 0.00556, \tau_1 = \tau_2 = 1 \times 10^{-7}$ s].	30
2.6	The effect of a negative perturbation of α_1 on the velocity and attenuation spectra of a rock model with two types of pores, using Xu and White model as a reference model, with model parameters of [$\alpha_1 = 0.1125, \alpha_2 = 0.05, \phi_2 = 0.00556, \tau_1 = \tau_2 = 1 \times 10^{-7}$ s].	31
2.7	The minimum perturbation of α_1 , and how it affects the velocity and attenuation spectra of a rock model with two types of pores, using Xu and White model as a reference model, with model parameters of [$\alpha_1 = 0.075, \alpha_2 = 0.05, \phi_2 = 0.00556, \tau_1 = \tau_2 = 1 \times 10^{-7}$ s].	32
2.8	The effect of a positive perturbation of α_1 on the velocity and attenuation spectra of a rock model with two types of pores, using Xu and White model as a reference model, with model parameters of [$\alpha_1 = 0.1875, \alpha_2 = 0.05, \phi_2 = 0.00556, \tau_1 = \tau_2 = 1 \times 10^{-7}$ s].	33
2.9	The maximum perturbation of α_1 , and how it affects the velocity and attenuation spectra of a rock model with two types of pores, using Xu and White model as a reference model, with model parameters of [$\alpha_1 = 0.225, \alpha_2 = 0.05, \phi_2 = 0.00556, \tau_1 = \tau_2 = 1 \times 10^{-7}$ s].	34

2.10	The effect of a negative perturbation of ϕ_2 on the velocity and attenuation spectra of a rock model with two types of pores, using Xu and White model as a reference model, with model parameters of $[\alpha_1 = 0.15, \alpha_2 = 0.05, \phi_2 = 0.00417, \tau_1 = \tau_2 = 1 \times 10^{-7} \text{ s}]$	35
2.11	The minimum perturbation of ϕ_2 on the velocity and attenuation spectra of a rock model with two types of pores, using Xu and White model as a reference model, with model parameters of $[\alpha_1 = 0.15, \alpha_2 = 0.05, \phi_2 = 0.00278, \tau_1 = \tau_2 = 1 \times 10^{-7} \text{ s}]$	36
2.12	Illustration of the effect of a positive perturbation of ϕ_2 on the velocity and attenuation spectra of a rock model with two types of pores, using Xu and White model as a reference model, with model parameters of $[\alpha_1 = 0.15, \alpha_2 = 0.05, \phi_2 = 0.00696, \tau_1 = \tau_2 = 1 \times 10^{-7} \text{ s}]$	37
2.13	Illustration of the effect of the maximum perturbation of ϕ_2 on the velocity and attenuation spectra of a rock model with two types of pores, using Xu and White model as a reference model, with model parameters of $[\alpha_1 = 0.15, \alpha_2 = 0.05, \phi_2 = 0.0075, \tau_1 = \tau_2 = 1 \times 10^{-7} \text{ s}]$	38
2.14	The effect of a negative perturbation of both τ_1 and τ_2 on the velocity and attenuation spectra of a rock model with two types of pores, using Xu and White model as a reference model, with model parameters of $[\alpha_1 = 0.15, \alpha_2 = 0.05, \phi_2 = 0.00556, \tau_1 = \tau_2 = 0.3 \times 10^{-7} \text{ s}]$	39
2.15	The minimum perturbation of τ_1 and τ_2 , and how it affect the velocity and attenuation spectra of a rock model with two types of pores, using Xu and White model as a reference model, with model parameters of $[\alpha_1 = 0.15, \alpha_2 = 0.05, \phi_2 = 0.00556, \tau_1 = 1 \times 10^{-8} \text{ s}, \tau_2 = 1 \times 10^{-8} \text{ s}]$	40
2.16	Illustration of the effect of a positive perturbation of τ_1 and τ_2 on the velocity and attenuation spectra of a rock model with two types of pores, using Xu and White model as a reference model, with model parameters of $[\alpha_1 = 0.15, \alpha_2 = 0.05, \phi_2 = 0.00556, \tau_1 = \tau_2 = 3 \times 10^{-7} \text{ s}]$	41

2.17	Illustration of the effect of the maximum perturbation of τ_1 and τ_2 on the velocity and attenuation spectra of a rock model with two types of pores, using Xu and White model as a reference model, with model parameters of $[\alpha_1 = 0.15, \alpha_2 = 0.05, \phi_2 = 0.00556, \tau_1 = 1 \times 10^{-6} \text{ s}, \tau_2 = 1 \times 10^{-6} \text{ s}]$. . .	42
2.18	The effect of a negative perturbation of τ_1 on the velocity and attenuation spectra of a rock model with two types of pores, using Xu and White model as a reference model, with model parameters of $[\alpha_1 = 0.15, \alpha_2 = 0.05, \phi_2 = 0.00556, \tau_1 = 0.3 \times 10^{-7} \text{ s}, \tau_2 = 1 \times 10^{-7} \text{ s}]$	43
2.19	The minimum perturbation of τ_1 , and how it affects the velocity and attenuation spectra of a rock model with two types of pores, using Xu and White model as a reference model, with model parameters of $[\alpha_1 = 0.15, \alpha_2 = 0.05, \phi_2 = 0.00556, \tau_1 = 1 \times 10^{-8} \text{ s}, \tau_2 = 1 \times 10^{-7} \text{ s}]$	44
2.20	The effect of a positive perturbation of τ_1 on the velocity and attenuation spectra of a rock model with two types of pores, using Xu and White model as a reference model, with model parameters of $[\alpha_1 = 0.15, \alpha_2 = 0.05, \phi_2 = 0.00556, \tau_1 = 3 \times 10^{-7} \text{ s}, \tau_2 = 1 \times 10^{-7} \text{ s}]$	45
2.21	The maximum perturbation of τ_1 , and how it affects the velocity and attenuation spectra of a rock model with two types of pores, using Xu and White model as a reference model, with model parameters of $[\alpha_1 = 0.15, \alpha_2 = 0.05, \phi_2 = 0.00556, \tau_1 = 1 \times 10^{-6} \text{ s}, \tau_2 = 1 \times 10^{-7} \text{ s}]$	46
2.22	Illustration of the effect of a negative perturbation of τ_2 on the velocity and attenuation spectra of a rock model with two types of pores, using Xu and White model as a reference model, with model parameters of $[\alpha_1 = 0.15, \alpha_2 = 0.05, \phi_2 = 0.00556, \tau_1 = 1 \times 10^{-7} \text{ s}, \tau_2 = 0.3 \times 10^{-7} \text{ s}]$	47
2.23	Illustration of the effect of the minimum perturbation of τ_2 on the velocity and attenuation spectra of a rock model with two types of pores, using Xu and White model as a reference model, with model parameters of $[\alpha_1 = 0.15, \alpha_2 = 0.05, \phi_2 = 0.00556, \tau_1 = 1 \times 10^{-7} \text{ s}, \tau_2 = 1 \times 10^{-8} \text{ s}]$	48

2.24	The effect of a positive perturbation of τ_2 on the velocity and attenuation spectra of a rock model with two types of pores, using Xu and White model as a reference model, with model parameters of $[\alpha_1 = 0.15, \alpha_2 = 0.05, \phi_2 = 0.00556, \tau_1 = 1 \times 10^{-7} \text{ s}, \tau_2 = 3 \times 10^{-7} \text{ s}]$	49
2.25	The maximum perturbation of τ_2 , and how it affects the velocity and attenuation spectra of a rock model with two types of pores, using Xu and White model as a reference model, with model parameters of $[\alpha_1 = 0.15, \alpha_2 = 0.05, \phi_2 = 0.00556, \tau_1 = 1 \times 10^{-7} \text{ s}, \tau_2 = 1 \times 10^{-6} \text{ s}]$	50
2.26	Theoretical predictions of the velocity and attenuation spectra of a water saturated rock model with three types of pores, this is the reference model, which the vico-elastic generalized Xu and White model $[\alpha_1 = 0.15, \alpha_2 = 0.05, \alpha_3 = 0.001 \phi_2 = 0.00556, \phi_3 = \alpha_3/10, \tau_1 = \tau_2 = \tau_3 = 1 \times 10^{-7} \text{ s}]$	51
2.27	The effect of a negative perturbation of α_3 on the velocity and attenuation spectra of a rock model with three types of pores, using more complex Xu and White model, with model parameters of $[\alpha_1 = 0.15, \alpha_2 = 0.05, \alpha_3 = 0.00075 \phi_2 = 0.00556, \phi_3 = \alpha_3/10, \tau_1 = \tau_2 = \tau_3 = 1 \times 10^{-7} \text{ s}]$	52
2.28	The effect of the minimum negative perturbation of α_3 on the velocity and attenuation spectra of a rock model with three types of pores, using more complex Xu and White model, with model parameters of $[\alpha_1 = 0.15, \alpha_2 = 0.05, \alpha_3 = 0.0005 \phi_2 = 0.00556, \phi_3 = \alpha_3/10, \tau_1 = \tau_2 = \tau_3 = 1 \times 10^{-7} \text{ s}]$	53
2.29	The effect of a positive perturbation of α_3 on the velocity and attenuation spectra of a rock model with three types of pores, using more complex Xu and White model, with model parameters of $[\alpha_1 = 0.15, \alpha_2 = 0.05, \alpha_3 = 0.00125 \phi_2 = 0.00556, \phi_3 = \alpha_3/10, \tau_1 = \tau_2 = \tau_3 = 1 \times 10^{-7} \text{ s}]$	54
2.30	The maximum positive perturbation of α_3 , and how it affects the velocity and attenuation spectra of a rock model with three types of pores, using more complex Xu and White model, with model parameters of $[\alpha_1 = 0.15, \alpha_2 = 0.05, \alpha_3 = 0.0015 \phi_2 = 0.00556, \phi_3 = \alpha_3/10, \tau_1 = \tau_2 = \tau_3 = 1 \times 10^{-7} \text{ s}]$	55

2.31	Pore-fluid substitution effects, when substituting water with oil for the model of two pore types. The reference model in the water saturated visco-elastic model shown in Figure 2.1.	56
2.32	Fluid substitution effects, when substituting water with oil for the model of three pore types. The reference model in the water saturated visco-elastic model shown in Figure 2.26.	57
3.1	The true model of two pore-types with, and without noise. Synthetic data are plotted as dots in the middle of the errorbars, red (p-wave), blue (S-wave). The errorbars, red (p-wave), blue (S-wave) represent the probability distribution, with the median data value in the middle of it. Using the model parameters in Table 3.1.	73
3.2	Illustration of the initial model used in the data inversion by VFSA. Synthetic data are plotted as dots in the middle of the error bars, red (p-wave), blue (S-wave). The errorbars, red (p-wave), blue (S-wave) represent the probability distribution, with the median data value in the middle of it. For the model parameters see Table 3.1.	74
3.3	The inverted model by VFSA, for model of two pore types. Synthetic data are plotted as dots in the middle of the errorbars, red (p-wave), blue (S-wave). The errorbars, red (p-wave), blue (S-wave) represent the probability distribution, with the median data value in the middle of it. The true model is in Figure 3.1, and the initial model is in Figure 3.2, for the model parameters see Table 3.1.	75
3.4	Illustration of the number of iterations and the behaviour of the objective function, and cooling process (temperature curve) for the model in Figure 3.3 above.	76

3.5	Inverted of the model with noise, for the same model in Figure 3.3. Synthetic data are plotted as dots in the middle of the error bars, red (p-wave), blue (S-wave). The errorbars, red (p-wave), blue (S-wave) represent the probability distribution, with the middle data value (data without noise) in the center of it. Here, noise realization is shown by the black and magenta dotes for the P-wave and S-wave spectra, respectively, for the model parameters see Table 3.2.	77
3.6	Illustration of the number of iterations and the behaviour of the objective function, and cooling process (temperature curve) for the model in Figure 3.5 above.	78
3.7	True model, the model is with three sets of pores. The errorbars, red (p-wave), blue (S-wave) represent the probability distribution, with the middle data value in the middle of it. Synthetic data are plotted as dots in the middle of the errorbars, red (p-wave), blue (S-wave). The model parameters are in Table 3.3.	79
3.8	The initial model for the model with three sets of pores. Synthetic data are plotted as dots in the middle of the errorbars, red (p-wave), blue (S-wave). A comparison between synthetic data (data with errorbars) and theoretical predictions of the velocity and attenuation spectra of a rock model with three sets of pores. Model parameters are in Table 3.3.	80
3.9	The model error estimation, when the three pore-types model inverted by model with two-pores. Synthetic data are plotted as dots in the middle of the errorbars, red (p-wave), blue (S-wave). The errorbars, red (p-wave), blue (S-wave) represent the probability distribution, with the median data value in the middle of it. The true model and initial model are in Figure 3.7, and Figure 3.8, respectively. The model parameters are in Table 3.3.	81
3.10	Illustration of the number of iterations needed by VFSA, the behaviour of the objective function, and cooling process (temperature curve)for the model in Figure 3.9 above.	82

3.11	The inverted model, for model of three pore types. Using the same true model in figure 3.9. Synthetic data are plotted as dots in the middle of the errorbars, red (p-wave), blue (S-wave). The errorbars, red (p-wave), blue (S-wave) represent the probability distribution, with the median data value in the middle of it. The theoretical predictions of both models are based on a microstructural visco-elastic model of communicating cavities with different pore shapes and scales, using the model parameters in Table 3.4.	83
3.12	Illustration of the number of iterations needed by VFSA, the behaviour of the objective function, and cooling process (temperature curve) for the model in Figure 3.11 above.	84
3.13	The inverted model with noise added, for the three sets of pores inverted with three sets of pores. Synthetic data are plotted as dots in the middle of the errorbars, red (p-wave), blue (S-wave). The errorbars, red (p-wave), blue (S-wave) represent the probability distribution, with the median data value (data without noise) in the middle of it. Noise realization is shown by the blue and red dots for the P-wave and S-wave spectra, respectively, for the model parameters see Table 3.5.	85
3.14	Illustration of the number of iterations needed by VFSA, the behaviour of the objective function, and cooling process (temperature curve) for the model in Figure 3.13 above.	86
3.15	The real data inversion for the model of two sets of pores. Synthetic data are plotted as dots in the middle of the errorbars, red (p-wave), blue (S-wave). The errorbars, red (p-wave), blue (S-wave) represent the probability distribution, with the median data value in the middle of it. for the model parameters see Table 3.6.	87
3.16	The number of iterations needed by VFSA, the behaviour of the cost function, and cooling process (temperature curve) for the model in Figure 3.15 above.	88

3.17	The real data inversion for the model of two sets of pores. Synthetic data are plotted as dots in the middle of the errorbars, red (p-wave), blue (S-wave). The errorbars, red (p-wave), blue (S-wave) represent the probability distribution, with the median data value in the middle of it. For the initial model and the best-fitting parameters been obtained see Table 3.7.	89
3.18	Illustration of the number of iterations needed by VFSA, the behaviour of the objective function, and cooling process (temperature curve) for the model in Figure 3.17 above.	90
3.19	The inverted model of three sets of pores. Synthetic data are plotted as dots in the middle of the errorbars, red (p-wave), blue (S-wave). The errorbars, red (p-wave), blue (S-wave) represent the probability distribution, with the median data value in the middle of it. for the model parameters see Table 3.8.	91
3.20	The inverted model of three sets of pores. Synthetic data are plotted as dots in the middle of the errorbars, red (p-wave), blue (S-wave). The errorbars, red (p-wave), blue (S-wave) represent the probability distribution, with the median data value in the middle of it, for the model parameters see Table 3.9.	92
3.21	Illustration of the number of iterations needed by VFSA, the behaviour of the objective function, and cooling process (temperature curve) for the model in Figure 3.20 above.	93
3.22	Inversion for only attenuation of the Portland limestone (top), using four different sets of pores. Synthetic data are plotted as dots in the middle of the errorbars, red (p-wave), blue (S-wave). The errorbars, red (observed p-wave), blue (observed S-wave), represent the probability distribution, with the median data value in the middle of it, for the model parameters see Table 3.10.	94
3.23	Illustration of the number of iterations needed by VFSA, the behaviour of the objective function, and cooling process (temperature curve) for the model in Figure 3.22 above.	95

3.24	The L1-norm inverted model for the Portland limestone (top). using four different sets of pores. Synthetic data are plotted as dots in the middle of the errorbars, red (p-wave), blue (S-wave). The errorbars, red (observed p-wave), blue (observed S-wave), represent the probability distribution, with the middle data value in the middle of it, for the model parameters see Table 3.10.	96
3.25	Illustration of the number of iterations needed by VFSA, the behaviour of the objective function, and cooling process (temperature curve) for the model in Figure 3.24 above.	97
3.26	The L2-norm inverted model for the Portland limestone (top). using four different sets of pores. Synthetic data are plotted as dots in the middle of the errorbars, red (p-wave), blue (S-wave). The errorbars, red (observed p-wave), blue (observed S-wave), represent the probability distribution, with the middle data value in the middle of it, for the model parameters see Table 3.10.	98
3.27	Illustration of the number of iterations needed by VFSA, the behaviour of the objective function, and cooling process (temperature curve) for the model in Figure 3.23 above.	99

List of Tables

- 1.1 Measured visco-elastic attributes of the Portland limestone (top) at sonic and ultrasonic frequencies. 7

- 3.1 Model parameters of the true model, initial model, and the inverted model based on the inversion of the model with tow different pore-types. 65
- 3.2 Model parameters for both the true model, the initial model, and the inverted model of two pore-types with noise levels, consistent with the uncertainties of the real data measurement. 65
- 3.3 Model parameters for, the true model, the initial model, and the inverted model, for data of three pore-types, inverted with model of two sets of pores. 67
- 3.4 Model parameters for, true model, initial model, and inverted model for the model with three pore types. 68
- 3.5 Model parameters of true model, initial model, and inverted model for the model with three pore types after adding some noises, consistent with uncertainties of the real data measurements. 68
- 3.6 Model parameters of the initial model and the inverted model, based on the inverted model of the real data. The model is of two pore-types. 69
- 3.7 Model parameters of the initial model and the inverted modelbased on the inverted model of the real data. The model is of three pore-types. 69
- 3.8 Best-fitting model parameters for the inverted model in comparison with initial model for the model with three different pore types. 71

3.9	Best-fitting model parameters for the inverted model in comparison with the initial model for the model with three different pore types.	72
3.10	Model parameters for the initial model, and inverted model for the model with four different pore types.	72

Chapter 1

Introduction

1.1 Carbonates and Related Porous Media

Carbonate rocks form an approximately 50% of the World hydrocarbon-bearing reservoirs (Li et al., 2018). Typical carbonates properties exhibit highly varying stiffness, complexity, and heterogeneity in their primary storage space (Agersborg et al., 2009; Eberli et al., 2003). The complexity and heterogeneity of carbonates follow naturally from the rapid and pervasive diagenetic alterations, complex forming, and depositional environment (Adam et al., 2009; Eberli et al., 2003). The combined effect of depositional lithology, in carbonates, and several post-depositional processes leads to a special velocity distribution, hence, controls the velocity (Eberli et al., 2003). Seismic attenuation give complementary information about the rock, e.g. sedimentary rocks, more specifically about their microstructural properties (Assefa et al., 1999).

Carbonates differ from siliciclastics by often having similar constituents, hence, yet need to be well studied (Agersborg et al., 2009). The effect of pore structure and texture, in carbonates found to be nearly identical with the porosity effect when it comes to acoustic velocity control (Eberli et al., 2003). According to the experimental data of (McCann and Sothcott, 2009), attenuation of acoustic waves, namely P- and S-waves in carbonates (limestones) can vary significantly with frequency, which is a result of the presence of discontinuities or disruptions in the matrix, either in the form of cracks or different scales of porosity (McCann and Sothcott, 2009) or generally due to the dependency on the details of the microstructures (Jakobsen et al., 2021). Thus, the complexity of carbonates leads to extra effort to be correctly recovered, when dealing with the acoustic signature;

for example, the complex properties in carbonates make the seismic responses and reservoir characterization more challenging than in siliciclastic rocks (Agersborg et al., 2009; Jakobsen et al., 2019; Li et al., 2018; Saberi, 2010).

Unlike siliciclastics in pure carbonates, the effective stiffnesses are affected by the concentration of the compliance and primarily controlled by porosities, mineralogy, pore types and the rock's fluid content (Agersborg et al., 2009). The squirt flow, the flow at the pore-scale, between communicating cavities of different shapes and orientation is considered to be the main mechanism of wave-induced fluid flow in the carbonates and related porous media, studied in this thesis. When dealing with the squirt flow dominant systems, the inclusion-based approach is more attractive, since it give adequate results (Jakobsen and Chapman, 2009). Therefore, in this thesis, inclusion-based approach using the rock physics t-matrix, consistent with the principle of fluid mass conservation (Jakobsen et al., 2003b), is been implemented.

Agersborg et al. (2009) studied the velocity variation of carbonates considering the dual porosity and wave-induced fluid flow. They presented efficient manually adjusted viscoelastic models for carbonates, using different pore scales. The work done by Jakobsen et al. (2021) gives an excellent understanding to estimate the microstructural parameters for complex media. They have discussed and presented a new experimental results, mainly the acoustic signature of the carbonate microstructure, pore-types, and rock constitutes, using three limestone samples. Jakobsen et al. (2021) concenter the local, squirt, flow to be the main mechanism for wave-induced fluid flow. Pore types of carbonate rocks can be roughly classified into intercrystalline, interparticle, intraparticle, moldic, vug, and fractures (Agersborg et al., 2009; Eberli et al., 2003).

1.2 Sonic and Ultrasonic Measurements on Carbonates

1.2.1 Sample Description

The descriptions of the sample, used in this thesis, are compiled from McCann and Sothcott (2009), and Jakobsen et al. (2021). The sample called Portland limestone (top). The Portland Limestone is of upper Jurassic age. Figure 1.1 (a) and (b) illustrates an scanning electron micro-photograph (SEM) of the Portland limestone sample, at two different scales, 100 μm and 10 μm , respectively. SEM micro-photograph is used to determine the mineralogy, porosity, permeability and the distribution of the pore types of the mineral (Assefa et al., 1999). SEM give both low-and high-resolution images. The sample is composed of pure calcium carbonate, which has porosity, ϕ_0 , of 21.2 %, permeability of 586

mD, grain density of 2679 kg/m^3 , dry density of 2111 kg/m^3 , and saturated density of 2297 kg/m^3 . The sample is an Oolitic porous grain-stone with large inter-granular pores and blocky calcite cement between the ooids. The ooids are rounded to sub-rounded, 250-750 μm in diameter. The ooids are formed of microspar crystals, 1-10 μm in diameter, and they have large internal microporosity.

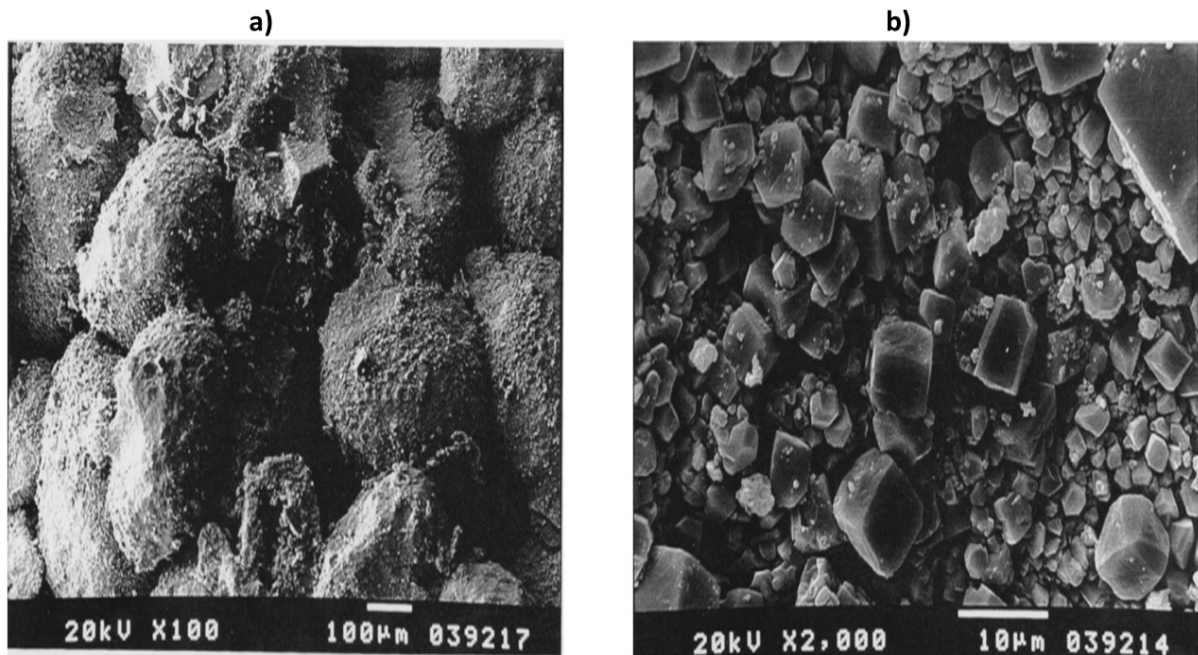


Figure 1.1: SEM of the Portland limestone sample, the sample is an Oolitic porous grain-stone with large inter-granular pores and blocky calcite cement between the ooids. The ooids are rounded to sub-rounded, 250 – 750 μm in diameter. **a)** Lower power of the sample, at the scale of 100 μm , showing the matrix made of ooids, large inter-granular pores and the local cement and **b)** Close up of the sample, at the scale of 10 μm , showing the ooids made of microspar with abundant porosity (Jakobsen et al., 2021).

1.2.2 Velocity and Attenuation Measurements

The measurements of the velocities and attenuations of P- and S- waves of the Portland limestone (top) was performed by McCann and Sothcott (1992, 2009), however, a review of the measurement system, the different methods has been performed, and a description of the different equipment is given in this section, since it is very important to understand the measurement system to perform a meaningful numerical experiments later, on this work, in Chapters 2 and 3. The sample used by McCann and Sothcott (1992, 2009), to measure the P- and S-wave properties, is 5 cm in diameter, the P- and S-wave attribute were determined at differential pressures up to 65 MPa. Torsional, or shear, and extensional modes of oscillation of each sample were measured over a frequency range of approximately

3 kHz to 30 kHz.

The Resonant-bar Method

The torsional, identical to a shear wave propagating in an infinite medium, and extensional modes of oscillation Portland limestone have been measured at sonic frequencies, using a resonant bar apparatus, see Figure 1.2 (McCann and Sothcott, 2009). In their measurement, they first, constructed and calibrated the equipments. The sample was jacketed in a thin (0.13 mm) copper sheet (O'Hara, 1985), since it allows making the measurements at reservoir temperatures and has negligible intrinsic absorption, opposed to other methods like heat-shrink sleeving or epoxy coating (McCann and Sothcott, 2009). Then, they used a resonant bar to measure right cylinders of rock, about 30 cm long by 2.54 cm diameter. The arrangement of the apparatus, used in the measurements, is identical to the one used by O'Hara (1985). However, McCann and Sothcott (2009) used a shorter sample than the one used by O'Hara (1985) which was 38 cm. The reason behind that is that the shorter sample increases the possibility of obtaining material from reservoir cores (McCann and Sothcott, 2009). A pore-fluid pipe was soldered into the copper, and the fluid-saturated cylinder was mounted inside a pressure vessel with helium gas, which operates as pressuring medium, providing a maximum confining pressure of 70 MPa.

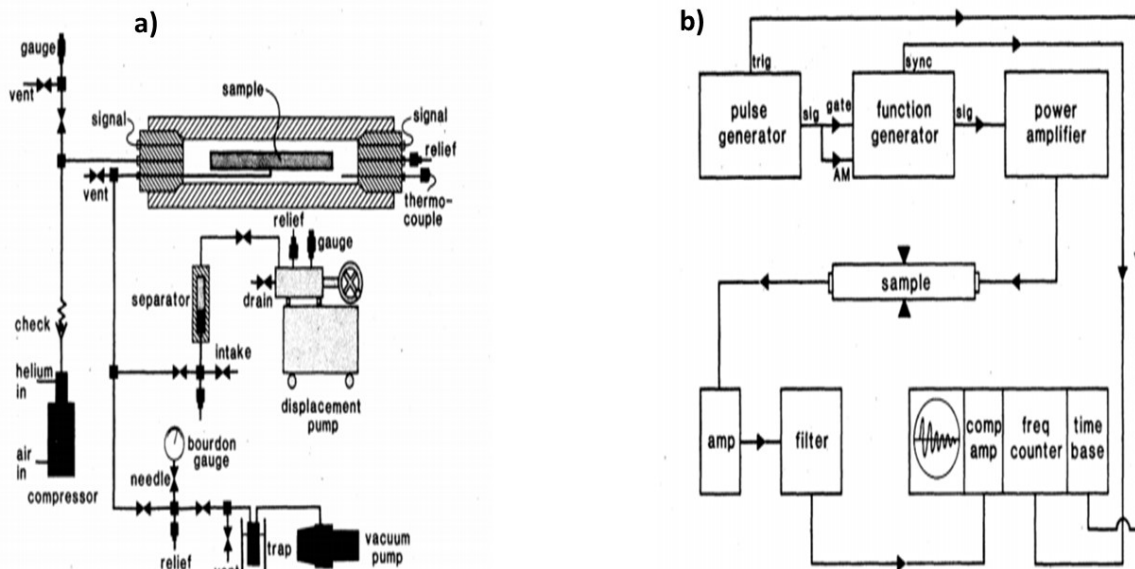


Figure 1.2: The resonant bar apparatus: a) Pressure apparatus used to subject the samples to elevated temperatures and hydrostatic confining pressure and to regulate the sample pore fluid pressure. b) Block diagram of electronic apparatus used for resonant rod measurements.(need reference)

Pulse-echo Method

McCann and Sothcott (1992, 2009) used the pulse-echo method, demonstrated in Figure 1.3, which uses an ultrasonic apparatus for the measurement at the ultrasonic frequencies (McCann and Sothcott, 1992).

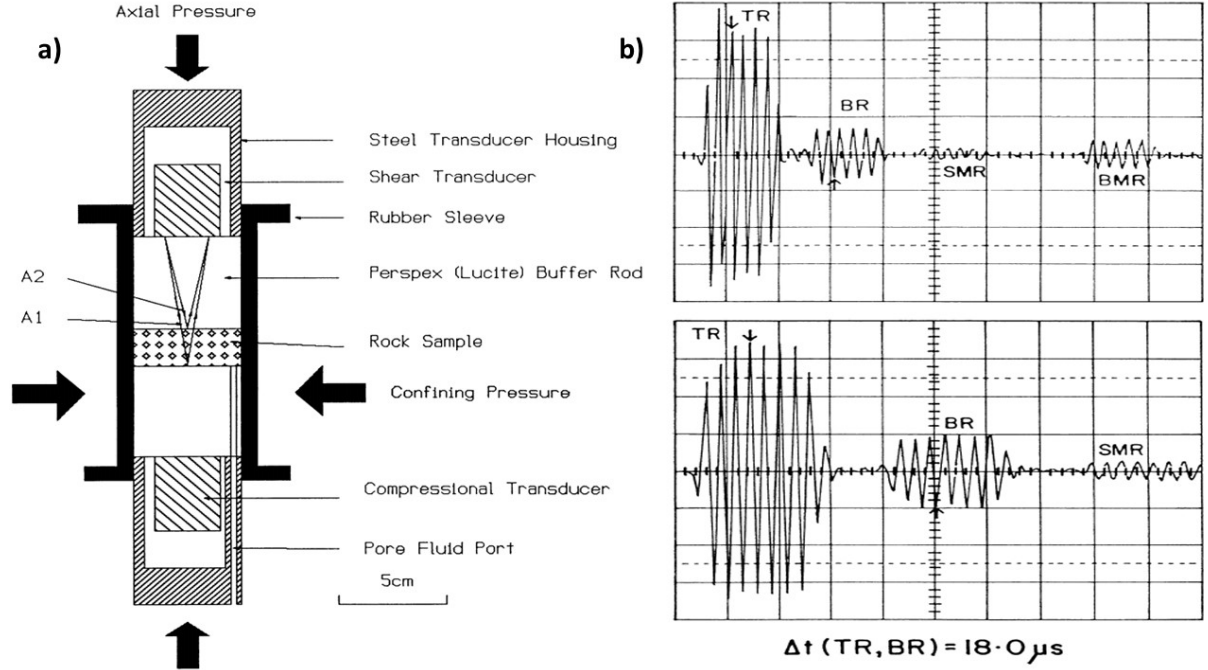


Figure 1.3: The pulse-echo method: a) Schematic diagram of the pulse-echo (reflection) method for measuring attenuation. b) Examples of P and S-wave pulse traces, where TR denotes sample-top reflection, BR denotes sample-bottom reflection, SMR denotes sample multiple reflection, and BMR denotes buffer multiple reflection (Assefa et al., 1999).

The shear and extensional velocities of the rock sample, $V_{s,E}$, where E denotes an extensional-mode resonance, were determined from the frequencies of resonance, $f_{s,E,n}$, of order n :

$$V_{s,E} = 2f_{s,E,n} \frac{L}{n}, \quad (1.1)$$

where L is isotropic rod length of the sample, and n is an odd integer.

The shear and extensional attenuations of the sample, $1000/Q_{s,E}$, were determined from the logarithmic decrements of successive free vibrations of the sample in the absence of the driving signal. The torsional mode velocity and attenuation require only correction for the effects of the copper jacket, Eqs. 1.5 and 1.6. The extensional mode velocity and attenuation were corrected for the radial component in the rod at the higher order harmonics, for the acoustic radiation from the side and the ends of the rod, and for the

effects of the copper jacket. Poisson's ratio, ν , of the sample were calculated from

$$\nu = -\frac{2V_{S2} + V_E}{V_{S2} * 2}. \quad (1.2)$$

The compressional wave velocity, V_P and attenuation, $1000/Q_p$, were calculated using the average of these ratios, from the resonant-bar data as follows:

$$V_p = V_s \sqrt{\frac{(2 - 2\nu)}{(1 - 2\nu)}}, \quad (1.3)$$

and

$$\frac{1000}{Q_p} = \frac{(1 + \nu)1000/Q_E - (2\nu)^2 1000/Q_s - 1}{(1 - \nu)(1 - 2\nu)}, \quad (1.4)$$

where $1000/Q_E$ and $1000/Q_s$ are the extensional and torsional attenuation, respectively. The measured velocities, and attenuations, were corrected for the effects of the copper jacket on the sample, the copper jacket corrected torsional or extensional velocity and attenuation (V_r and $1000/Q_r$) are given by ((McCann and Sothcott, 2009))

$$V_r^2 = \frac{V_m^2 \times (m_r + m_j)}{m_r} - \frac{C_j \times v_j}{m_r}, \quad (1.5)$$

and

$$1000/Q_r = \frac{1000/Q_m \times V_m^2 \times m_r + m_j}{V_r^2 \times m_r}, \quad (1.6)$$

respectively, where V_m is the measured torsional or extensional velocity of the sample, $1000/Q_m$ is the measured torsional or extensional attenuation of the sample, m_r is the mass of the rock and m_j is the mass of the copper jacket, C_j is the torsional elastic modulus (49.8 GPa) or the extensional elastic modulus (129 GPa) of the copper jacket, and v_j is the volume of the copper jacket. The results of these measurements are shown in Figure 1.4, and organised in Table 1.1.

Noise Investigation and Uncertainty

The real data measurements contaminates often with some noises, which causes uncertainties to the data been measured. Geophysical data, as well, may be affected significantly by the uncertainty due to the relationships between reservoir parameters and geophysical attributes being non-linear and non-unique (?). Thus, in inversion of synthetic data presented in this work, the estimation of the uncertainty is take to be consistent with the uncertainties estimation of the real data measurements, presented here in this section. For the uncertainty estimation, this work is Following McCann and Sothcott (2009) and the

uncertainty presented in an old version of (Jakobsen et al., 2021). First, they found the S-wave velocities and attenuations of the limestones to be reliable with uncertainties of ± 0.003 and ± 1 , respectively, for the data measured at the ultrasonic frequency. McCann and Sothcott (2009) showed in their work that, at the sonic frequency, the S-wave velocities and attenuations of the limestones, are also reliable with uncertainties of ± 0.003 and ± 1 , respectively, while the P-wave velocities and attenuations are reliable with uncertainties of ± 0.003 and ± 1 , respectively. Furthermore, their estimate of the uncertainties of the sonic frequency P-wave velocities and attenuations are ± 0.01 and ± 3 , respectively.

Table 1.1: Measured visco-elastic attributes of the Portland limestone (top) at sonic and ultrasonic frequencies.

Measured properties	Sonic frequency [Hz]					Ultrasonic frequency [Hz]
	3328	9914	16647	23290	30003	850000
$V_p[m/s]$	4292	4200	4231	4227	4237	4269
$V_s[m/s]$	2203	2188	2204	2202	2207	2202
$1000/Q_p$	1	4	8	14	16	42
$1000/Q_s$	5	6	6	7	7	50

1.3 Microstructural Visco-elastic Models

The clayey sandstones model quite similar to that of ?, can safely be treated as visco-elastic composites based on a model representing the clay phase in the form of isolated inclusions, within a load-bearing matrix of quartz (Jakobsen and Hudson, 2003; Jakobsen et al., 2003b). Agersborg et al. (2009) in their modelling of dual porosity, considered both the effective and elastic properties of aragonite, calcite and dolomite, making up the primary two scales of the porosity in the model they have used, namely, the micro and the meso scale. In this work, a microstructural visco-elastic models are presented. The discussed microstructures are, primarily: The aspect ratios, i , porosities ϕ_i , the squirt flow time, τ_i , for the inversion of real data X_p and X_s has been employed, which represent the perturbations in the P and S-wave velocities of the solid matrix, respectively. X_p and X_s are taken relative to calcite, which is the dominant mineral for these limestones (Jakobsen et al., 2021). Following Jakobsen et al. (2003b), and Agersborg et al. (2009), τ_i for water is taken as 0^{-7} . For the pore system, first, a relatively simple models, with

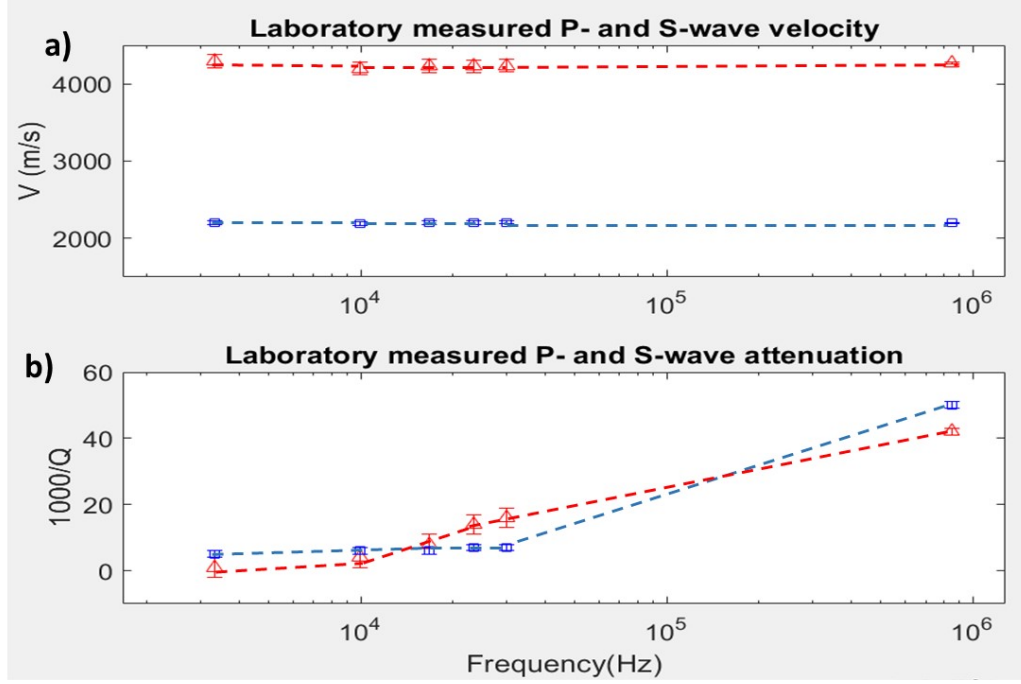


Figure 1.4: Measured data of the Portland limestone (top) sample at sonic and ultrasonic frequencies as in table 1.1: (a) P-wave velocity (red triangle) and S-wave velocity (blue squares), (b) P-wave attenuation (red triangle) and S-wave attenuation (blue squares). The errorbars, red (p-wave), blue (S-wave) represent the probability distribution, with the middle data value in the middle of it.

only consist of two or three pore-types are employed. The models with different sets of communicating cavities, has the following assumption: The pores in the model system of two pore-types are connected to each other with $\alpha_1 = 0.15$ and $\alpha_2 = 0.05$, see Figure 1.5 (a). The complexity of the model in (a) has been increased, by adding a flatter compliant ($\alpha_3 = 0.001$) to the model in (a), see Figure 1.5 (b), again, the pores are connected to each other, in (c) a new sets of compliant pore is added (pore type 4), pore [U+0638] type 4 are connected to each other (with dashed lines), however, isolated with respect to pore [U+0638] types 1-3. While pore-types 1-3 are connected to each other, but isolated with respect to pore type 4. For the modelling a visco-elastic generalized Xu-White clayey sand model (Xu and White, 1995) is used to understand the acoustic spectra of carbonate being studied.

Wave-induced fluid flow, discussed in Chapter 2, can occur at the scale of the acoustic wave-length, global flow, which is presented by Darcy's flow (Biot, 1956a,b), or at the scale of the microstructure, known as local flow or squirt flow (Gurevich et al., 2010; Jakobsen et al., 2003b). Biot (1956a,b) considered the phenomenon of the global flow and its effects on the overall wave characteristic, which is an important phenomenon, however it fails to interpret the high amount of attenuation, which associated with experimental

real data of the rock, which are assumed to be homogeneous on the macroscopic scale and fully saturated with fluid (Jakobsen et al., 2003b). Wave-induced fluid flow, known as the visco-elastic effects, is an important mechanism for acoustic attenuation and dispersion, discussed in Chapter 2 Section 2.2. Figure 1.6 illustrates the mechanism of squirt flow, in which the fluid flow, from the compliant soft pores to the more rounded stiffer pores. To demonstrate this phenomenon, a velocity-model of cracked porous medium, with two pores, is assumed (Figure 1.6 (a)). However, for the sake of calculations simplicity, a velocity constant medium is been assumed, while a two layer model is assumed to demonstrate the velocity variations. Figure 1.6 (b) demonstrates a synthetic seismic wave propagation, generated by solving the acoustic wave equation, Using Finite Differences method(FD). Then, by zooming in at a time t , while the time harmonic seismic wave, propagated from a shot point, is passing on the RVE (Figure 1.6 (c) at any point in the model, in this example represented by point $p(x,y)$, a fluid-pressure relaxation will take place, causing special fluid-pressure distribution. One may note that this work do not exclusively discuss the steps of FD implementation. And that is because this method has only been employed to generate synthetic wave propagation, concerning the demonstration of the squirt flow mechanism, however, the such method is defined to be out of the scope of this thesis.

1.4 Rock Physics Modelling and Inversion

Most attempts to match real rock acoustic data using theoretical models are based on forward modelling, sensitivity analysis and manual inversion. However, a unique feature of this master project is that a formal nonlinear rock physics inversion is been performed based on the minimization of a data mismatch function using simulated annealing (SA), proposed by Kirkpatrick et al. (1983). Reservoir engineers, on their first concern, would not be very interested for example in the acoustic impedance or the analysis of the waveform, the idea to improve and efficiently apply methods that explicitly give the microstructural parameters of the rocks, such as porosity, saturation, fluid pressure and permeability, will save time for engineers and help with ultimate production process. Furthermore, one of the advantages of SA is, that it provide good estimation of the misfit, and has the a criteria of finite probability of jumping out of local minima, and, simultaneously, settle into the global minimum, an illustration of SA optimization is shown in Figure 1.7, (Sen and Stoffa, 2013). SA has been often preferred, when it comes to the uncertainty characterization, comparing to other methods, such as genetic algorithms, GA. In this thesis, an instantaneous variant of SA, called VFSA, has been employed. VFSA makes such tasks this applicable and help on finding the best-fitting microstrutural parameter with a relatively short time. Both SA and VFSA, do not require a good choice of the starting model (Jakobsen et al., 2021; Sen and Stoffa, 2013). Experimentalist's experience is extremely needed, when it comes to VFSA coefficients selection, as this selection

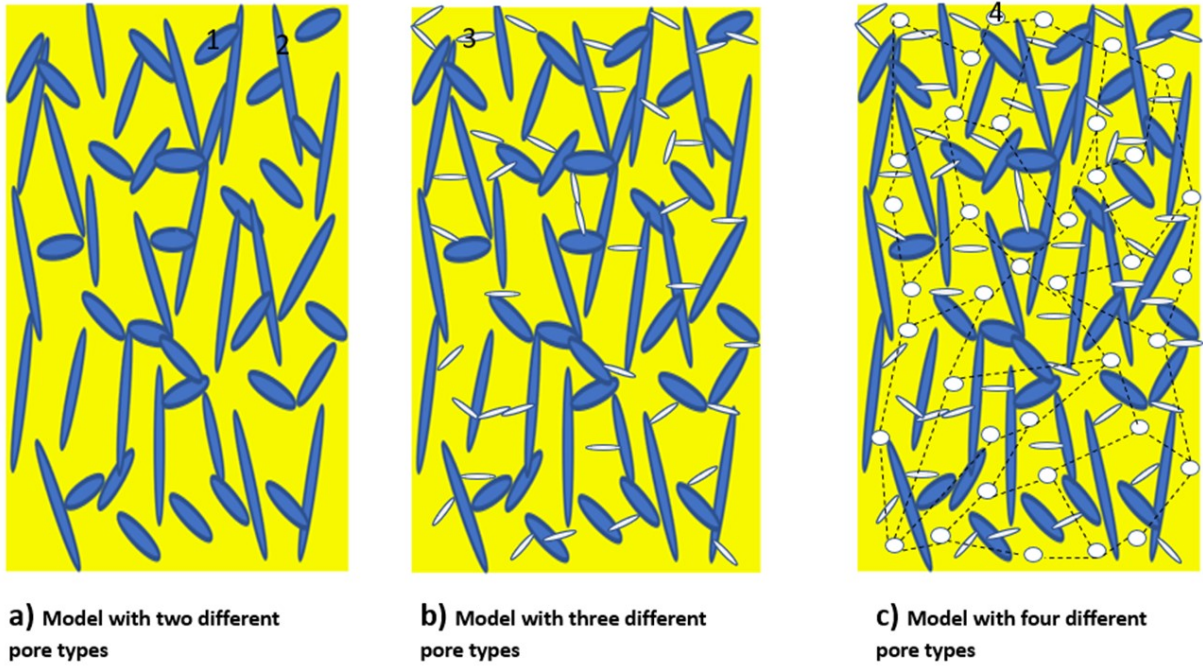


Figure 1.5: Sketched illustration of the models with different sets of communicating cavities: a) the pores are connected to each other ($\alpha_1 = 0.15$ and $\alpha_2 = 0.05$), b) the complexity of this model has been increased, by adding a flatter compliant ($\alpha_3 = 0.001$) to the model in (a), again, the pores are connected to each other, c) a new sets of compliant pore is added (pore type 4), pore type 4 are connected to each other (with dashed lines), however, isolated with respect to pore types 1-3. While pore types 1-3 are connected to each other, but isolated with respect to pore type 4.

is essential to obtain the optimal result using SA (Izumotani and Onozuka, 2013).

The reservoir system is dynamic, due to the production processes, and possibly before production process taking place, due to cementation and dissolution processes, as in carbonates (Eberli et al., 2003). Implementing this unique combination may give an adequate results to be used in connecting reservoir characterization and monitoring to the seismic modelling system.

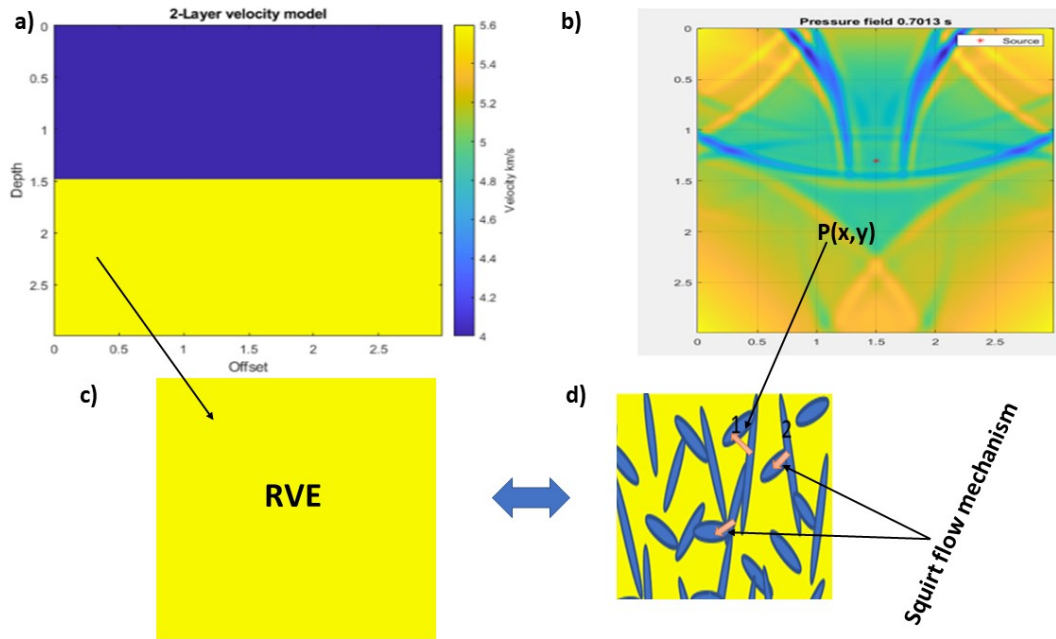


Figure 1.6: Wave induced fluid flow (squirt flow) caused by a seismic wave propagation, using a model of two layers: a) two layer velocity model b) acoustic wave propagation from a shot point (red star), for the sake of simplicity constant density was assumed c) a representative volume element, used as the effective homogeneous medium d) the real heterogeneous medium (micro scale) of the model at time t , demonstrating the squirt flow mechanism, in which the fluid flow from the compliant soft pores (pore type 2) to the more rounded stiffer pores (pore type 1).

Global optimization by SA

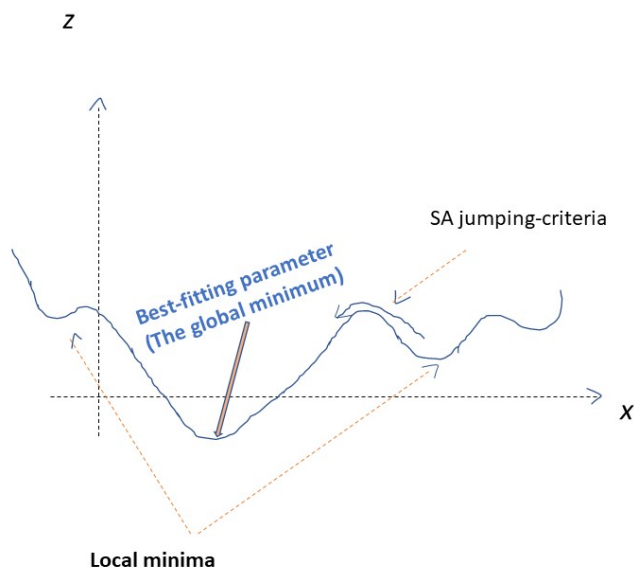


Figure 1.7: Simulate annealing minimization and its criteria of finite probability of jumping out of local minima, and, simultaneously, settle into the global minimum.

1.5 Applications to Seismic Reservoir Characterization

Seismic reservoir characterization and monitoring continuously improve by taking advantages of the powerful results of Rock Physics Inversion (RPI). A better understanding of the reservoir characterization can be obtained by studying both velocities and attenuation (Adam et al., 2009). Rock physics has generally developed a good understanding of the mechanism of the acoustic attenuation (Jakobsen et al., 2021). Rock physics consider a vital linkage between seismic data, which gives us the acoustic properties of rocks, and reservoir engineering that needs real parameters such as permeability, fluid type, and saturation, which is the main focus of rock physics. The acoustic properties is been studied by geoscientists using a combination of experimental and theoretical methods (Jakobsen et al., 2019). Seismic velocities varies with respect to rock densities, pore structure, fluid content, and confining pressure, affecting cracks (Eberli et al., 2003). Geoscientists have done relatively more work on understanding the acoustic properties of sandstones, in addition to the complexity of the porosity of rocks with cracks and fractures. There is an essential need for a better understanding of the acoustic properties of rocks featured with more complex media, such as carbonates, as it has been referred to by Siqueira et al. (2017). In addition to the relatively few studies that have been made to carbonate rocks, it is found to be characterized by dual-porosity and more complicated micro-structures and parameters than sandstones (Agersborg et al., 2009).

1.6 Main goals, Scope of the work, and Outline

1.6.1 Main Goals and Motivation

The main objectives of this thesis are to:

- Develop a microstructural visco-elastic model that can explain the measured velocity and attenuations of P- and S-waves at sonic and ultrasonic frequencies.
- Give a thorough review of the work by Jakobsen et al. (2021), on account of they managed to obtain a good match between theory and experiment, by using a relatively complicated model with four different pore types, an important task was to investigate the possibility to obtain a satisfactory match between theory and experiment by using a simpler model with only two and three different pore-types.
- Show that forward modelling results corresponding to different perturbations in the microstructural parameters can lead to an optimum understanding of the behaviour

of the microstructural models, and effectively employ that to obtain the ultimate match with the real data, presented in this thesis.

Furthermore, it is aimed to investigate the performance of the VFSA inversion algorithm of synthetic velocity and attenuation data. In this way, one can learn more about the relative importance of model errors and the effects of noise. Study how uncertainties in defining reservoir parameters can influence the inverse solutions.

Ultimately, having in mind the relevancy of visco-elastic modelling of the complex porous media, it is intended to suit the rock physics modelling and inversion for optimum production and reservoir characterization monitoring applications.

1.6.2 Scope of the Work and Limitations

In order for this work to be generalized and for the microstructural visco-elastic model to be considered as reliable model for carbonate rocks, one may need to compare with results of other porous media, e.g. sandstones. However, the lack of corresponding real experimental data limited the numerical experiments to carbonate rocks only.

Local effect of fluid flow, squirt flow, due to the propagation of body waves, in visco-elastic porous media, is studied in this thesis. Although the squirt fluid flow is found to be dominant in the complex media, the global flow can not simply be ignored. Therefore, the numerical results can not be used as a generalization for all cases of fluid flow.

1.6.3 Thesis Outline

A review of the data measured by Professor Clive McCann and lab technician Jeremy Sothcott is presented in this chapter, Chapter 1, these measured velocity and attenuation at sonic and ultrasonic are been used in this thesis. Furthermore, this chapter provide the reader with a precedent research on the topics of model for carbonates and visco-elastic porous media.

In Chapter 2, a sensitivity modelling for the microstructural visco-elastic models has been presented. This will be useful for the real data inversion, using VFSA, where the upper and lower bounds for an initial microstructural model parameter need to be defined. Furthermore, the effect of fluid substitution is been discussed.

Chapter 3 presents rock physic inversion of both real and theoretically predicted data, using VFSA.

Finally, in addition to the quite satisfactory discussion have been presented during the numerical results of Chapter 2 and 3 , an exclusive detailed discussions and the mean

finding of this work is presented in Chapter 4.

Appendix A provides an evaluation of the G-tensor while Appendix B presents discussion on the orientation averaging being used in this thesis.

Chapter 2

Rock Physics Modelling

2.1 T-matrix Approach to Effective Stiffnesses

The T-matrix approach in rock physics-based modelling and inversion, give a sufficient results, because of its flexibility and consistency in the rocks visco-elastic behaviour cite-jakobsen2003acoustic. Many physical significances and advantages of the T-matrix approach had been addressed lately by many scientist. For example, it can drive an exact solution for the stiffness tensor in Eq. 2.2 (Jakobsen et al., 2003a), which is a key in evaluating different porous media (e.g. anisotropic, elastic, and visco-elastic). The efficiency of the t-matrix lies on the fact that it can use a Lippmann-Schwinger type of integral, as well as it adds to the work the modern highly iterative methods of physics, something make it a very important approach in the inclusion models (Jakobsen et al., 2003a).

In visco-elastic media, stress is a convolution of the (time-domain) effective stiffness and strain tensors. Since convolution in the time-domain is equal to multiplication in the frequency-domain, the strain (response), $\bar{\epsilon}$, is still proportional to the applied stress, $\bar{\sigma}$. Hence, the relationship between stress and strain, is the same as Hook's law for the elastic media, given by (Guéguen and Palciauskas, 1994)

$$\bar{\sigma} = \mathbf{M}^* \bar{\epsilon}, \quad (2.1)$$

where \mathbf{M}^* is the effective elastic moduli, the only difference is that the effective elastic moduli, \mathbf{M}^* , of the visco-elastic media, known as the effective stiffness tensor, \mathbf{C}^* , becomes frequency-dependent and complex-valued (?)-jakobsen2003t). The non-local averaged stress tensor, $\bar{\sigma}$, of a statistically homogeneous visco-elastic material is given by

(Auld, 1990; Guéguen and Palciauskas, 1994; Jakobsen et al., 2003a)

$$\bar{\boldsymbol{\sigma}} = \mathbf{C}^* : \bar{\boldsymbol{\varepsilon}}, \quad (2.2)$$

where \mathbf{C}^* is the effective stiffness tensor of the visco-elastic media. The statistically homogeneous medium refers to a heterogeneous medium on the small scale (grain or micro-scale) but appears homogeneous as a whole, macro-scale. Then, the sufficiently large subregion of that material is statistically identical to the whole specimen (Guéguen and Palciauskas, 1994; Jakobsen et al., 2003a), which means that the physical response is described by the average properties of the representative volume element (RVE), which are the effective properties for this type of media (Guéguen and Palciauskas, 1994). The stiffness tensor \mathbf{C}^* in Eq. 2.2 above, for both the elastic and visco-elastic media, is given by (Jakobsen et al., 2003a,b), Eq. 2.3. In this case the medium have non-zero attenuation and dispersion, as a result the stiffness tensor becomes frequency-dependent and complex-valued (Agersborg et al., 2007; Jakobsen et al., 2003b). For the visco-elastic model, used in this thesis, a frequency-dependent effect of wave-induced fluid flow is considered. Thus, parameters related to the fluid and its ability to flow, such as fluid density and viscosity, need to be taken into consideration (Jakobsen and Hudson, 2003; Jakobsen et al., 2003b). The attenuation, expressed as $1000/Q$, is one of the key factors when dealing with visco-elastic models, which is the loss per wavelength or, in other words, the energy loss of the seismic wave, that is because the attenuation becomes significant with frequency in fluid-saturated rocks (Jakobsen et al., 2021). The propagation of visco-elastic waves in rock-like composites implies a dynamic situation, which must be consistent with the quasi-static considerations.

In this work, an isotropic model is assumed, by taking the orientation average, discussed in Appendix B, of the randomly oriented communicating cavities, and all inclusions are assumed to be cavities. Considering a model of a homogeneous matrix material embedded with inclusions of the same scale, Jakobsen et al. (2003a,b) developed an instrumental theory of the visco-elastic effective medium. They divided the model into families having the same concentrations, shapes and orientations. It is not necessary that the inclusion is a matrix, but it can also be cavities (e.g., pores, compliant pores, and cracks). , labelled $r = 1, 2, \dots, N$. Hence, \mathbf{C}^* is given by (Jakobsen et al., 2003a)

$$\mathbf{C}^* = \mathbf{C}^{(0)} + \sum_{r=1}^N \phi_r \bar{\boldsymbol{\mathbf{t}}}^{(r)} : \left(\mathbf{I} - \mathbf{G}_d : \sum_{s=1}^N \phi_s \bar{\boldsymbol{\mathbf{t}}}^{(s)} \right)^{-1}, \quad (2.3)$$

where \mathbf{I} is the identity for the fourth-rank tensors, assuming ϕ_r to be the volume concen-

tration for the inclusion of type r , $\bar{\mathbf{t}}^{(r)}$ represents the orientation averaged t-matrix for a single communicating cavity of type r . \mathbf{G}_d is a fourth-rank tensor, which is given by the modified green's function for strain integrated over a characteristic ellipsoid, which describes the random spatial distribution of cavities as given by [Jakobsen et al. \(2003a\)](#). The G-tensor evaluation of the isotropic matrix material containing spheroidal inclusions with semiaxes $a_1^{(r)}=a_2^{(r)}=a_r^{(r)}$ and $a_3^{(r)}=b_r$, is presented in Appendix ??.

In Eq. 2.3 above, $\mathbf{C}^{(0)}$ is the fourth-rank stiffness tensor of the homogeneous matrix material, using Kelvin notation, which adds a weight of 2, to the lower right corner ([Dellinger et al., 1998](#)). given by

$$\mathbf{C}^{(0)} = \begin{bmatrix} C_{11} & C_{12} & C_{12} & 0 & 0 & 0 \\ & C_{11} & C_{12} & 0 & 0 & 0 \\ & & C_{11} & 0 & 0 & 0 \\ & & & 2C_{44} & 0 & 0 \\ & & & & 2C_{44} & 0 \\ & & & & & 2C_{44} \end{bmatrix}, \quad (2.4)$$

where $c_{12} = c_{11} - 2c_{44}$.

respectively. The t-matrix for a single cavity of type r , which is isolated concerning wave-induced fluid flow, is given by ([Jakobsen et al., 2003a,b](#))

$$\bar{\mathbf{t}}^{(r)} = (\mathbf{C}^{(r)} - \mathbf{C}^{(0)}) : [\mathbf{I}_4 - \mathbf{G}^{(r)} : (\mathbf{C}^{(r)} - \mathbf{C}^{(0)})]^{-1} \quad (2.5)$$

where $\mathbf{C}^{(r)}$ is the stiffness tensor for the single cavity and $\mathbf{G}^{(r)}$ is a fourth-rank tensor that depends only on the aspect ratio of the single cavity and $\mathbf{C}^{(0)}$.

2.2 Visco-elastic Effects due to Squirt Flow

Pore pressure communication and wave induced fluid flow can play significant roles on the effective stiffness of complex porous media ([Agersborg et al., 2009](#)). The compliant, soft cracks with very small α_i in the models discussed in this study, edges open into the more round shaped stiff pore and they form a disk-shaped gap between the neighbouring grains ([Gurevich et al., 2010](#)). Following [Jakobsen et al. \(2021\)](#), the squirt flow is considered the primary mechanism for the wave-induced fluid flow. In complex media, the squirt flow often dominating the global flow ([Agersborg et al., 2009, 2008](#)). The effect of global flow

becomes negligible when the fluid viscosity, the porosity and/or permeability of the specific complex media is very small, which is the case for many carbonate rocks, (Agersborg et al., 2008; Klimentos and McCann, 1990). The wave-induced fluid flow, squirt flow, appears to have the major cause of attenuation of the seismic waves passing fluid saturated rocks (Gurevich et al., 2010). The saturated cavities, pores and cracks, are considered to be communicating with respect to fluid flow. This type of cavities, discussed and studied by Gurevich et al. (2010); Jakobsen (2004); Jakobsen and Chapman (2009); Jakobsen et al. (2003a,b) are assumed to be cavities that allow the exchange of fluid mass caused by the wave-induced fluid flow. The t-matrix of a fully saturated communicating cavity is given by Jakobsen et al. (2003b)

$$\bar{\mathbf{t}}^{(r)} = \bar{\mathbf{t}}_d^{(r)} + \frac{\Theta \bar{\mathbf{Z}}^{(r)} + i\omega\tau_r k_f \bar{\mathbf{X}}^{(r)}}{1 + i\omega\tau_r \gamma^{(r)}}, \quad (2.6)$$

where $\bar{\mathbf{t}}_d^{(r)}$ is the t-matrix of the dry cavities of type r, Θ and $\gamma^{(r)}$ are physically related with the average wave-induced pore fluid pressure and the frequency location of the maximum attenuation peak, respectively, both $\gamma^{(r)}$, and the fourth-rank tensors $\mathbf{X}^{(r)}$, and $\mathbf{Z}^{(r)}$ in Equation 2.6 are given by (Jakobsen et al., 2003b)

$$\gamma^{(r)} = 1 + k_f (K_d^{(r)} - S^{(0)})_{uvvv}, \quad (2.7)$$

$$\mathbf{X}^{(r)} = \bar{\mathbf{t}}_d^{(r)} : \mathbf{S}^{(0)} : (\mathbf{I}_2 \otimes \mathbf{I}_2) : \mathbf{S}^{(0)} : \bar{\mathbf{t}}_d^{(r)}, \quad (2.8)$$

and

$$\mathbf{Z}^{(r)} = \mathbf{t}_d^{(r)} : \mathbf{S}^{(0)} : (\mathbf{I}_2 \otimes \mathbf{I}_2) : \mathbf{S}^{(0)} : \left(\sum_s \frac{\phi_s \mathbf{t}_d^{(s)}}{1 + i\omega\gamma^{(s)}\tau_s} \right), \quad (2.9)$$

respectively, where $K_d^{(r)}$ denotes the k-matrix of type r, for the dry and can be found from the superposition of results from two different, gedanken, experiments (Jakobsen et al., 2003b), \mathbf{I}_2 in Equations 2.8 and 2.9 above is the identity for second-rank tensors, and the symbol \otimes denotes the dyadic tensor product, and Θ is given by (Jakobsen et al., 2021)

$$\Theta = k_f \left(\sum_s \frac{\phi_s \gamma^{(s)}}{1 + i\omega\gamma^{(s)}\tau_s} \right), \quad (2.10)$$

where k_f is the bulk modulus of the fluid, given by

$$C_f = \begin{bmatrix} \kappa_f & \kappa_f & \kappa_f & 0 & 0 & 0 \\ & \kappa_f & \kappa_f & 0 & 0 & 0 \\ & & \kappa_f & 0 & 0 & 0 \\ & & & 0 & 0 & 0 \\ & & & & 0 & 0 \\ & & & & & 0 \end{bmatrix}. \quad (2.11)$$

The P- and S-wave velocity and attenuation, for the assumed to be isotropic media, is given by (Jakobsen et al., 2003b)

$$V_P = \left[\Re \left(\frac{c_{11}^*}{\rho^*} \right)^{-\frac{1}{2}} \right]^{-1}, \quad (2.12)$$

$$V_S = \left[\Re \left(\frac{c_{44}^*}{2\rho^*} \right)^{-\frac{1}{2}} \right]^{-1}, \quad (2.13)$$

$$Q_P = \frac{\Re(c_{11}^*)}{\text{Im}(c_{11}^*)}, \quad (2.14)$$

and

$$Q_S = \frac{\Re(c_{44}^*)}{\text{Im}(c_{44}^*)}, \quad (2.15)$$

respectively, where \Re denotes the real part, and Im denotes the imaginary part.

Algorithm 1: Pseudo code used for the rock physics modelling, based on a theoretically predicted visco-elastic Xu-White model, at sonic and ultrasonic frequencies similar to real experiments, presented in Table 1.1. The orientation averaging (iso-average) should be taken into account, when computing the tensors involved. Equations from Sections 2.1 and 2.2 should be implemented for the computation of the parameters, which this code requires.

Compute frequency-independent quantities of the visco-elastic model.

for $i = 1, 2, \dots, N_f$ **do**

frequency-independent quantities.

Calculate the t-matrix, $\mathbf{t}_d^{(r)}$, of the dry cavities of type r by Eq. (2.6).

Determine the fourth-rank effective stiffness tensor, \mathbf{C}^* , from Eq. (2.3).

$$V_{Pc} = \sqrt{\frac{c_{11}^*}{\rho^*}}$$

$$V_{Sc} = \sqrt{\frac{c_{44}^*}{2\rho^*}}$$

$$S_{Pr} = \Re \left[\frac{1}{V_{Pc}} \right]$$

$$S_{Sr} = \Re \left[\frac{1}{V_{Sc}} \right]$$

$$V_{P \text{ obs}}^{(i)} = \frac{1}{S_{Pr}}$$

$$V_{S \text{ obs}}^{(i)} = \frac{1}{S_{Sr}}$$

$$Q_{P \text{ obs}}^{(i)} = 1000 \times \frac{\text{Im}[V_{Pc}^2]}{\Re[V_{Pc}^2]}$$

$$Q_{S \text{ obs}}^{(i)} = 1000 \times \frac{\text{Im}[V_{Sc}^2]}{\Re[V_{Sc}^2]}$$

end for

2.2.1 Fluid Substitution

Fluid substitution is one of the key factor in reservoir monitoring and time-laps seismic inversion. The Gassmann's equation can be used to estimate fluid substitution in the real rock if the Voigt & Reuss or Hashin-Shtrikman are employed to compute the effective stiffness, due to heterogeneous. When the fluids are not assumed to be equally distributed, one may need to apply the patchy saturation model, compiled with Gassmann's equation to consider fluid substitution. However, the those methods are considered to be outside of the scope of this thesis. Following (Agersborg et al., 2009) and using the key parameter τ , the visco-elastic t-matrix has been employed to perform the fluid substitution. The relaxation time constant τ is assumed to be an empirical constant and is suggested to be dependent on the scale of the pores and cracks, and the properties of the fluid (Jakobsen et al., 2003b). The constant τ_i for each fluid under the assumption of this work, the squirt

flow to be the main cause behind the evident attenuation, is give by

$$\tau_i = E_c \eta_i, \quad (2.16)$$

Where E_c denote an empirical constant. Assuming a fluid with τ_{f_1} , and η_{f_1} is been substituted with another fluid, τ_{f_2} , and η_{f_2} , the new τ parameter, τ_2 , is given, from Eq. 2.16, by (Agersborg et al., 2009)

$$\tau_{f_2} = \tau_{f_1} \frac{\eta_{f_2}}{\eta_{f_1}}. \quad (2.17)$$

Batzle and Wang (1992) give pore fluids properties at temperature of 80 °C and a pore pressure of 40 MPa, the oil properties under these condition is as follow: density, $\rho_{oil} = 854$ kg/m³ and viscosity, $\eta_{oil} = 6.4$ cP.

2.3 Numerical Results and Discussion

2.3.1 Models with Two Different Pore-Types

In this modelling part, a sensitivity study is presented, using synthetic data of velocity and attenuation data for P- and S-waves at sonic and ultrasonic frequencies. These experiments are made similar to real experiments of the inversion of real data in Chapter 3, using a visco-elastic t-matrix model. This study will be used effectively in the studying and for better understanding of such complex rock, being studied in this thesis. The sensitivity study is carried out for models of two stets of pores and three sets of pores, respectively, using the procedures described on Algorithm 1.

This sensitivity study will primary focus in the either increasing or decreasing of the velocity and attenuation spectra due to perturbing the model microstructural parameters. In other words, the changes on compressional and shear wave velocities, V_p , V_s , and attenuations, Q_p , and Q_s , spectra, respectively, as a result of changes in the microstructural parameters, mainly the pore shapes aspect ratios (α_i), their corresponding volume concentrations (ϕ_i), and squirt flow constants (τ_i). First, the well known Xu-White (Xu and White, 1995), with $\alpha_1 = 0.15$ and $\alpha_2 = 0.05$ is used. The model is assumed to be fully water saturated ($\tau_i = 10^{-7}$), see Figure 2.1. Then, some other models were produced by both negative and positive perturbation of the microstructural parameters. Xu-White model is consider to be the reference model, other models are compared to. The maximum and minimum perturbations of α_i and ϕ_i , in this study, are 50 percent. While for τ_i , the maximum perturbation is 10^{-6} and the minimum perturbation is 10^{-8} , By the maximum and minimum here, it is meant the highest increase, upper pound, and the lowest decrease, lower pound, respectively. The model parameters will be perturbed using this two pounds, which are consistent with the inversion part in 3 . In all cases,

the microstructural parameters are firstly perturbed. Secondly, more perturbation in the same direction is performed. Finally, the minimum or the maximum perturbation, of that specific direction, been taken. Several numerical experiments have been performed to study the sensitivity of the model to the change of all the microstructural parameters mentioned previously. The perturbation is often on every parameter at a time to examine the effect of that particular parameter. However, the perturbation of two parameters together is sometimes performed.

Effects of aspect ratios and porosities

First, a negative perturbation on the aspect ratio of the soft pores (α_2) is done, while the more rounded sands aspect ratio (α_1) kept as it is. Some changes on the paths of the curves is obtained, namely some decreases on V_p and V_s and increases on their corresponding attenuations, see Figure 2.2. At lower aspect ratio of the clay, α_2 , which is the minimum perturbation in this study, it gives further more decrease in V_p and V_s and increase in their corresponding Q_p and Q_s . The changes is in the same direction of the previous experiment. Keeping in mind that the increases in Q_p are significant comparing to the increases in Q_s , see Figure 2.3. Next, a positive perturbation of the aspect ratio α_2 , is carried out by increasing its value. this gives some increases in V_p and V_s with corresponding decrease in their attenuations, see Figure 2.4. However. Finally, the maximum perturbation of α_2 , is taken. The result is shown in Figure 2.5, it is true that it gives an opposite changes. However the changes this time is relatively not very significant.

Next, the change of the more rounded sands aspect ratio α_1 is examined while the aspect ratio α_2 is kept fixed. First, a negative perturbation of α_1 is done, A significant decreases on both V_p and V_s , specially more on V_p , have been obtained. The increases on Q_p , however, are not very significant, while Q_s shows a significant increases, see Figure 2.6. At the minimum perturbation of α_1 , a very significant changes in the same direction have been obtained, still the decreases are specially more noticeable on V_p compared to V_s , while the increases on Q_p are less compared to Q_s , which shows a significant increases see Figure 2.7. Next is a positive perturbation of α_1 , some changes on the opposite direction is been recorded, nevertheless a significant increases on both V_p and V_s , specially more on V_p . The decreases on Q_p , however, is not very significant, while Q_s shows a significant decreases compared to Q_p , see Figure 2.8. At the maximum perturbation of α_1 , a very significant changes is obtained. Still, the increases are especially more on V_p compared to V_s . Simultaneously, the increases in Q_p are less compared to Q_s , as shown in Figure 2.9.

When it comes to porosity (ϕ_i), it is only ϕ_2 that will be perturbed. The negative per-

turbation on ϕ_2 gives an increases on Vp and Vs with corresponding decreases on their attenuations, see Figure 2.10. Figure 2.11 illustrates the minimum perturbation on ϕ_2 . While a positive perturbation on (ϕ_2) gives some decreases on Vp and Vs, with corresponding increases on their attenuations, see Figure 2.12. Figure 2.13 illustrates the maximum perturbation on ϕ_2 .

Effects of squirt flow times τ_i

The squirt flow parameter, τ_i , seems to be a very uncertain and quit complicated parameter to understand. However, it has a big effect on the acoustic properties of the rock. Therefore, the perturbation of τ_i is done in a wider interval (minimum to maximum). Since the perturbation on τ_i cause the peaks shift, either toward high frequency or to the lower frequency, on the other hand, the velocity spectra, being studied in this thesis, shows no significant effect when changing on τ_i , there will be focus on the attenuations only. It is interesting to see, by only perturbing on τ_i values, a significant moves on the position of the peaks of the attenuation spectra. Furthermore some changes on their shapes. The maxima display, sometimes, either an increase or a decrease. The peaks of the attenuation spectra in all cases move either to the right (higher frequency) or to the left (lower frequency). Generally a negative perturbation on τ_i , no mater if it was a perturbation on τ_1 and τ_2 together, or on each one of them at a time, shifts the peaks to the higher frequency. On the other hand, a positive perturbation of τ_i makes the peaks shift to the lower frequency. A negative perturbation of both τ_1 and τ_2 gives a clear shift of the peaks of both Qp and Qs to the higher frequency and cause some slight increase on the peak of Qp, from 11.35 (at the reference Xu-White model) to 11.38 with slightly decreasing on the peak of Qs from 17.1232 (at the reference Xu-White model) to 17.085, see Figure 2.14. The next step is the minimum perturbation of τ_1 and τ_2 , which result in a more notable changes in the same direction, see Figure 2.15. Then, a positive perturbation of both τ_1 and τ_2 is taken. An apparent shift of the peaks to the opposite direction, has been obtained, and the Qp peak increased upto 11.40, while Qs peak decreased to 17.050, see Figure 2.16. For higher changes in the same direction, see the maximum perturbation, shown in Figure 2.17. In the coming experiments, change on each of τ_1 and τ_2 at a time is done. A negative perturbation of τ_1 makes the peaks shift to the higher frequency, and causes an apparent decrease on both Qp and Qs to 9.01 and 15.53, respectively, see Figure 2.18. It is noticeable that Qp is more affected by the decrease of τ_1 in terms of the reduction of the values and missing its peaks sharpness. In Figure 2.19 the changes become more evident at the minimum perturbation and Qp spectrum begins to have two peaks instead of one. Then, a positive perturbation of τ_1 makes the peaks shifts to the lower frequency, and cause a decrease in both Qp and Qs to 10.74 and 16.55, respectively,

as shown in Figure 2.20. For more noticeable change, see the maximum perturbation in Figure 2.21. However this time the changes are not as clear as changes towards the higher frequency. Finally, both negative and positive perturbations on τ_2 have been taken. The negative perturbation on τ_2 makes the peaks shift to the lower frequency, and cause some decrease on Qp and Qs, see Figure 2.22. In Figure 2.23, the changes become more clear at the minimum perturbation while the positive perturbation of τ_2 makes the peaks shift to the higher frequency, see Figure 2.24, the effects of the maximum perturbation on τ_2 are shown in Figure 2.25. Again, it is noticeable that Qp is more affected by the changes on τ_2 than the equivalent change on τ_1 in reducing the values and missing its peak sharpness; in addition to that, the Qp spectra begins to shape two peaks instead of one, which become more evident at the maximum perturbation of τ_2 . However, the effects of changes on τ_2 are in general much less than the effects of the equivalent changes on τ_1 .

2.3.2 Fluid Substitution of Model with Two Pore-Type

To substitute water with oil, in the models discussed in Sections 2.3.1. 2.17 above, and the properties given by Batzle and Wang (1992) has been employed, the effect of fluid substitution has been determined. Figure 2.31 shows the effect of fluid substitution in the model of two pore types. The model to compare with is the fluid saturated visco-elastic model in Figure 2.1. The affects of pore-fluid substitution, in which the water has been substituted with oil, are noticeable on the attenuation more than the velocity, the attenuation peaks moved to the lower frequency.

2.3.3 Models with Three Pore-Types

The complexity of the model in the previous experiments has been increased by adding more flatter cracks with aspect ration of $\alpha_3 = 0.001$ as shown in Figure 1.5. Since the other parameters are studied well on the previous subsection, this subsection's focus is more on the flat cracks effects, namely cracks with $\alpha_3 = 0.001$, and its corresponding porosity ϕ_3 . Using the result of the previous modelling of two pore types, and since the effects of ϕ_3 in this study appear to be not very big, the change on it has been done accordingly with the change of α_3 . The minimum and maximum perturbation on α_3 is again 50 percent. First, a negative perturbation on α_3 , accordingly on ϕ_3 , has been taken. The result is relativity small decrease in Vp and Vs and increase in their corresponding attenuations comparing with the reference Model 2.26, see Figure 2.27. At lower α_3 , which is the minimum perturbation in this study, a further decrease in Vp and Vs and increase in their corresponding Qp and Qs is obtained. The changes are in the same direction of the previous experiment. Again, one can notice that the increases in Qp are significant comparing to the increase in Qs, see Figure 2.28. Next is a positive perturbation of

α_3 , the results show slight increase in V_p and V_s with decrease in their corresponding attenuations, see Figure 2.29. Then, the maximum perturbation of α_2 is taken and the results are shown in Figure 2.30. however, the changes this time are not very significant.

2.3.4 Fluid Substitution of Model with Three Pore-Type

To substitute water with oil, in the models discussed in Section 2.3.3, again, Eq. 2.17 above and the properties given by Batzle and Wang (1992) has been employed, the effect of pore-fluid substitution has been investigated. Figure 2.32 shows the effect of fluid substitution in the model of three pore-types. The reference model in this case is show in Figure 2.26. Again, the affects of the substitution of water with oil in the model with three communicating sets of pores, are noticeable on the attenuation more than the velocity, the attenuation peaks moved toward the lower frequency.

2.4 Concluding Remarks

From the numerical experiment performed in Section 2.3, one can conclude that, in complex porous media such as carbonates and related porous media, even if porosity is constant, the variations in pore type can cause variable velocity (Agersborg et al., 2009; Eberli et al., 2003). The microstructural models with both two and three pore-types are employed as less complex and moderate complex visco-elastic generalized Xu-White models, respectively. These microstructural visco-elastic model, give usable indications to the behaviour that a complex medium can take, when constituting of several pore-type than the usual case for siliciclastics. The previous experiments in Section 2.3, show that the perturbation on τ_i makes the peaks shift, either toward high frequency or to the lower frequency, this is noticeable clearly on the attenuation. The fact that, the attenuation spectra is more sensitive to the perturbation on τ_i , is very interesting and encourages one to give more care to the attenuation. These are very useful indications, since the ultimate goal of this modelling is to build a good understanding of the visco-elastic behaviour of carbonates. From the numerical experiments were done in this work, it is clear that the attenuation varies with the change on the model parameters, this is discussed more deeply in the numerical results and discussion section in Chapter 2.

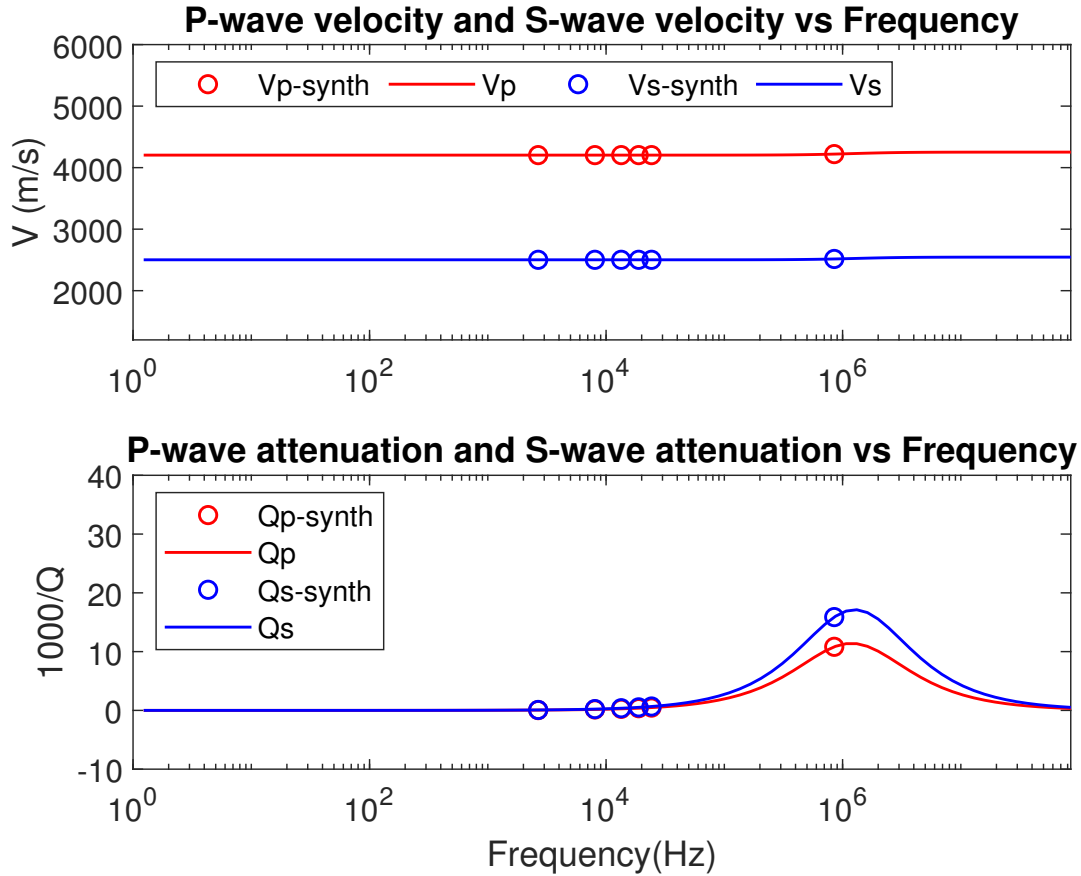


Figure 2.1: Theoretical predictions of the velocity and attenuation spectra of a rock model with two types of pores, versus synthetic data. This is the reference model (Xu-White model), and it is water saturated. The model parameters are: $[\alpha_1 = 0.15, \alpha_2 = 0.05, \phi_2 = 0.00556, \tau_1 = \tau_2 = 1 \times 10^{-7} \text{ s}]$.

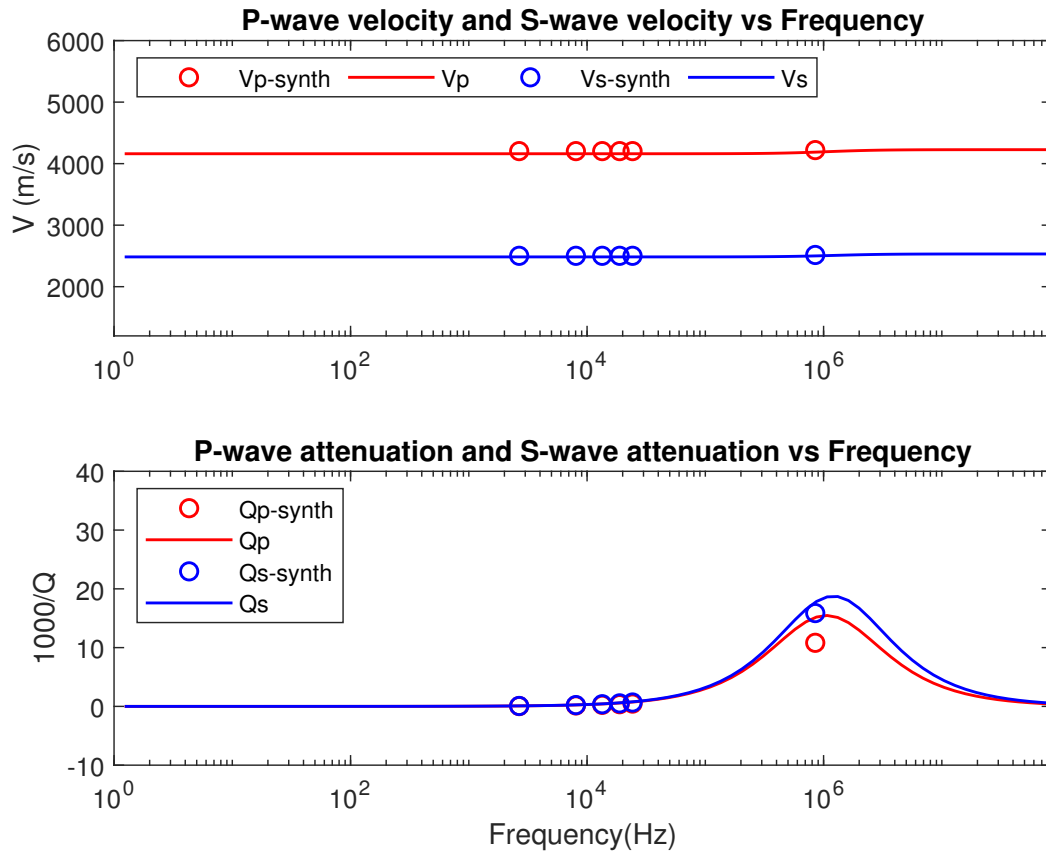


Figure 2.2: The effect of a negative perturbation of α_2 on the velocity and attenuation spectra of a rock model with two types of pores, using Xu and White model as a reference model, with model parameters of: $[\alpha_1 = 0.15, \alpha_2 = 0.0375, \phi_2 = 0.0056, \tau_1 = \tau_2 = 1 \times 10^{-7}$ s].

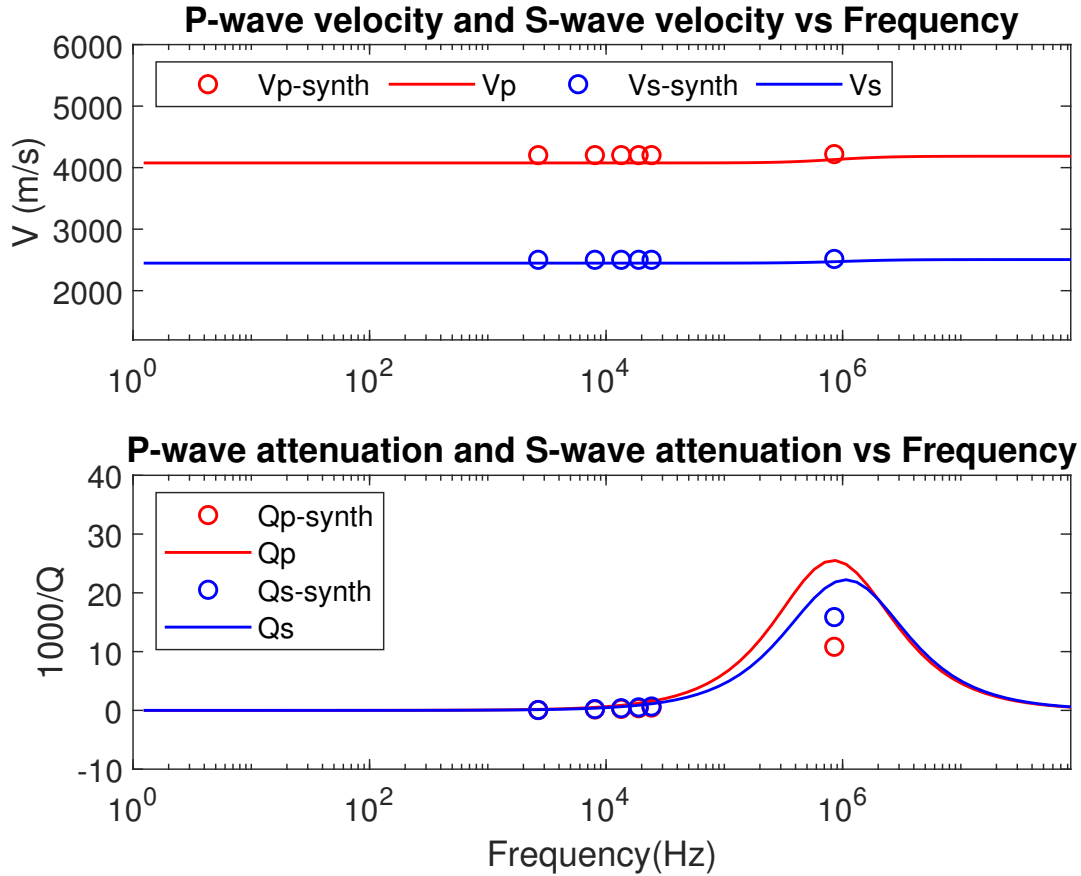


Figure 2.3: The minimum perturbation of α_2 , and how it affects the velocity and attenuation spectra of a rock model with two types of pores, using Xu and White model as a reference model, with model parameters of $[\alpha_1 = 0.15, \alpha_2 = 0.025, \phi_2 = 0.00556, \tau_1 = \tau_2 = 1 \times 10^{-7} \text{ s}]$.

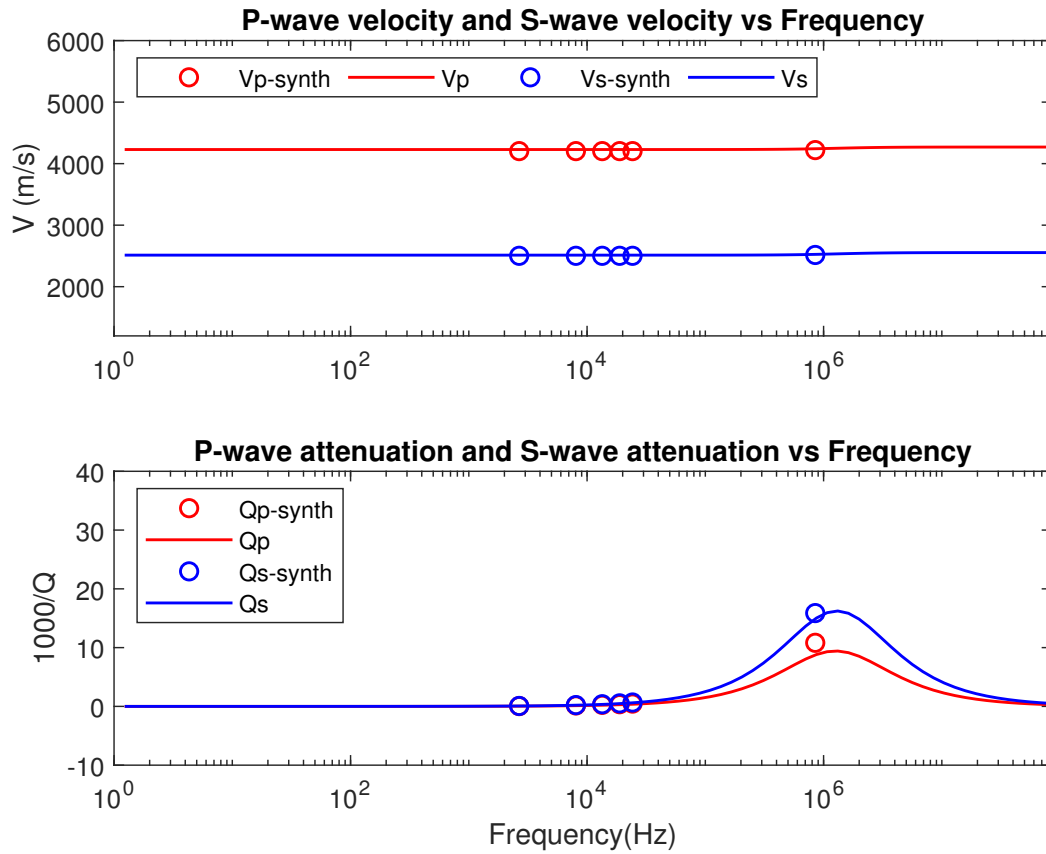


Figure 2.4: The effect of a positive perturbation of α_2 on the velocity and attenuation spectra of a rock model with two types of pores, using Xu and White model as a reference model, with model parameters of $[\alpha_1 = 0.15, \alpha_2 = 0.0625, \phi_2 = 0.00556, \tau_1 = \tau_2 = 1 \times 10^{-7} \text{ s}]$.

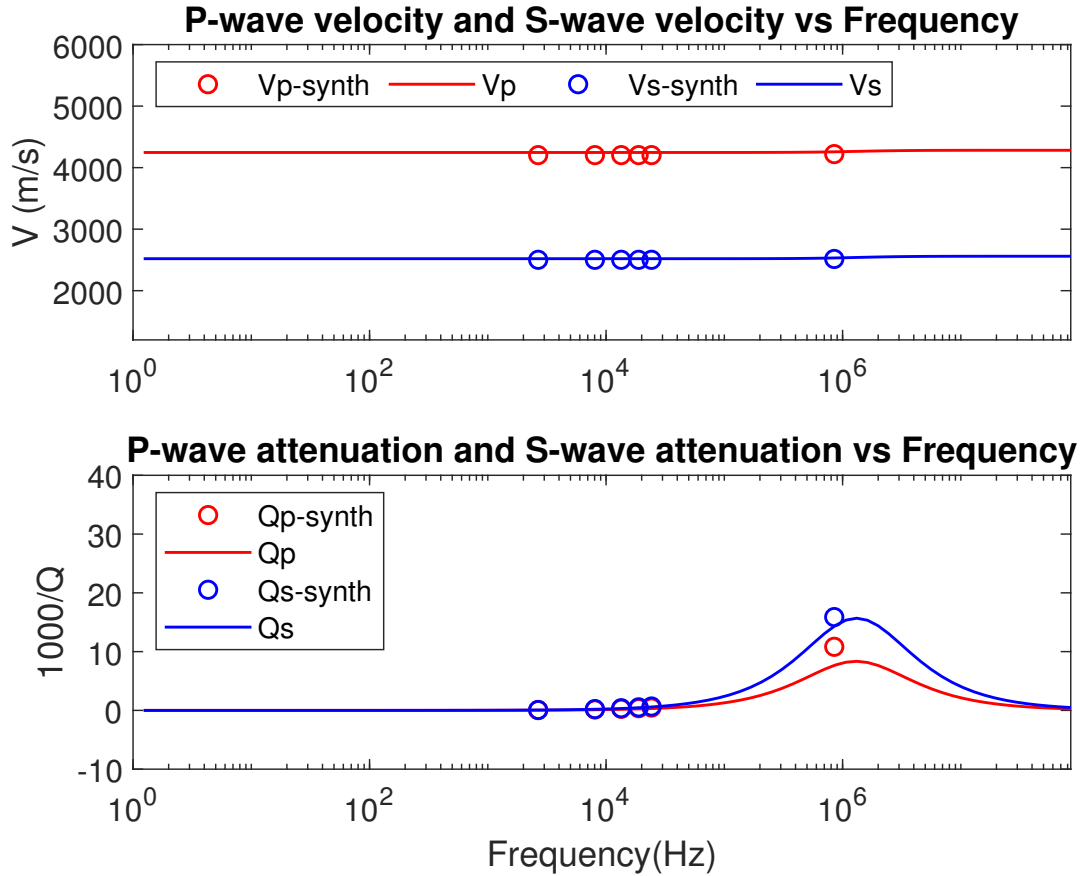


Figure 2.5: The maximum perturbation of α_2 , and how it affects the velocity and attenuation spectra of a rock model with two types of pores, using Xu and White model as a reference model, with model parameters of $[\alpha_1 = 0.15, \alpha_2 = 0.075, \phi_2 = 0.00556, \tau_1 = \tau_2 = 1 \times 10^{-7} \text{ s}]$.

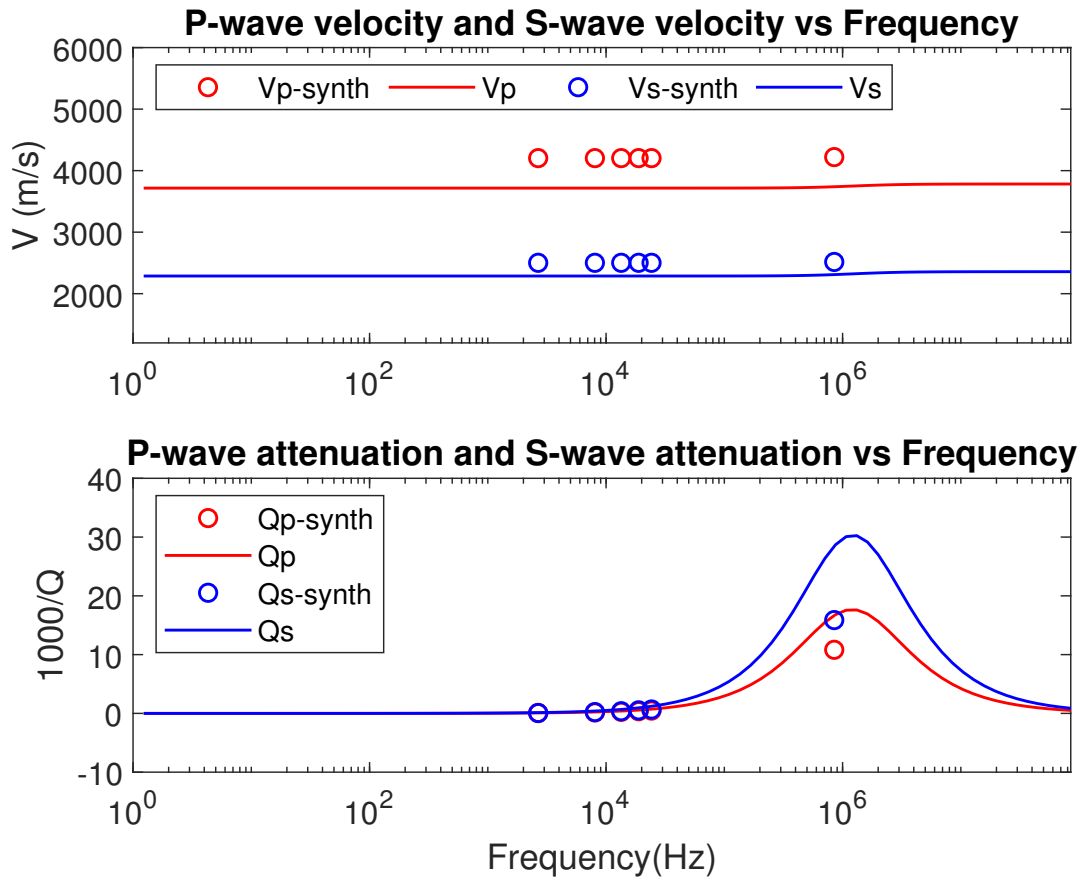


Figure 2.6: The effect of a negative perturbation of α_1 on the velocity and attenuation spectra of a rock model with two types of pores, using Xu and White model as a reference model, with model parameters of $[\alpha_1 = 0.1125, \alpha_2 = 0.05, \phi_2 = 0.00556, \tau_1 = \tau_2 = 1 \times 10^{-7} \text{ s}]$.

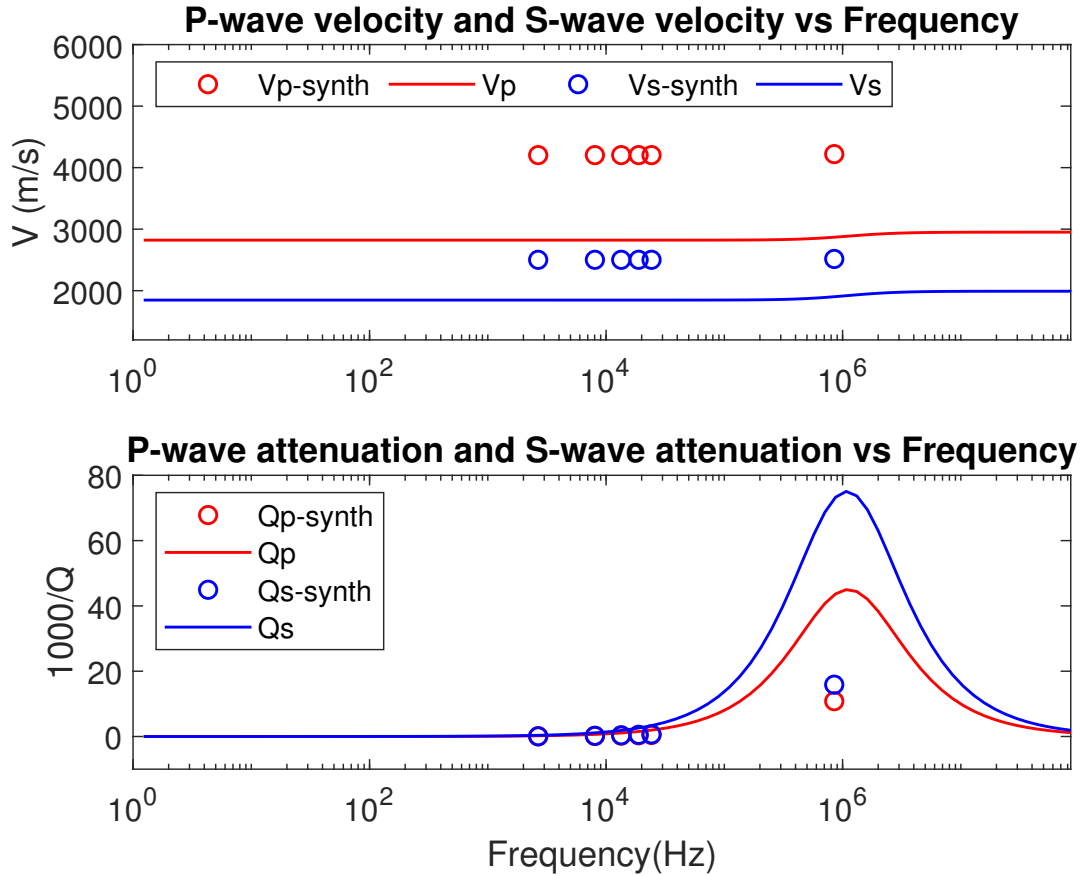


Figure 2.7: The minimum perturbation of α_1 , and how it affects the velocity and attenuation spectra of a rock model with two types of pores, using Xu and White model as a reference model, with model parameters of $[\alpha_1 = 0.075, \alpha_2 = 0.05, \phi_2 = 0.00556, \tau_1 = \tau_2 = 1 \times 10^{-7} \text{ s}]$.

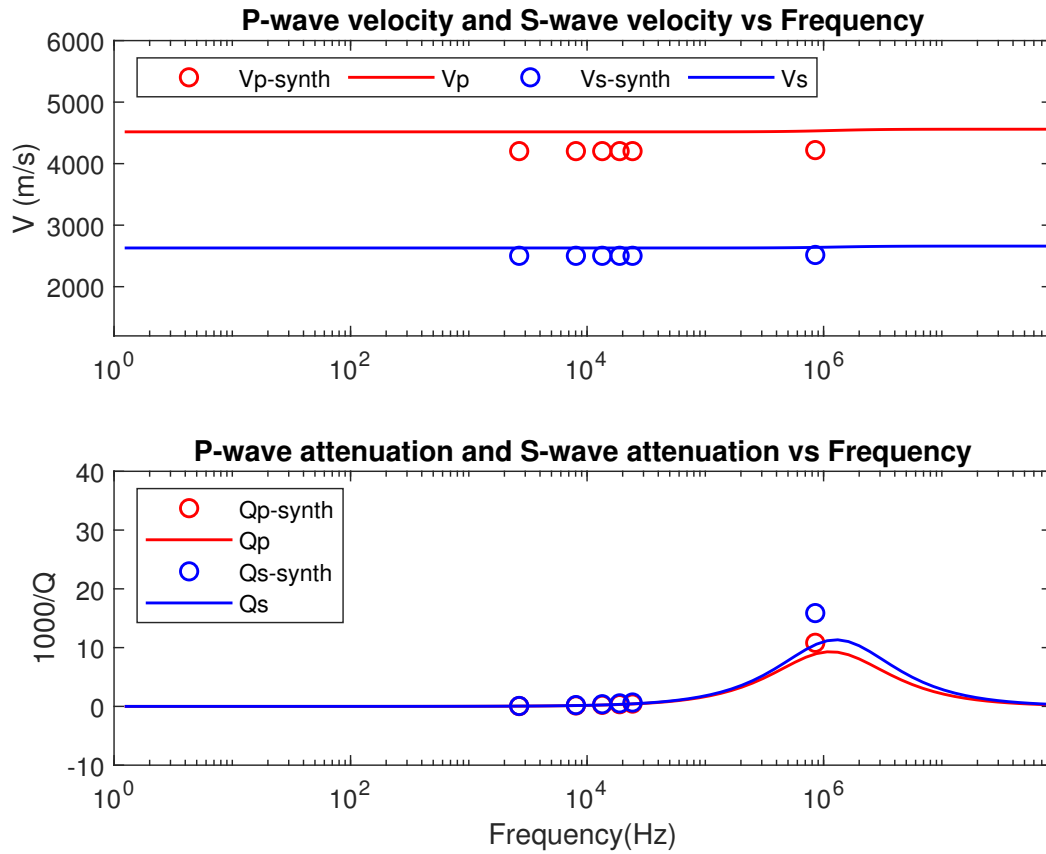


Figure 2.8: The effect of a positive perturbation of α_1 on the velocity and attenuation spectra of a rock model with two types of pores, using Xu and White model as a reference model, with model parameters of $[\alpha_1 = 0.1875, \alpha_2 = 0.05, \phi_2 = 0.00556, \tau_1 = \tau_2 = 1 \times 10^{-7} \text{ s}]$.

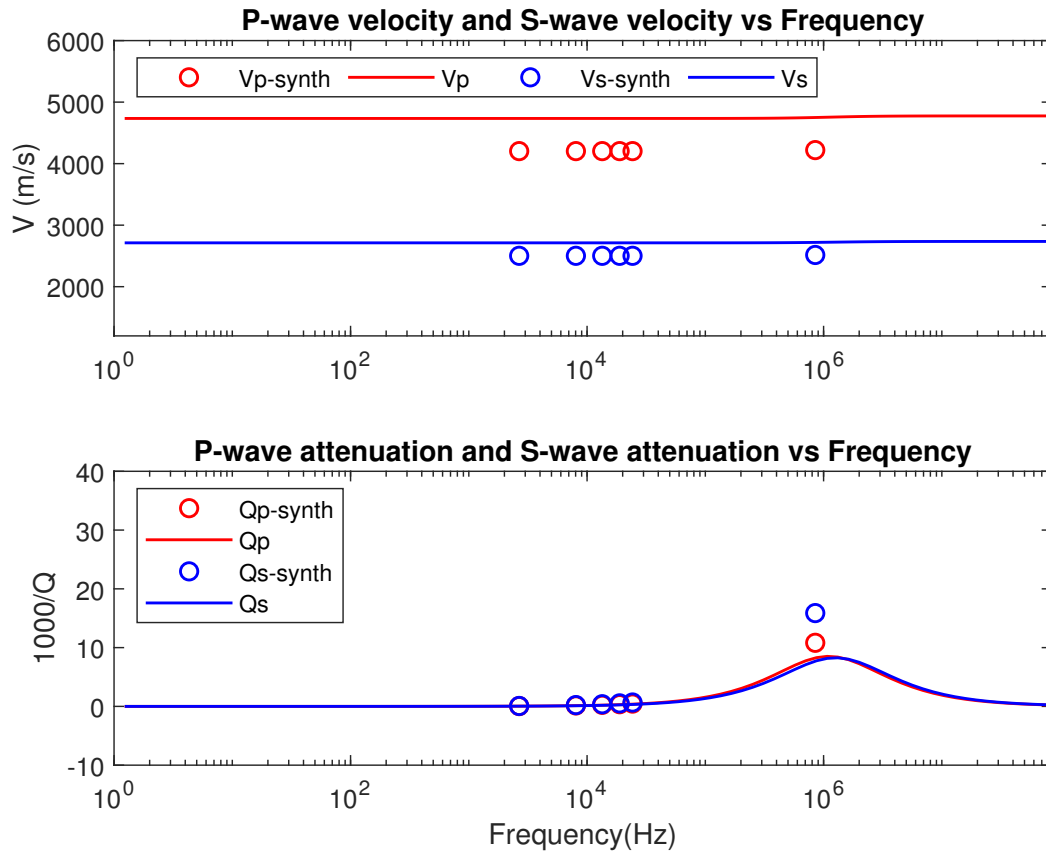


Figure 2.9: The maximum perturbation of α_1 , and how it affects the velocity and attenuation spectra of a rock model with two types of pores, using Xu and White model as a reference model, with model parameters of $[\alpha_1 = 0.225, \alpha_2 = 0.05, \phi_2 = 0.00556, \tau_1 = \tau_2 = 1 \times 10^{-7} \text{ s}]$.

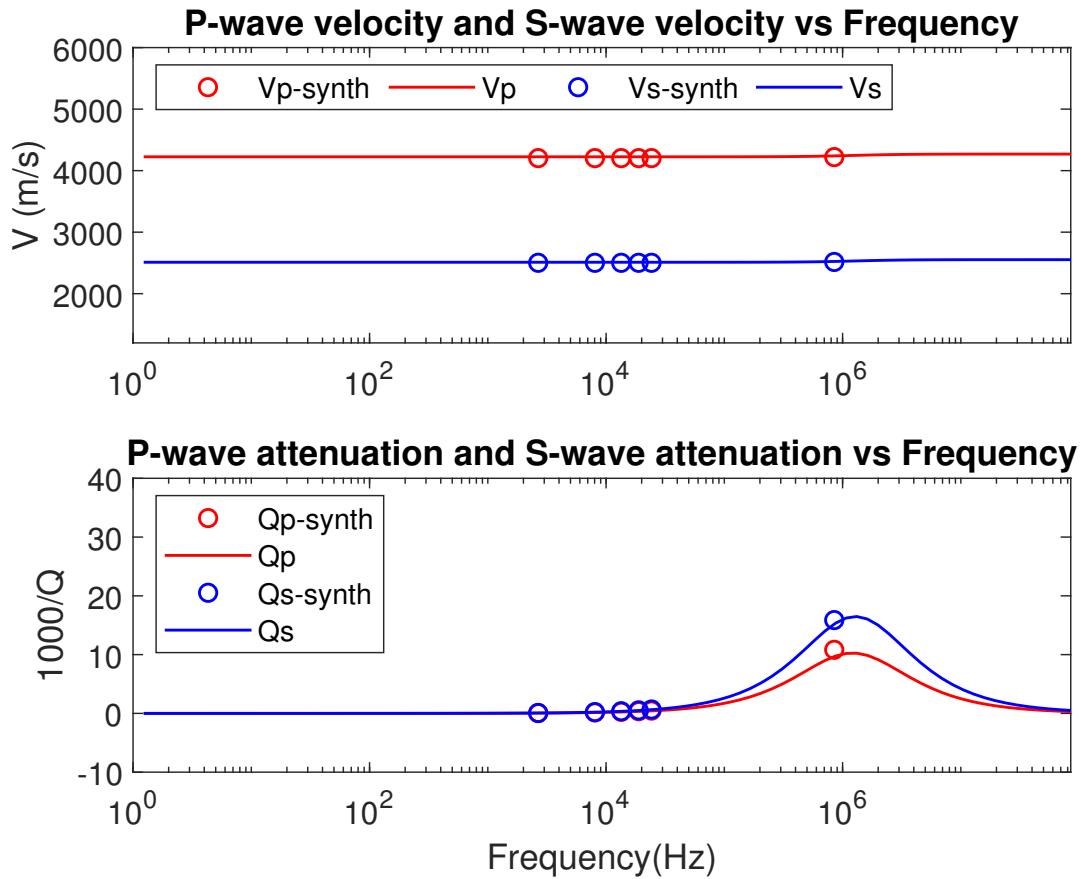


Figure 2.10: The effect of a negative perturbation of ϕ_2 on the velocity and attenuation spectra of a rock model with two types of pores, using Xu and White model as a reference model, with model parameters of $[\alpha_1 = 0.15, \alpha_2 = 0.05, \phi_2 = 0.00417, \tau_1 = \tau_2 = 1 \times 10^{-7} \text{ s}]$.

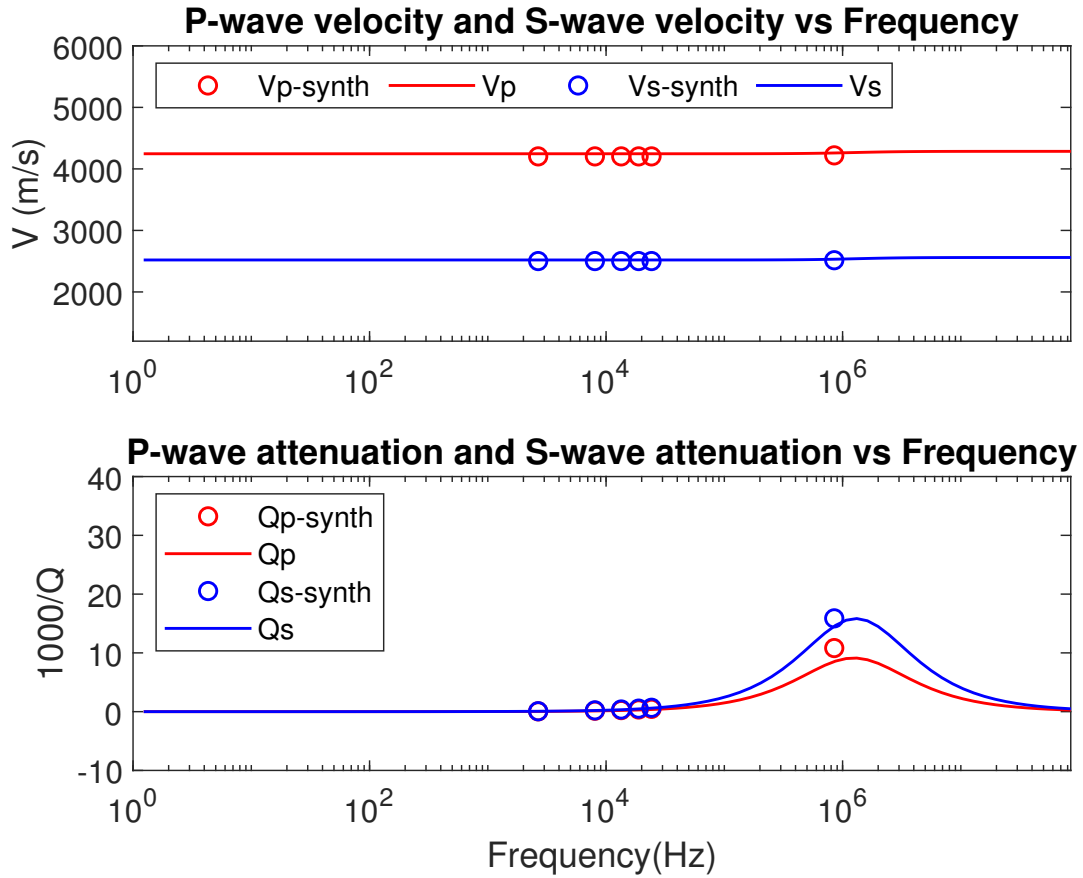


Figure 2.11: The minimum perturbation of ϕ_2 on the velocity and attenuation spectra of a rock model with two types of pores, using Xu and White model as a reference model, with model parameters of $[\alpha_1 = 0.15, \alpha_2 = 0.05, \phi_2 = 0.00278, \tau_1 = \tau_2 = 1 \times 10^{-7} \text{ s}]$.

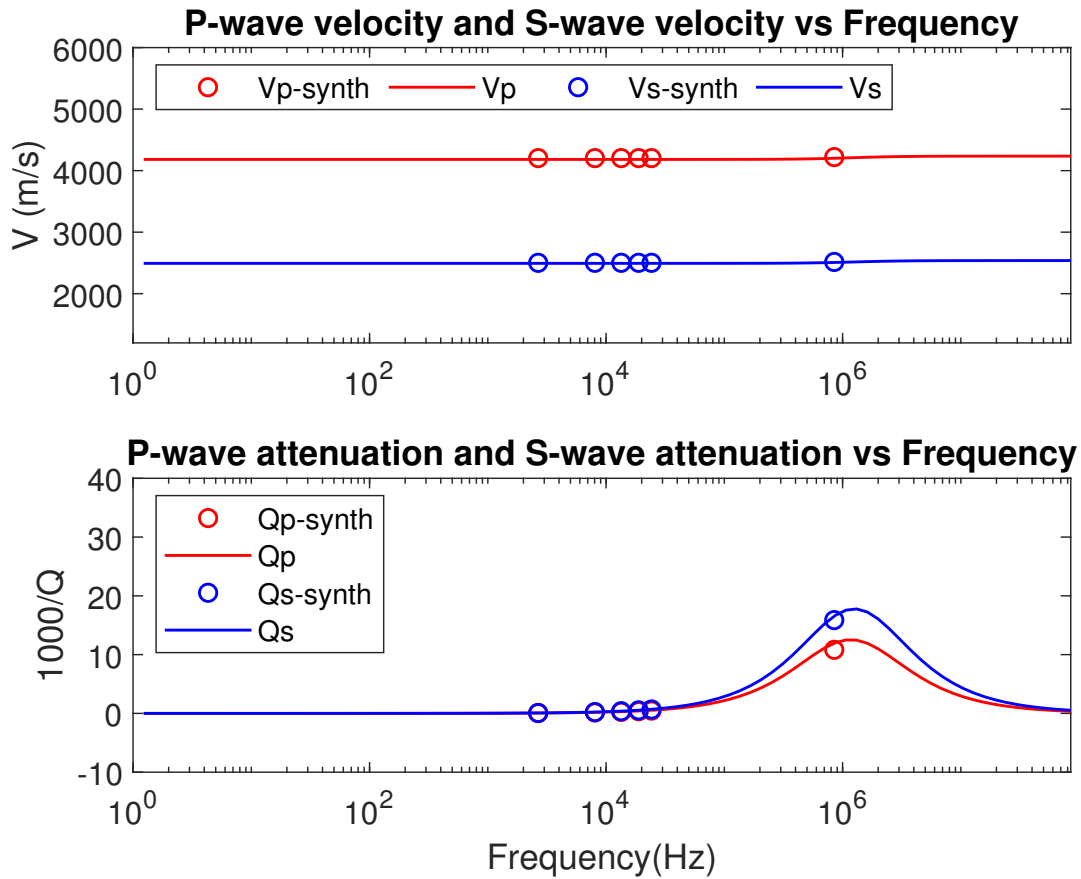


Figure 2.12: Illustration of the effect of a positive perturbation of ϕ_2 on the velocity and attenuation spectra of a rock model with two types of pores, using Xu and White model as a reference model, with model parameters of $[\alpha_1 = 0.15, \alpha_2 = 0.05, \phi_2 = 0.00696, \tau_1 = \tau_2 = 1 \times 10^{-7} \text{ s}]$.

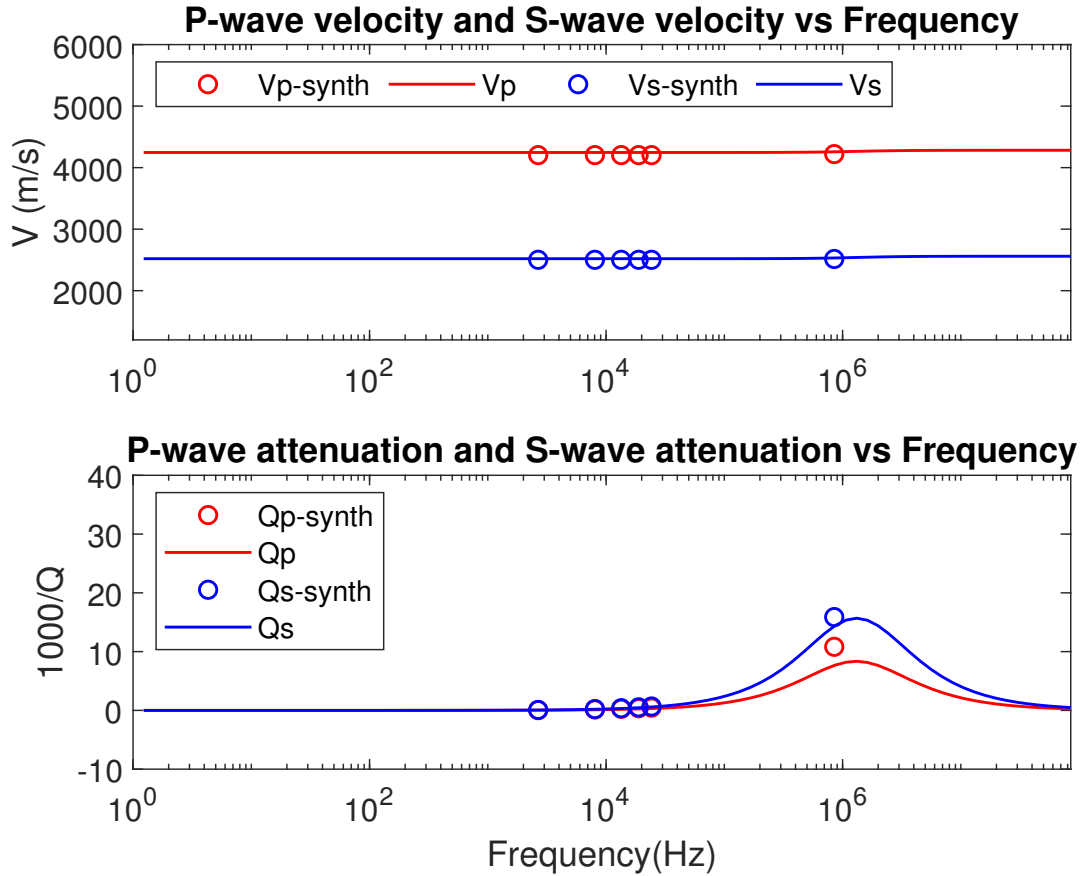


Figure 2.13: Illustration of the effect of the maximum perturbation of ϕ_2 on the velocity and attenuation spectra of a rock model with two types of pores, using Xu and White model as a reference model, with model parameters of $[\alpha_1 = 0.15, \alpha_2 = 0.05, \phi_2 = 0.0075, \tau_1 = \tau_2 = 1 \times 10^{-7} \text{ s}]$.

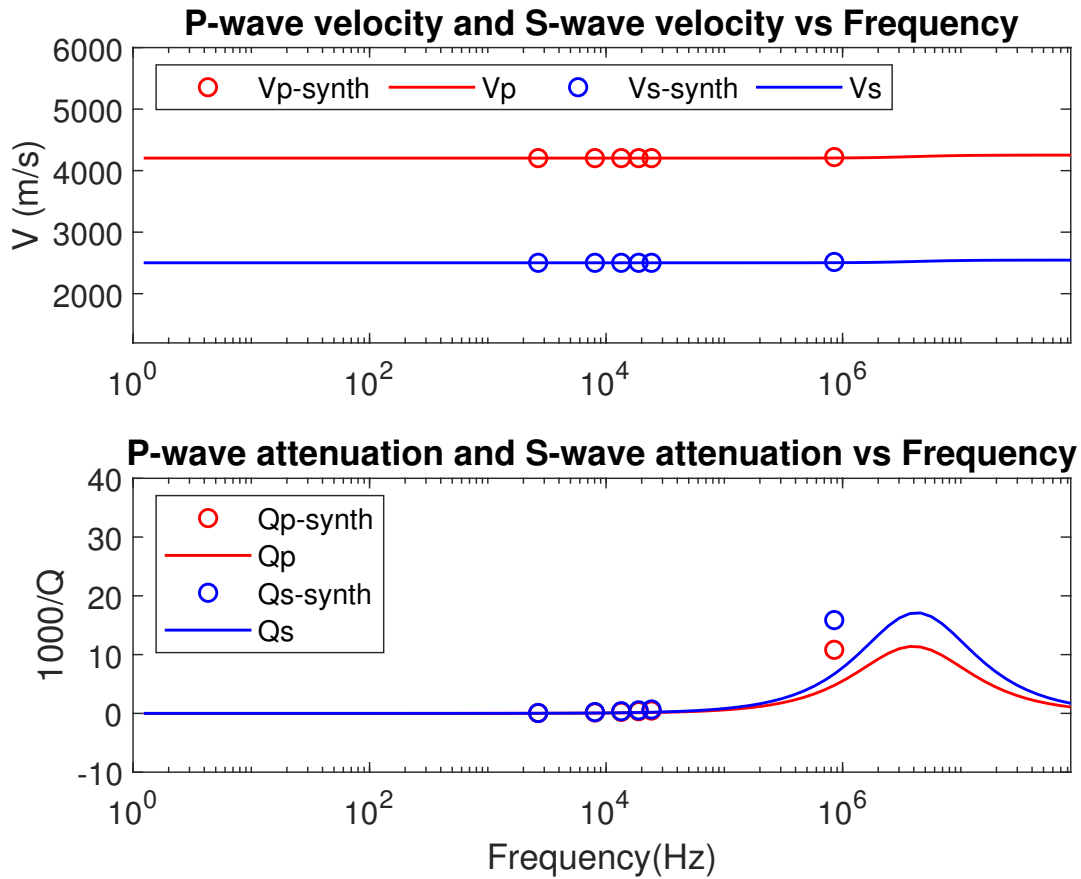


Figure 2.14: The effect of a negative perturbation of both τ_1 and τ_2 on the velocity and attenuation spectra of a rock model with two types of pores, using Xu and White model as a reference model, with model parameters of $[\alpha_1 = 0.15, \alpha_2 = 0.05, \phi_2 = 0.00556, \tau_1 = \tau_2 = 0.3 \times 10^{-7} \text{ s}]$.

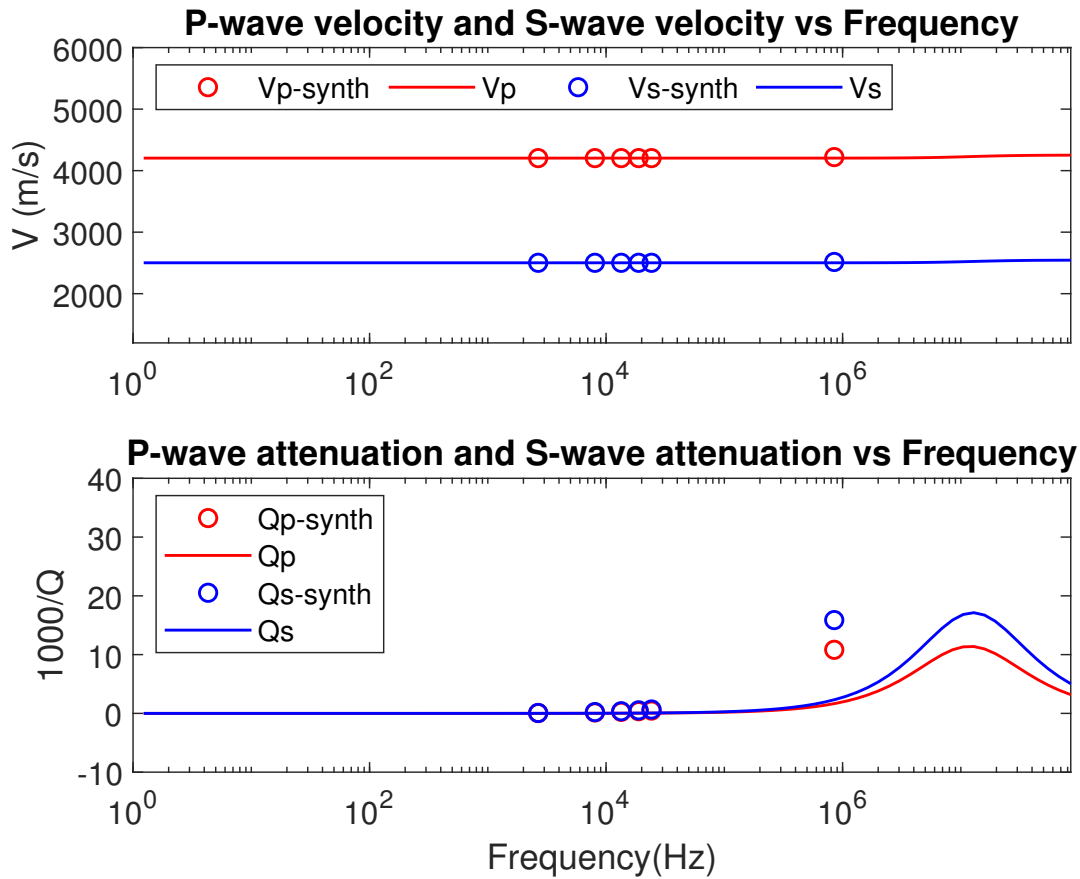


Figure 2.15: The minimum perturbation of τ_1 and τ_2 , and how it affect the velocity and attenuation spectra of a rock model with two types of pores, using Xu and White model as a reference model, with model parameters of $[\alpha_1 = 0.15, \alpha_2 = 0.05, \phi_2 = 0.00556, \tau_1 = 1 \times 10^{-8} \text{ s}, \tau_2 = 1 \times 10^{-8} \text{ s}]$.

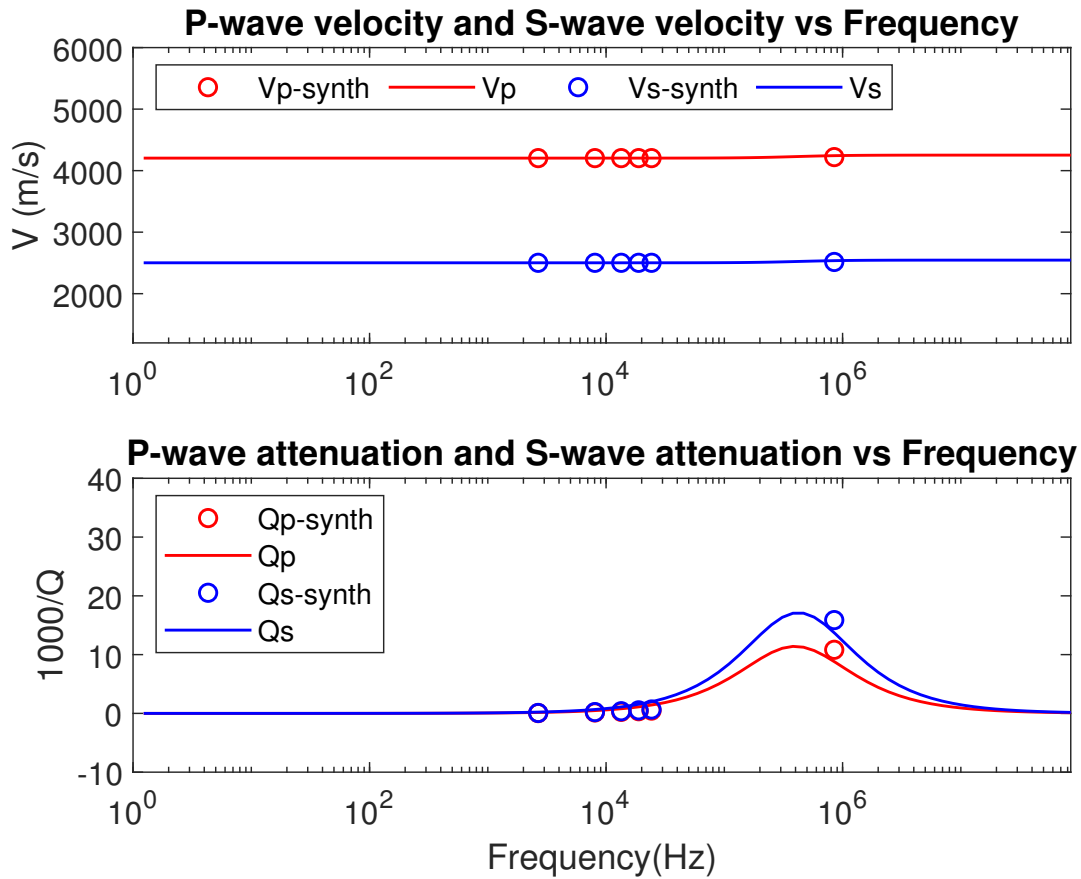


Figure 2.16: Illustration of the effect of a positive perturbation of τ_1 and τ_2 on the velocity and attenuation spectra of a rock model with two types of pores, using Xu and White model as a reference model, with model parameters of $[\alpha_1 = 0.15, \alpha_2 = 0.05, \phi_2 = 0.00556, \tau_1 = \tau_2 = 3 \times 10^{-7} \text{ s}]$.

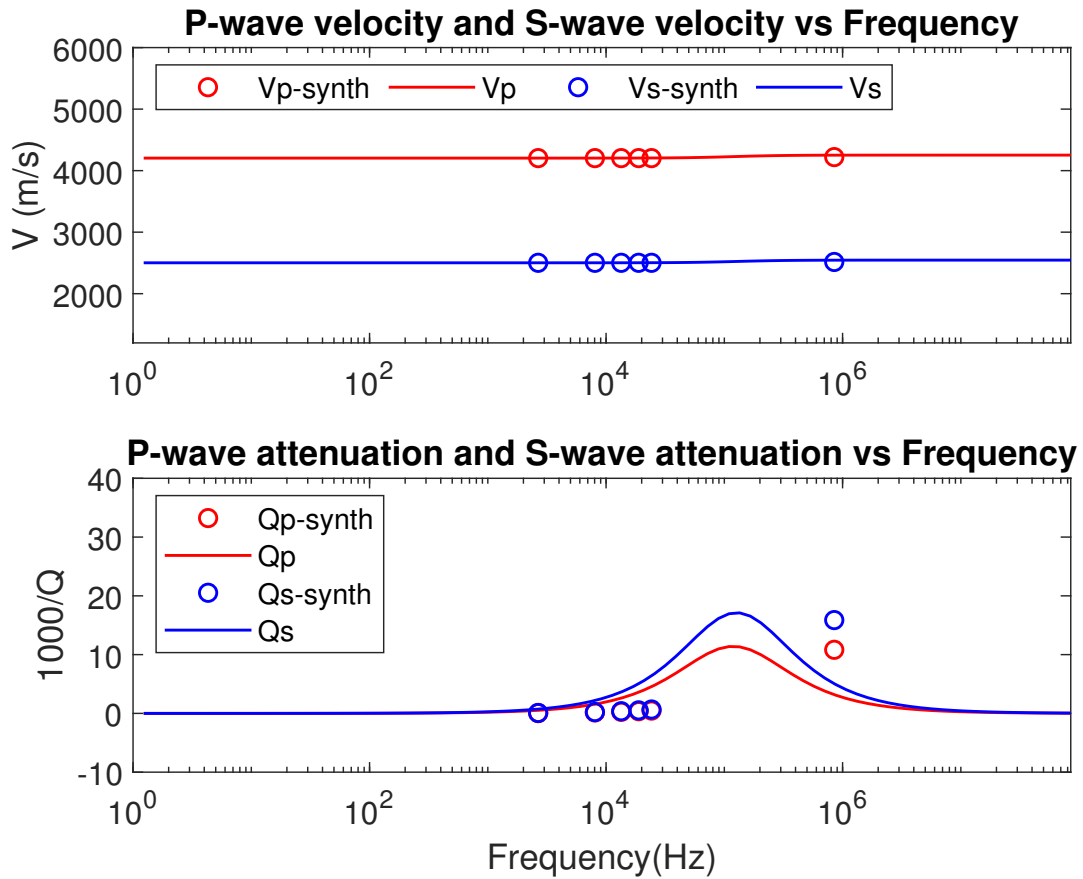


Figure 2.17: Illustration of the effect of the maximum perturbation of τ_1 and τ_2 on the velocity and attenuation spectra of a rock model with two types of pores, using Xu and White model as a reference model, with model parameters of $[\alpha_1 = 0.15, \alpha_2 = 0.05, \phi_2 = 0.00556, \tau_1 = 1 \times 10^{-6} \text{ s}, \tau_2 = 1 \times 10^{-6} \text{ s}]$.

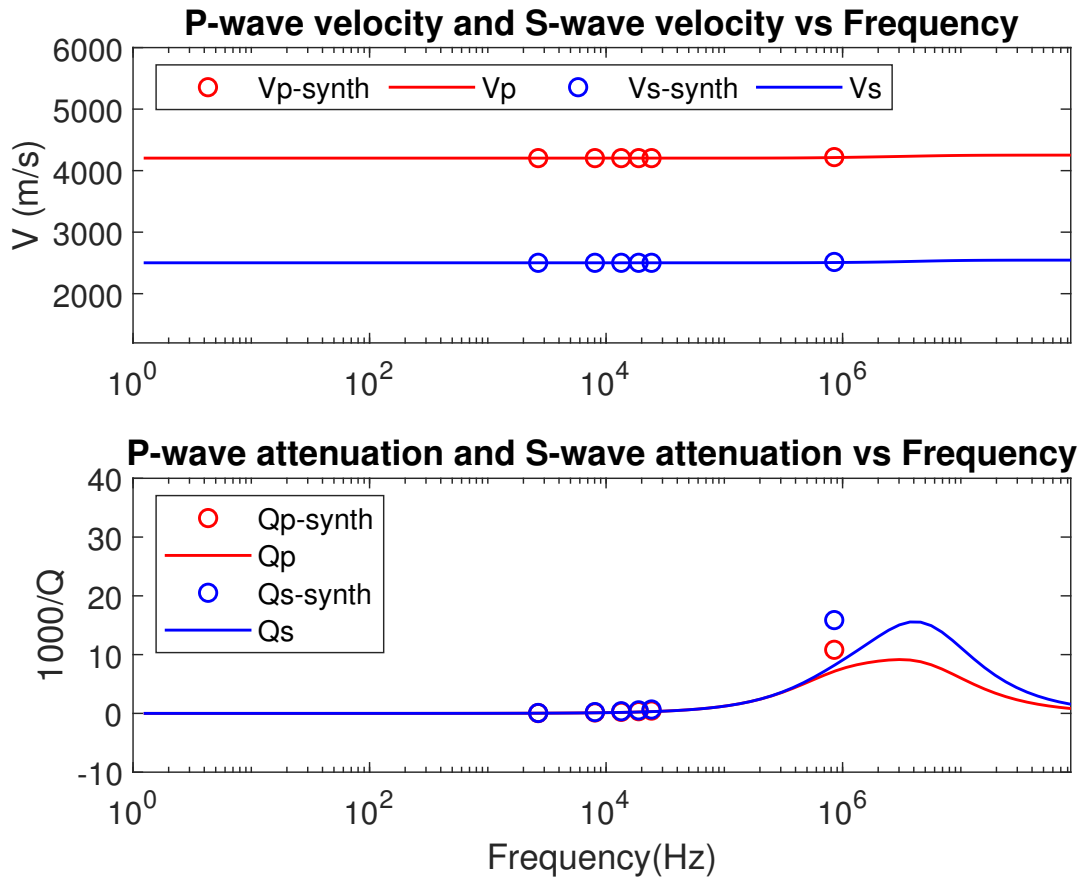


Figure 2.18: The effect of a negative perturbation of τ_1 on the velocity and attenuation spectra of a rock model with two types of pores, using Xu and White model as a reference model, with model parameters of $[\alpha_1 = 0.15, \alpha_2 = 0.05, \phi_2 = 0.00556, \tau_1 = 0.3 \times 10^{-7} \text{ s}, \tau_2 = 1 \times 10^{-7} \text{ s}]$.

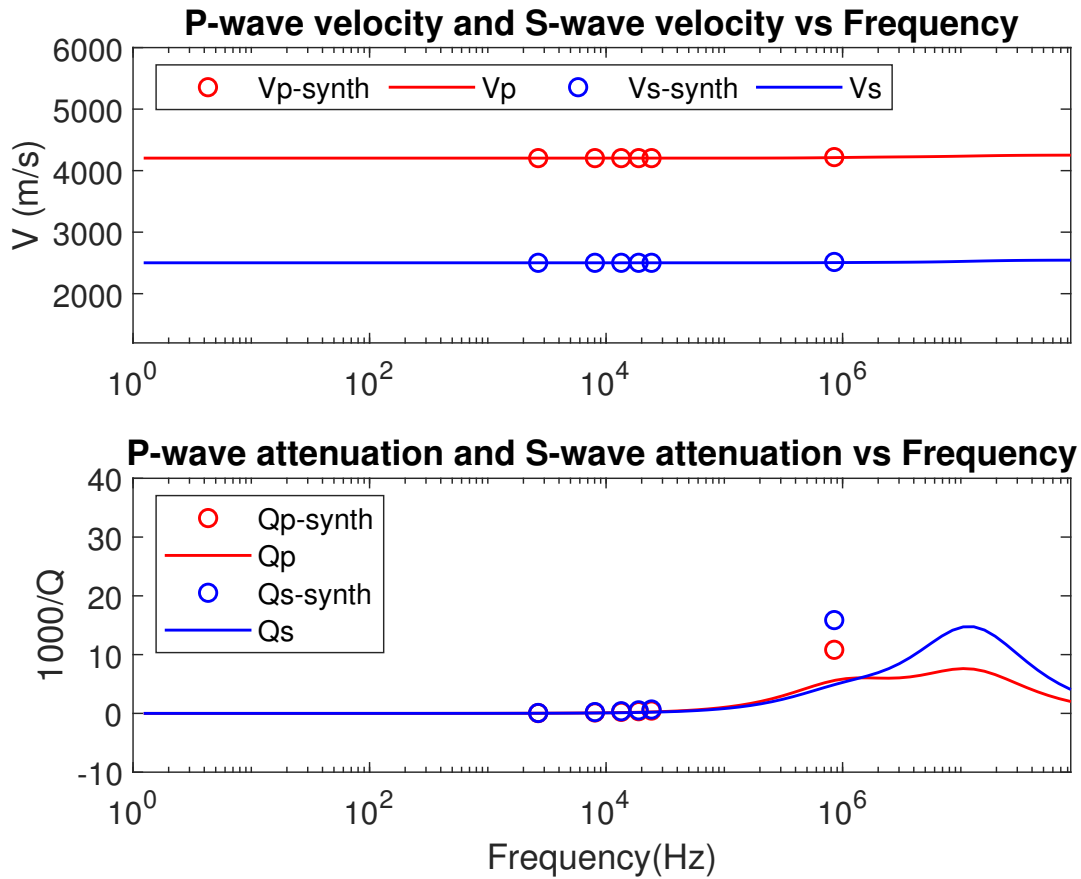


Figure 2.19: The minimum perturbation of τ_1 , and how it affects the velocity and attenuation spectra of a rock model with two types of pores, using Xu and White model as a reference model, with model parameters of $[\alpha_1 = 0.15, \alpha_2 = 0.05, \phi_2 = 0.00556, \tau_1 = 1 \times 10^{-8} \text{ s}, \tau_2 = 1 \times 10^{-7} \text{ s}]$.

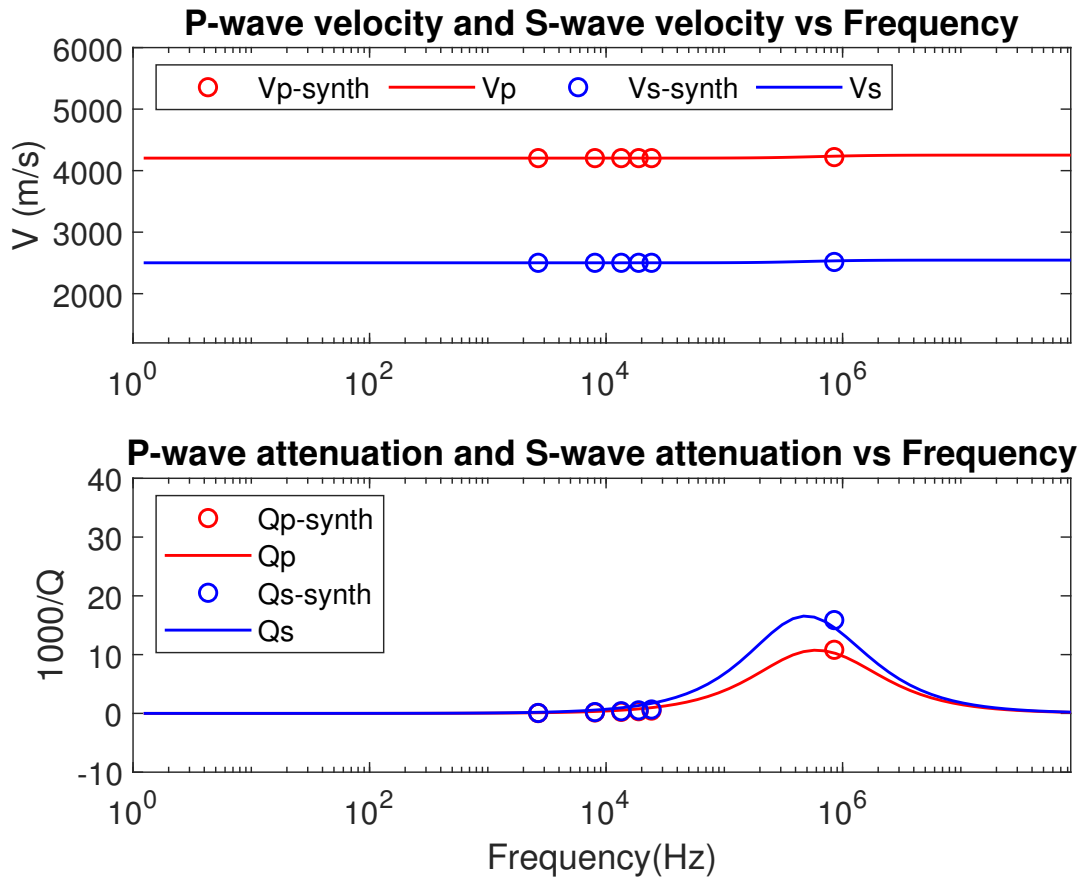


Figure 2.20: The effect of a positive perturbation of τ_1 on the velocity and attenuation spectra of a rock model with two types of pores, using Xu and White model as a reference model, with model parameters of $[\alpha_1 = 0.15, \alpha_2 = 0.05, \phi_2 = 0.00556, \tau_1 = 3 \times 10^{-7} \text{ s}, \tau_2 = 1 \times 10^{-7} \text{ s}]$.

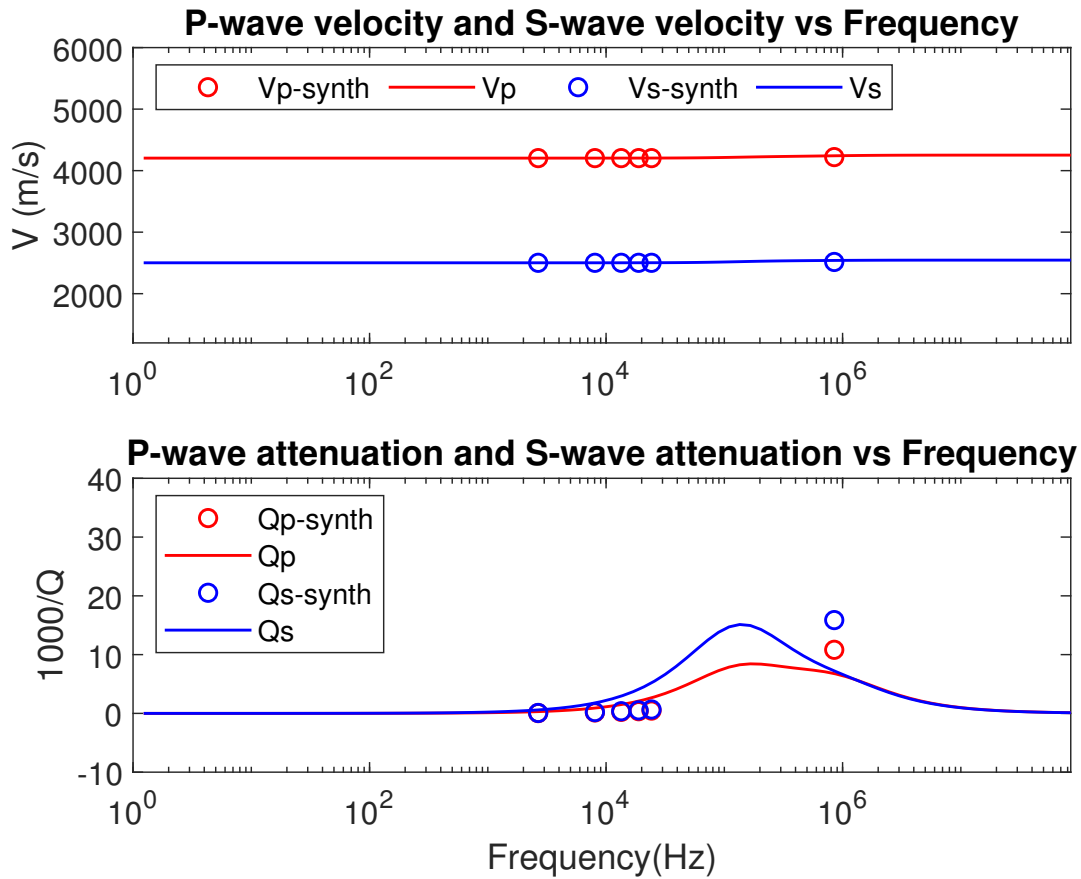


Figure 2.21: The maximum perturbation of τ_1 , and how it affects the velocity and attenuation spectra of a rock model with two types of pores, using Xu and White model as a reference model, with model parameters of $[\alpha_1 = 0.15, \alpha_2 = 0.05, \phi_2 = 0.00556, \tau_1 = 1 \times 10^{-6} \text{ s}, \tau_2 = 1 \times 10^{-7} \text{ s}]$.

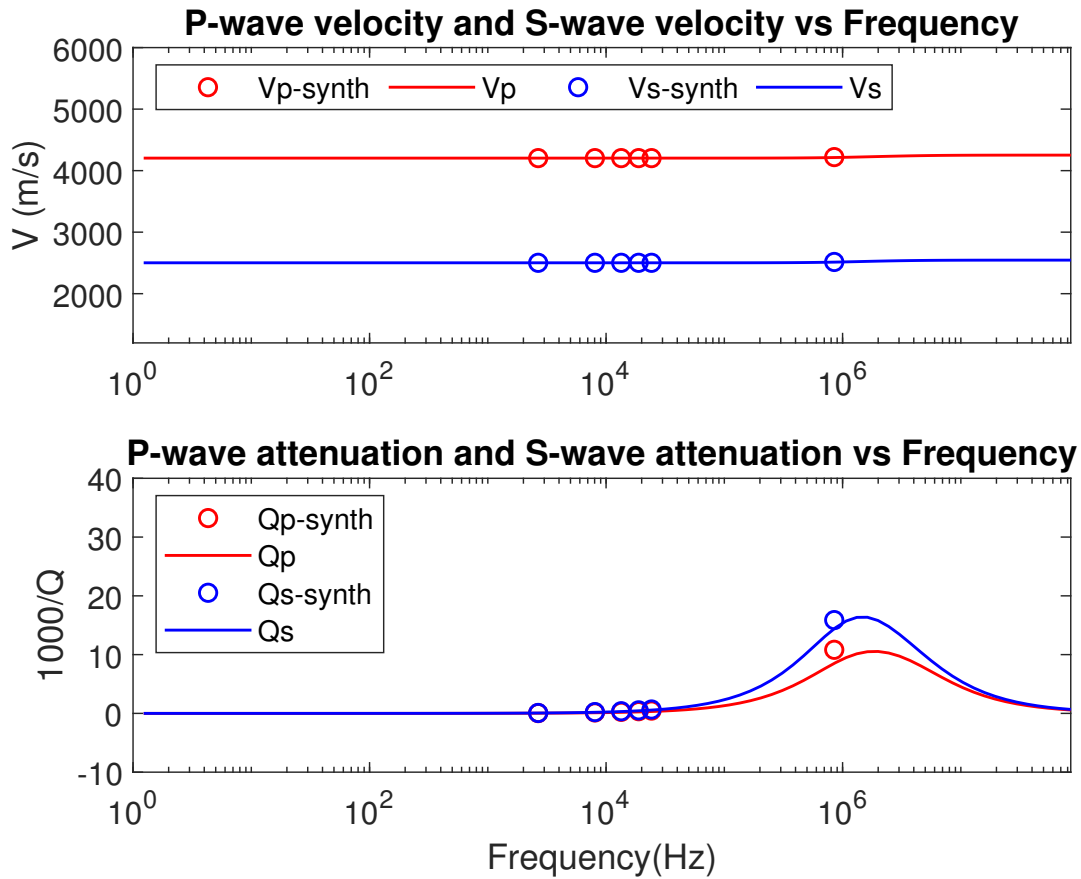


Figure 2.22: Illustration of the effect of a negative perturbation of τ_2 on the velocity and attenuation spectra of a rock model with two types of pores, using Xu and White model as a reference model, with model parameters of $[\alpha_1 = 0.15, \alpha_2 = 0.05, \phi_2 = 0.00556, \tau_1 = 1 \times 10^{-7} \text{ s}, \tau_2 = 0.3 \times 10^{-7} \text{ s}]$.

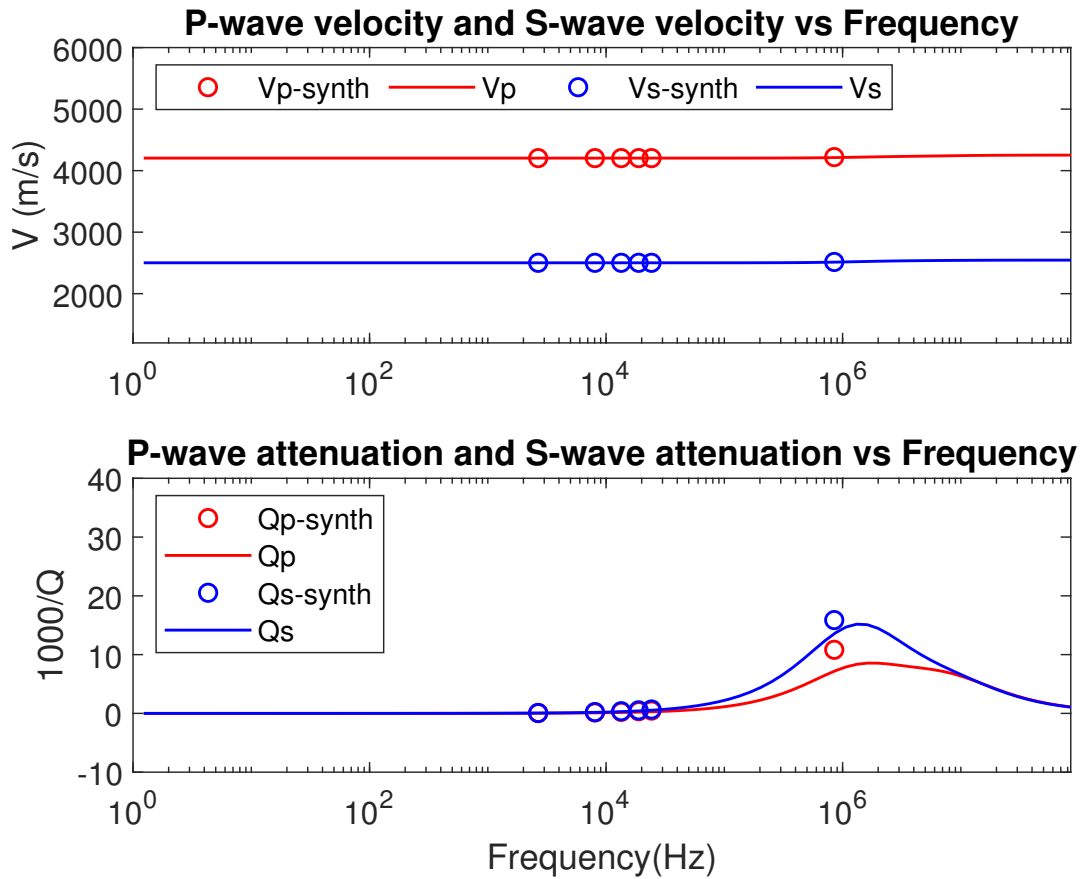


Figure 2.23: Illustration of the effect of the minimum perturbation of τ_2 on the velocity and attenuation spectra of a rock model with two types of pores, using Xu and White model as a reference model, with model parameters of $[\alpha_1 = 0.15, \alpha_2 = 0.05, \phi_2 = 0.00556, \tau_1 = 1 \times 10^{-7} \text{ s}, \tau_2 = 1 \times 10^{-8} \text{ s}]$.

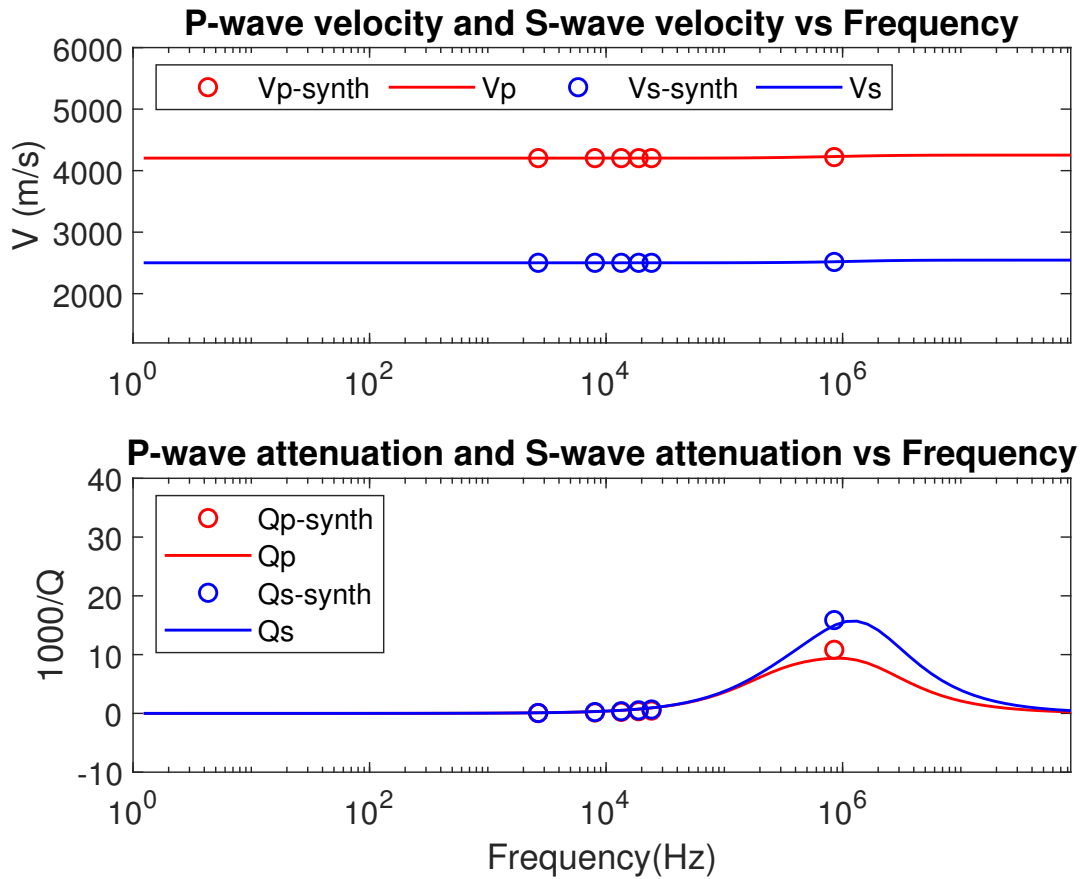


Figure 2.24: The effect of a positive perturbation of τ_2 on the velocity and attenuation spectra of a rock model with two types of pores, using Xu and White model as a reference model, with model parameters of $[\alpha_1 = 0.15, \alpha_2 = 0.05, \phi_2 = 0.00556, \tau_1 = 1 \times 10^{-7} \text{ s}, \tau_2 = 3 \times 10^{-7} \text{ s}]$.

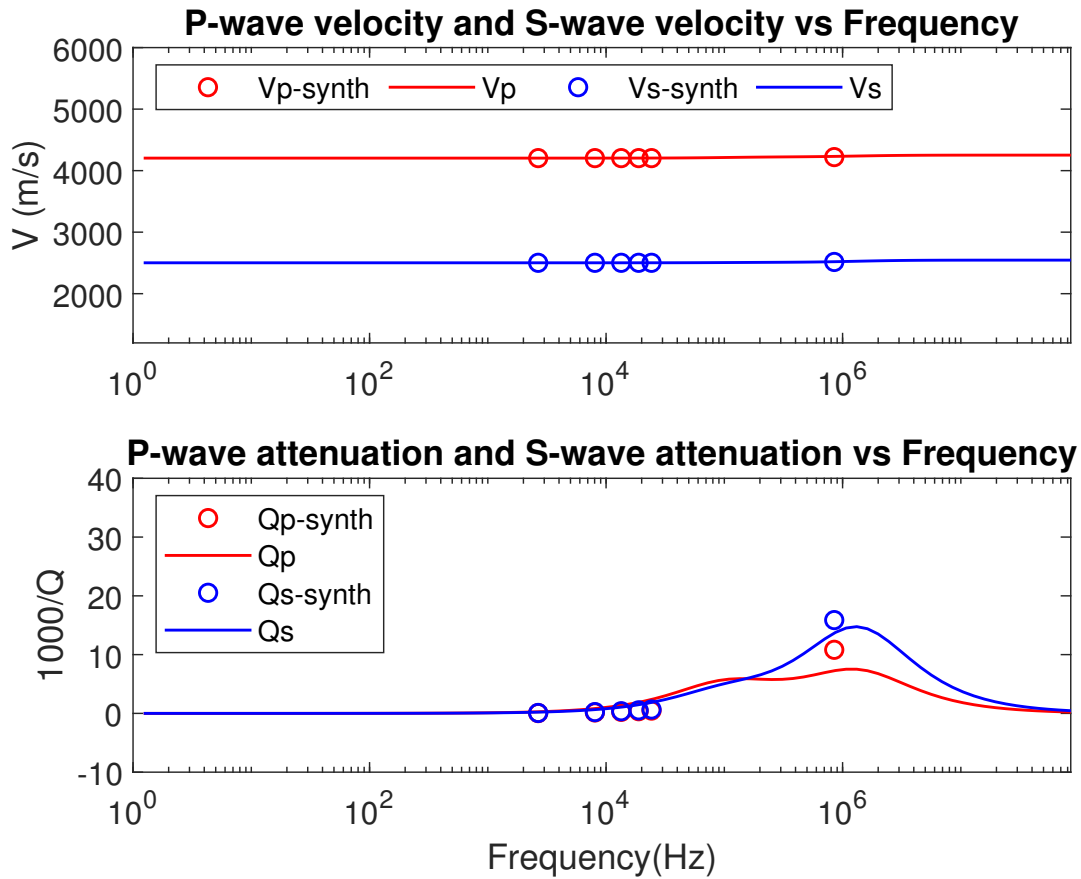


Figure 2.25: The maximum perturbation of τ_2 , and how it affects the velocity and attenuation spectra of a rock model with two types of pores, using Xu and White model as a reference model, with model parameters of $[\alpha_1 = 0.15, \alpha_2 = 0.05, \phi_2 = 0.00556, \tau_1 = 1 \times 10^{-7} \text{ s}, \tau_2 = 1 \times 10^{-6} \text{ s}]$.

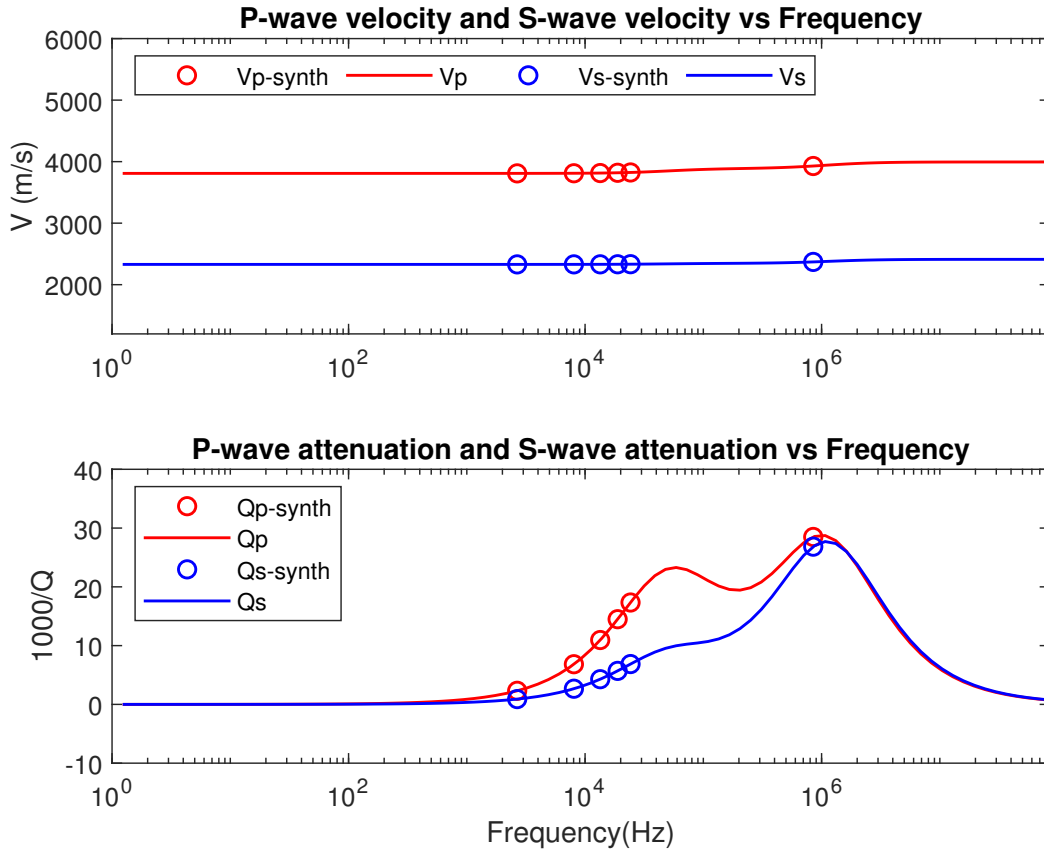


Figure 2.26: Theoretical predictions of the velocity and attenuation spectra of a water saturated rock model with three types of pores, this is the reference model, which the visco-elastic generalized Xu and White model [$\alpha_1 = 0.15$, $\alpha_2 = 0.05$, $\alpha_3 = 0.001$ $\phi_2 = 0.00556$, $\phi_3 = \alpha_3/10$, $\tau_1 = \tau_2 = \tau_3 = 1 \times 10^{-7}$ s].

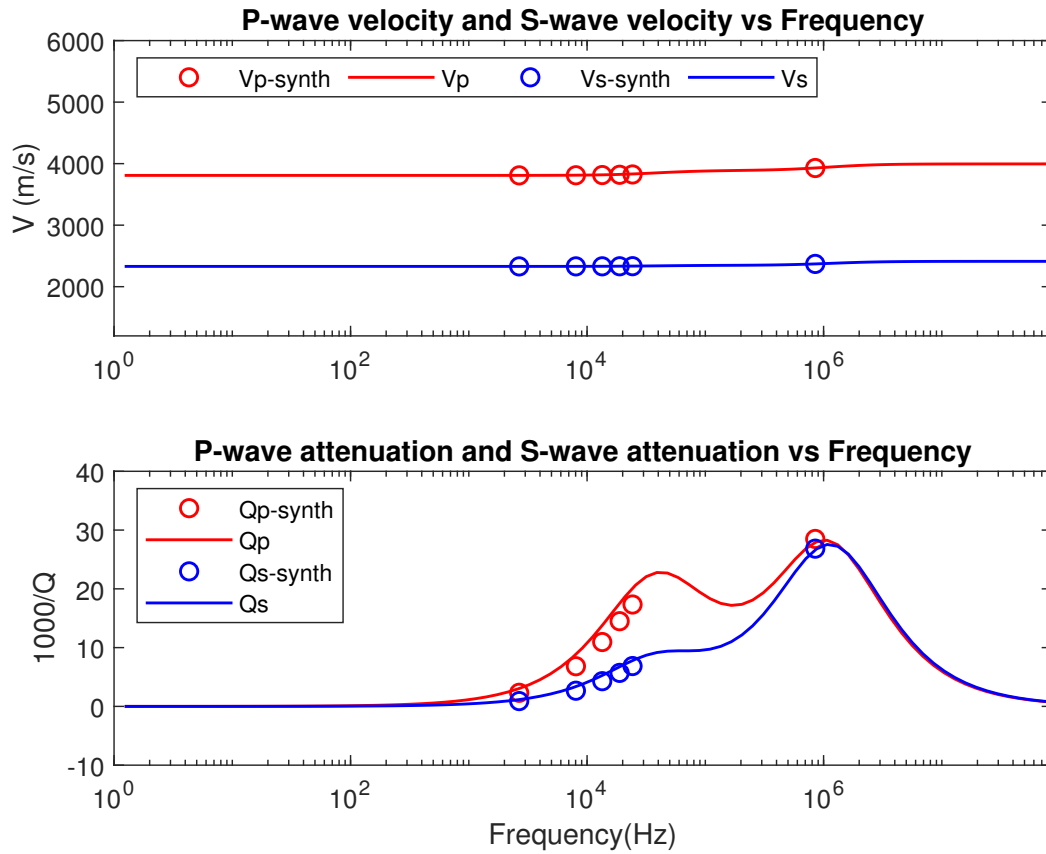


Figure 2.27: The effect of a negative perturbation of α_3 on the velocity and attenuation spectra of a rock model with three types of pores, using more complex Xu and White model, with model parameters of $[\alpha_1 = 0.15, \alpha_2 = 0.05, \alpha_3 = 0.00075, \phi_2 = 0.00556, \phi_3 = \alpha_3/10, \tau_1 = \tau_2 = \tau_3 = 1 \times 10^{-7} \text{ s}]$.

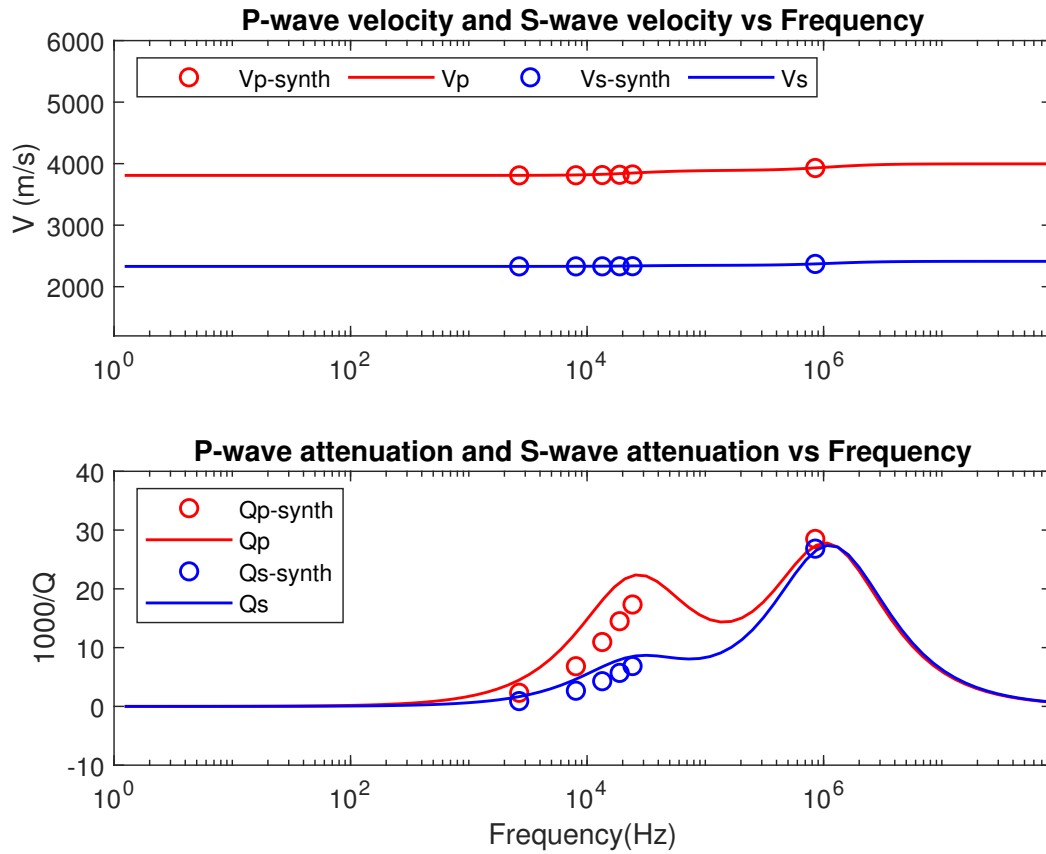


Figure 2.28: The effect of the minimum negative perturbation of α_3 on the velocity and attenuation spectra of a rock model with three types of pores, using more complex Xu and White model, with model parameters of [$\alpha_1 = 0.15$, $\alpha_2 = 0.05$, $\alpha_3 = 0.0005$ $\phi_2 = 0.00556$, $\phi_3 = \alpha_3/10$, $\tau_1 = \tau_2 = \tau_3 = 1 \times 10^{-7}$ s].

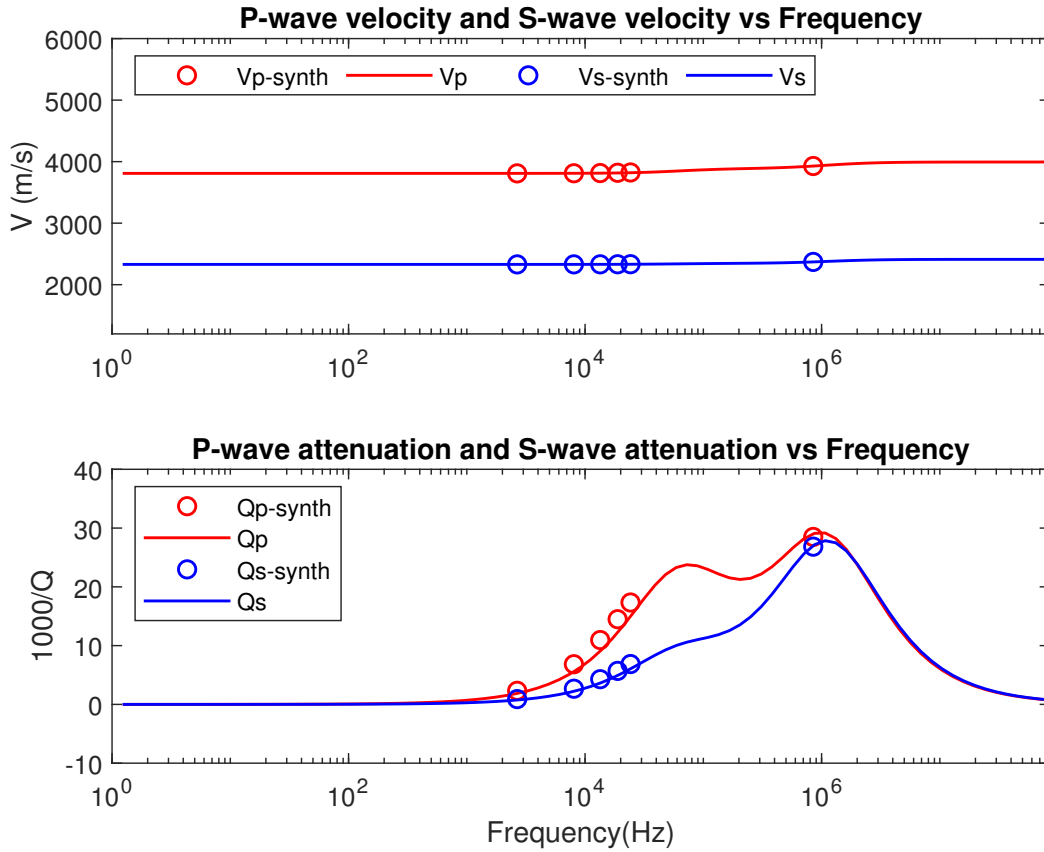


Figure 2.29: The effect of a positive perturbation of α_3 on the velocity and attenuation spectra of a rock model with three types of pores, using more complex Xu and White model, with model parameters of $[\alpha_1 = 0.15, \alpha_2 = 0.05, \alpha_3 = 0.00125, \phi_2 = 0.00556, \phi_3 = \alpha_3/10, \tau_1 = \tau_2 = \tau_3 = 1 \times 10^{-7} \text{ s}]$.

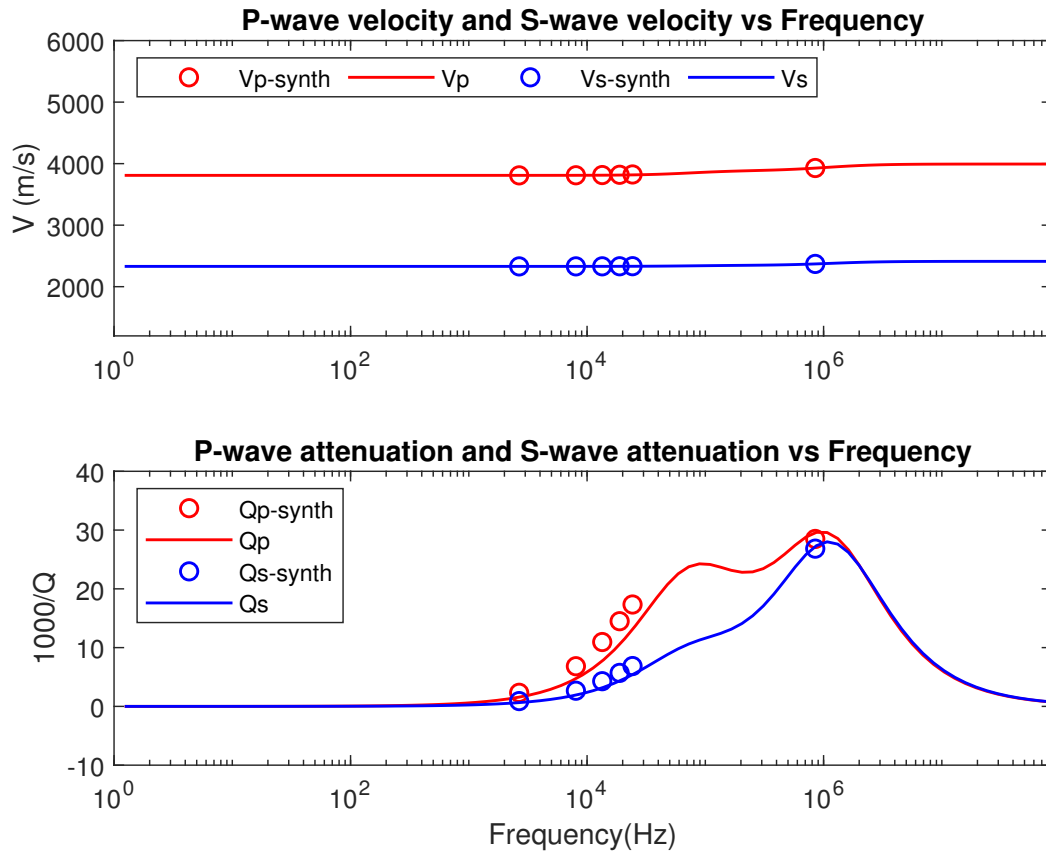


Figure 2.30: The maximum positive perturbation of α_3 , and how it affects the velocity and attenuation spectra of a rock model with three types of pores, using more complex Xu and White model, with model parameters of $[\alpha_1 = 0.15, \alpha_2 = 0.05, \alpha_3 = 0.0015, \phi_2 = 0.00556, \phi_3 = \alpha_3/10, \tau_1 = \tau_2 = \tau_3 = 1 \times 10^{-7} \text{ s}]$.

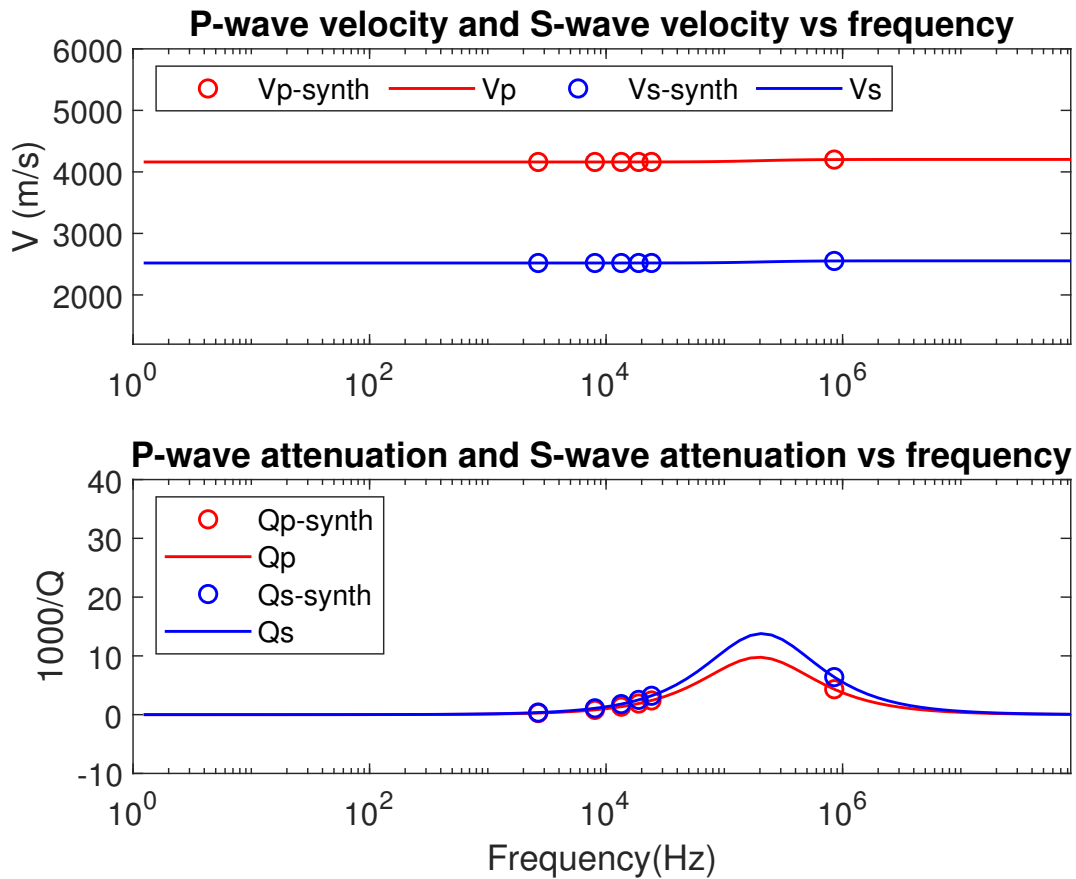


Figure 2.31: Pore-fluid substitution effects, when substituting water with oil for the model of two pore types. The reference model in the water saturated visco-elastic model shown in Figure 2.1.

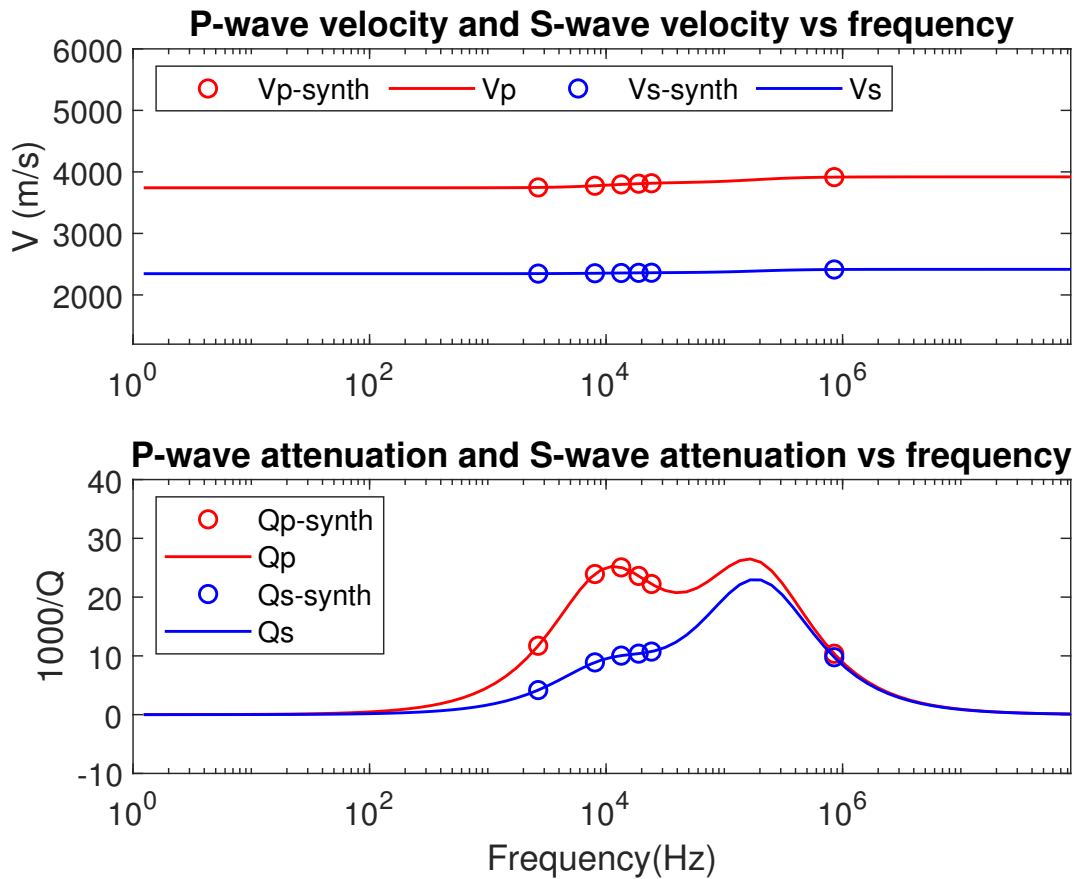


Figure 2.32: Fluid substitution effects, when substituting water with oil for the model of three pore types. The reference model in the water saturated visco-elastic model shown in Figure 2.26.

Chapter 3

Rock Physics Inversion

3.1 The Non-linear Inverse Problem

The goal of inversion in general is to find models that explain observations. Thus, model-based inversion, as introduced in Section ??, aims to deduce model parameters by iteratively fitting observations with theoretical predictions from trial models (Sen and Stoffa, 2013). Inversion has been used to provide unique and powerful results of estimating physical models from data in geophysics and rock physics, such as in seismic tomography, reservoir characterization, and monitoring. As the seismic velocities carry beneficial information of the underground that can be inverted. One can produce a map of microstructures properties out of the corresponding acoustic properties (Jakobsen et al., 2021), which helps for studying the underground. Using parameter estimation and inverse problem, engineers and scientists regularly link physical parameters characterizing a model, \mathbf{m} , with a set of data, \mathbf{d} , (Aster et al., 2018). The data can be predicted theoretically (model-based inversion) or collected by some observation (inverse problems). For problems where the data is often a function of time and/or space, or a collection of discrete observations, and the model parameters and data are vectors, we can use a non-linear system of algebraic equation (\mathbf{G}) to get the following non-linear functional relation (Aster et al., 2018):

$$\mathbf{G}(\mathbf{m}) = \mathbf{d}. \tag{3.1}$$

By making use of the non-linear inverse equation above, Eq. 3.1, the model parameters are related to both the theoretically calculated, discussed in Section ??, and observed data as discussed in Section 3.4, hence, a non-linear rock physics inversions, using a microstructural visco-elastic models, are carried out. The inversion is done for the calculated and

observed velocity and attenuation with respect to the microstructural parameters (i.e. α_i , ϕ_i , and τ_i).

Eq. 3.2 assumed to be the vector of data, \mathbf{d} , measured at N different frequencies for a set of complex porous media. The sets of communicating cavities (pores and cracks) are considered to be the inclusion of the complex porous media being studied, are divided into families of communicating cavities, labelled by $r = 1, \dots, N_c$, then the model parameters assumed to be \mathbf{m} and organised in Eq. 3.3. A cost function $E(\mathbf{m})$, which calculates the data mismatch, using both L1-norm and L2-norm, is used as in Eq. 3.4.

$$\mathbf{d} = [V_p^1, \dots, V_p^N, V_s^1, \dots, V_s^N, Q_p^1, \dots, Q_p^N, \dots, Q_s^1, \dots, Q_s^N]^T. \quad (3.2)$$

$$\mathbf{m} = [\alpha_1, \dots, \alpha_{(N_c)}, \dots, \phi_1, \dots, \phi_{(N_c)}, \tau_1, \dots, \tau_{(N_c)}, X_p, X_s]^T, \quad (3.3)$$

and

$$E(\mathbf{m}) = \frac{\|W(\mathbf{d} - G(\mathbf{m}))\|_1}{\|\mathbf{d}\|_1}, \quad (3.4)$$

where $\|\cdot\|_1$ denotes the L1-norm, and W denotes the diagonal weight matrix.

Although several works have shown no significant difference in the results between the misfit of the L1-norm and the L2-norm in Eq. 3.4 above, (Izumotani and Onozuka, 2013), some scientist prefer to use the L1-norm, since it is known to be more robust concerning data outliers, than the L2-norm (Tarantola, 2005). However, the L1-norm may sometimes treat the sparse ultrasonic data like outliers. For this reason, some others may prefer to use the L2-norm (Jakobsen et al., 2021). Thus, it seems, both the L1 and the L2 norm can be used based on difference considerations and assumptions, in this thesis, both the L1-norm and the L2-norm is employed. The L1-norm is used in the synthetic data inversion, Section 3.3 inversynthetic, while both L1 and L2 norm are employed in the real data inversion, Section 3.4, and the results are compared. More discussion and the comparison between results from the L1-norm and L2-norm are presented in Section 3.4.

3.2 Optimization by Simulated Annealing

Global optimization algorithms give a solution to non-linear problems. Based on the work of Metropolis et al. (1953), Kirkpatrick et al. (1983) proposed one of the beneficial global optimization methods, called Simulated Annealing (SA), which is analogous to the natural process of crystal annealing (Izumotani and Onozuka, 2013). Since the work of Kirkpatrick et al. (1983), Metropolis algorithm with annealing has been applied in a different applications of optimization problems (Sen and Stoffa, 2013). Nevertheless, SA has been generalized and implemented, successfully, in many geophysical and non-linear

rock physics inverse problem (Izumotani and Onozuka, 2013; Kirkpatrick et al., 1983). Searching for the best-fitting model parameters is one of the central goals of geophysical inversion (Sen and Stoffa, 2013). SA works by searching an optimal minimum value of a the cost function, shown in Eq. 3.4, where \mathbf{m} is the model vector. Following Sen and Stoffa (2013), and assuming that the starting model is \mathbf{m}^k with energy $E(\mathbf{m}^k)$, making a small perturbation to \mathbf{m}^k leads to a new model \mathbf{m}^{k+1} , which is given by

$$\mathbf{m}^{k+1} = \mathbf{m}^k + \Delta\mathbf{m}^k. \quad (3.5)$$

The new energy is now $E(\mathbf{m}^{k+1})$, assuming the difference in the energy between the to states is ΔE , the new state generated by Metropolis et al. (1953) is given by

$$\Delta E = E(\mathbf{m}^{k+1}) - E(\mathbf{m}^k). \quad (3.6)$$

Based on the value of ΔE , the decision of whether the new state is accepted or not can be made. The new state is accepted without any condition if $\Delta E = 0$, while if $\Delta E > 0$ it will be accepted with the probability

$$P = \exp\left(-\frac{\Delta E}{T}\right), \quad (3.7)$$

where T is the temperature. This accepting criteria is known as the Metropolis criterion. SA unlike the other greedy local optimization methods (e.g. iterative linear methods), has a finite probability of jumping out of local minima (Sen and Stoffa, 2013). One of the advantages of SA is that the cost function can be multi-variant, which is usually a function of a large number of variables, and does not require a good initial model (Jakobsen et al., 2021; Sen and Stoffa, 2013). The algorithm of simulated annealing is not only very simple but also its implementation is straightforward. However, to obtain the optimal result, and not settle for the second best, the coefficients, the minimum and the maximum of the search window, which are used in the equations of the cooling schedule, Eqs. 3.9, 3.11, and 3.12 must be carefully selected and examined (Izumotani and Onozuka, 2013). For this work, an algorithm called very fast simulated annealing (VFSA), proposed by Ingber (1989, 1993), will be adopted, a swift variant of the SA method. By taking advantage of the previously presented best-fitting search function, Eq. 3.4, VFSA, explained more detailed in Algorithms 2, has been implemented to find the global minima, which are the inverted model vector components.

In all variants of SA method, similar to the physical process of annealing, the goal is to minimize an energy function, which depends on a cooling scheme, they only differs in the way of the randomly perturbation of that temperature cooling scheme, Eq. 3.12 and the model parameters (Jakobsen et al., 2021). For the VFSA algorithm, employed in this

thesis, a temperature-dependent Cauchy distribution, Eq. 3.9, has been applied as the temperature cooling system. Starting with a random model at a high temperature. Then, at annealing step (iteration) k the model \mathbf{m} will be \mathbf{m}^k . Ingber's algorithm for VFSA is give by (Sen and Stoffa, 2013)

$$\mathbf{m}^{min} \leq \mathbf{m}^k \leq \mathbf{m}^{max}, \quad (3.8)$$

where \mathbf{m}^{min} and \mathbf{m}^{max} are the minimum and maximum values of the model parameter \mathbf{m} , respectively. Then, at iteration $k + 1$ the model parameter value will be perturbed, using the temperature-dependent Cauchy distribution given by (Jakobsen et al., 2021)

$$\mathbf{m}^{k+1} = \mathbf{m}^k + y(\mathbf{m}^{max} - \mathbf{m}^{min}), \quad (3.9)$$

where \mathbf{m}^{k+1} is the new candidate model at the $k + 1$ iteration, and can be perturbed, again, by

$$\mathbf{m}^{min} \leq \mathbf{m}^{k+1} \leq \mathbf{m}^{max}, \quad (3.10)$$

when the perturbation function y^k given by (Ingber, 1989)

$$y^k = sgn(u - 0.5)T^k \left[\left(1 + \frac{1}{T^k}\right)^{|2u-1|} - 1 \right], \quad (3.11)$$

where sgn is the signum function, u is a uniform random in the interval $[0, 1]$, and T^k is the temperature at the k th iteration and it is the cooling scheme by which the temperature is controlled and reduced. For the distribution used in this thesis, the global minimum can be statistically obtained using the following cooling scheme (Ingber, 1989):

$$T^k = T^{(0)}exp(-ac), \quad (3.12)$$

where $T^{(0)}$ is the initial temperature and the parameter c determines how fast the temperature is decreasing concerning the number of iterations, a , which is equal to the number of accepted models. Moreover, it is used to control the temperature scheme and help to tune the algorithm for specific problems (Jakobsen et al., 2021; Sen and Stoffa, 2013). VFSA provide quit good results, starting from a random place in the search area. Compiled with an exponential cooling, one can use the temperature-dependent Cauchy-distribution scheme for VFSA. Then, as the temperature cools, the unique Cauchy-like distribution condenses the perturbation amplitude. all these features give VFSA the ability to attain the global minimum very fast compared with the traditional SA (Jakobsen et al., 2021).

Algorithm 2: Pseudo code of the VFSA method for real data inversion, s , a , and S denotes sampling, the number of the accepted models, and the step been taken, respectively. This Pseudo code is mainly inspired by (Jakobsen et al., 2021).

```

m(i) = m(0)
T(i) = T(0)
s = a = 0
while T(i) > Tmin and s < smax do
  s = s + 1
  while u < Nu do
    Δm(i) = ModifiedCauchyDistribution(m(i), T(i))
    S = m(i) + Δm(i)
    if E(S) < E(m(i)) then
      m(i) = S
      a = a + 1
    else
      u = random(0, 1)
      if u < e-(E(S)-E(x))/T then
        m(i) = S
        a = a + 1
      end if
    end if
  end while
  Tk = T0e-c*a
end while
end while

```

3.3 Inversion of Synthetic Data

This section presents a theoretical inversion of the visco-elastic properties, namely P- and S-wave velocity and attenuation spectra of a complex porous media. The aim is to compare the results from the manually adjusted modelling, presented in Chapter 2, and results from VFSA. The dynamic version of the T-matrix approach to effective visco-elastic properties of complex porous media allow for the modelling of squirt flow in complex pore systems characterized by different relaxation times (Jakobsen et al., 2021). To perform the inversion, initially, a microstructural true model, which account for the model parameters based on the visco-elastic generalized Xu-White model, have been computed. Then, an

initial model of the model parameters, was adjusted, including the squirt flow time, to obtain the model's best match. The Matlab code is been modified to allow first for choosing whether to use the, theoretically predicted, synthetic data or, the observed, real data. As the VFSA Algorithm, which presented in Algorithm 2, being used can give the global minimum values are searched for, the models with different pore systems, introduced in Chapter 2, can be evaluated with respect to their ability to explain the behaviour of carbonate rocks. A secondary goal is to investigate the possibility of introducing an elegant microstructural visco-elastic model that can be successfully used for carbonate and complex porous media.

3.3.1 Inversion using Two Pore-type

In the coming inversion work, the upper and lower bound is as follows: The maximum and minimum perturbations of α_i and ϕ_i , in this study, are 50 percent. While for τ_i , the maximum perturbation is 10^{-6} and the minimum perturbation is 10^{-8} . The error bars is used to represent the probability distribution, with the median value in the center of it. This upper and lower bounds are always taken, in this work, if not otherwise stated.

Figure 3.1 shows the true model being used in the numerical experiments while the initial model is shown in Figure 3.2, the only different between this model and the reference model in the forward modelling, Chapter 2, is that this model is introduced with the error bars. For both the true, initial, and best-fitting model parameters been obtained see Table 3.1. A great deal has been obtained from the two pore-types model's inversion employing VFSA, as shown in Figure 3.3. However, a slight over-prediction of the S-wave attenuation can be noticed. Figure 3.4 shows the behaviour of the cost function, based on the cooling scheme, presented in Section 3.2, and the number of iterations that VFSA needed to find the best-fitting parameters. Typically VFSA techniques, after the first numerical experiment is been carried out, can be mentioned briefly as follows: Since the VFSA perturbs the model parameters. Thus, for obtaining the optimal result, using VFSA, it is quite worthy to perform the specific numerical experiment several times for each model. VFSA does not have high computational cost, by computational cost, it is meant that computational time or computational resources. The computational resources might be the random access memory (RAM) and/or the central processing unit (CPU). The time VFSA require is approximately 5 to 20 minutes, depending mostly on the L-norm being used. These features give the opportunity to, effortlessly, repeat the experiments. Ultimately, The lower and upper bound must be selected carefully.

Due to the non-linearity, the derived rock physics models are often uncertain (?). Thus, in this section the effects of noise are presented, to estimate how our derived models

Table 3.1: Model parameters of the true model, initial model, and the inverted model based on the inversion of the model with tow different pore-types.

Microstructures	True model	Initial model	Inverted model
α_1	0.1500	0.2100	0.1496
α_2	0.0500	0.0260	0.0542
ϕ_2	0.00556	0.00220	0.00540
$\tau_1[s]$	1×10^{-7}	1.1×10^{-8}	1.69×10^{-7}
$\tau_2[s]$	1×10^{-7}	0.7×10^{-6}	1.68×10^{-7}

been affected by the noise. The noise levels here, are considered to be consistent with the uncertainties of real data measurements, presented in Section 1.2.2. In this synthetic inversion, the uncertainty of the P-wave attenuations was reduced from ± 3 to ± 2 , since it will not have a big effect in the synthetic computations. Figure 3.5 shows the result for the inversion of model with noise. The model is of two sets of pores, using the same initial model, used in the noiseless model, shown in Figure 3.2. The best-fitting parameters and the other model parameters being used are in Table 3.2. From the results one can notice that noise effect is relatively little.

Table 3.2: Model parameters for both the true model, the initial model, and the inverted model of two pore-types with noise levels, consistent with the uncertainties of the real data measurement.

Microstructures	True model	Initial model	Inverted model
α_1	0.1500	0.2100	0.1488
α_2	0.0500	0.0260	0.0488
ϕ_2	0.00556	0.00220	0.00551
$\tau_1[s]$	1×10^{-7}	1.1×10^{-8}	2.35×10^{-7}
$\tau_2[s]$	1×10^{-7}	0.7×10^{-6}	0.76×10^{-7}

Model Error evaluation

Computer measurement and modelling work is often done in simplified way, because of the limitations may occur or come to pass, while the models in real life is more complicated. An inversion of three sets of pores using model with two sets of pores is performed, to

estimate the model error (ME). In inversion, one can estimate the model error, based on numerical experiments, which primarily meant to explain the challenging that scientists phase as a result of inversion based on simplified model. In this task I inverted a model of three pore-types using model with only two types of pores, 3.1. The inverted model parameters are viewed in Table 3.3. The inversion result, as shown in Table 3.3 and Figure 3.9, appears to be unreliable and away from the true model as shown in Figure 3.7.

Table 3.3: Model parameters for, the true model, the initial model, and the inverted model, for data of three pore-types, inverted with model of two sets of pores.

Microstructures	True model	Initial model	Inverted Model
α_1	0.1500	0.2100	0.1307
α_2	0.0500	0.0260	0.0282
α_3	0.0010	–	–
ϕ_2	0.0250	0.0022	0.0081
ϕ_3	0.0001	–	–
$\tau_1[s]$	1.00×10^{-7}	1.10×10^{-8}	1.34×10^{-7}
$\tau_2[s]$	1.00×10^{-7}	0.70×10^{-6}	1.78×10^{-7}
$\tau_3[s]$	1.00×10^{-7}	–	–

3.3.2 Inversion using Three Pore-type

As the model error has been introduced in the previous discussion, further an inversion of the model with three pore-types, is presented here. This time using the correct true model in Figure 3.7. By the correct true model here, it meant the true model with an equivalent pore-types. the initial model is shown in Figure 3.8. Figure 3.11 illustrates the inverted model, the differences are evident between the two inversions, namely the inversion of three sets of pores inverted by only two sets of pores and the other one that is inverted by the data with the equivalent pore-types. The model parameters are in Table 3.4 below. Again a very good much has been obtained, however, VFSA inversion over-predict the real data of the attenuation spectra a bit.

Then, an inversion for three pore-types with some uncertainties, is performed. The model, in this task, consist of three sets of pores, with the same noise levels provided in Section 1.2.2, is performed. An estimation to uncertainties effects is been provided in Figure 3.13. The model parameters are in table 3.5 below.

3.4 Inversion of Real Data

3.4.1 Inversion using Two Different Pore-Type

The same methodology in the synthetic data inversion is followed here, in the real data inversion. First, an inversion with two sets of pores is performed, using Algorithm 2.

Table 3.4: Model parameters for, true model, initial model, and inverted model for the model with three pore types.

Microstructures	True model	Initial model	Inverted Model
α_1	0.1500	0.2200	0.1499
α_2	0.0500	0.0260	0.0494
α_3	0.0010	0.0015	0.0014
ϕ_2	0.02500	0.01220	0.02480
ϕ_3	0.000100	0.00140	0.00014
$\tau_1[s]$	1×10^{-7}	2.01×10^{-7}	1.07×10^{-7}
$\tau_2[s]$	1×10^{-7}	3.01×10^{-7}	1.07×10^{-7}
$\tau_3[s]$	1×10^{-7}	4.01×10^{-7}	1.07×10^{-7}

Table 3.5: Model parameters of true model, initial model, and inverted model for the model with three pore types after adding some noises, consistent with uncertainties of the real data measurements.

Microstructures	True model	Initial model	Inverted Model
α_1	0.1500	0.2200	0.1463
α_2	0.0500	0.0260	0.0549
α_3	0.0010	0.0015	0.0009
ϕ_2	0.0250	0.0122	0.0239
ϕ_3	0.0001	0.0014	0.0001
$\tau_1[s]$	1×10^{-7}	2.01×10^{-7}	1.03×10^{-7}
$\tau_2[s]$	1×10^{-7}	3.01×10^{-7}	1.03×10^{-7}
$\tau_3[s]$	1×10^{-7}	4.01×10^{-7}	1.03×10^{-7}

The numerical experiments give, as expected, a weak match in general, see Figure 3.15. However, one can notice that it gives a good match at the ultrasonic frequency, for the S-wave attenuation. The model parameters are organized in Table 3.6. Figure 3.16 shows the behaviour of the objective function and of the temperature cooling. To recover for the low value of the S-wave attenuation, an adjustment of the initial model parameters, and on one of the calcite perturbations parameters, namely on Xs has been made. The results now seem to be better and the S-wave attenuation (at the ultrasonic frequency) got raised

to the expected position, as shown in Figure 3.17. Figure 3.18 shows the behaviour of the objective function and of the temperature cooling scheme.

Table 3.6: Model parameters of the initial model and the inverted model, based on the inverted model of the real data. The model is of two pore-types.

Microstructures	Initial model	Inverted model
α_1	0.15000	0.19600
α_2	0.0500	0.07100
ϕ_2	0.00556	0.00008
X_p	1	1.36
X_s	1	1.11
$\tau_1[s]$	1×10^{-7}	6.72×10^{-8}
$\tau_2[s]$	1×10^{-7}	1.31×10^{-7}

Table 3.7: Model parameters of the initial model and the inverted model based on the inverted model of the real data. The model is of three pore-types.

Microstructures	Initial model	Inverted model
α_1	0.0750	0.1120
α_2	0.0350	0.0523
ϕ_2	0.0350	0.0241
X_p	1.000	1.157
X_s	1.000	1.106
$\tau_1[s]$	1×10^{-7}	8.70×10^{-8}
$\tau_2[s]$	1×10^{-7}	1.01×10^{-7}

Several experiment have carried out, for the model of two pore-types, using real data. After all, the results obtained by the inversion are somewhat far from the observed data, and need a lot of improvement.

3.4.2 Inversion using Three Different Pore-Type

An inversion for a model with three pore-types, shown in Figure 3.19) gives a better much specially at the sonic frequency (more noticeable on the attenuation spectra), however, at the ultrasonic frequency the attenuations need to be increased. The addition of the

third sets of pores gives a bit of improvement, but still it is not that satisfactory. To recover the low value of the P-wave and S-wave attenuation at the ultrasonic frequency, an adjustments of the initial model parameters and the calcite perturbations parameters have been made. There are some improvement on the attenuations spectra at the ultrasonic frequency, see Figure 3.20. Figure 3.21 shows the behaviour of the objective function and of the temperature cooling scheme. Again, several experiment have been carried out, using different upper and lower pounds. However, it seems still quite tricky to obtain a good balance on the model parameters, even when a model with three different pore-types is been used. Contrary to the conventional modelling of sandstone rocks and the media with less complexity, it is of important to have some innovated tricks when dealing with carbonates. By employing, among other things, the analyses and modelling discussion, Chapter 2 and discussions from Chapters 1, such as how the fluid-pressure relaxation can affect the acoustic behaviour of a complex media. Some cracks with low aspect ratios are already forming some shapes of channels to connect the more toroidal pores together, however adding more compliant would give a closer to the real complex media, featured by more complexity required by nature (Jakobsen et al., 2003a). The compliant pores seems to have a big role on the visco-elastic properties of the rock physic model, more specifically on the attenuation spectra; their edges opens into the more round shaped stiff pore and they form a disk-shaped gap between the neighbouring grains (Gurevich et al., 2010).

3.4.3 Inversion using Four Different Pore-Type

From the result and discussion in the previous Section, it seems very necessary for obtaining the optimum match, a model with four different sets of pores has been introduced, Figure 1.5 (c), by adding a compliant sets that is increase the interconnections of the system and gives the system a texture that close to the complex porous media, namely limestone and related porous media. In the inversion with four different pore-tyes, a new inversion alternatives has been investigated. This is to curry out an inversion of only attenuation. Then, the model with four different pore types has been inverted for only attenuation, as shown in Figure 3.22 the inversion for only attenuation cause give some miss much, it is clear that the velocity is been effected more. Trying to get a better much on the velocity can be on the cost of worse much on the attenuation.

Next, is to compare between results from L1-norm and results from L2-norm. First, an inversion using L1-norm in the case of model with four pore-types, has been performed, the result is shown in Figure 3.24. The Vs attenuation gives a good match at the ultrasonic frequency, but, it under-predicts the observed data a bit at sonic frequency. However, the Vp attenuation has shown a big miss-match at the ultra sonic frequency, while it

under-predicts the observed data highly at sonic frequency. Ultimately, a quite good much have been obtained by inversion of both velocity and attenuation, using L2-norm, see Figure 3.26. However, VFSA slightly over-predict the measured P-wave velocity at the ultrasonic frequency and the S-wave velocity at the sonic frequency. The best-fitting model parameters are in table 3.10. Figure 3.27 shows the behaviour of the objective function and of the temperature cooling.

Table 3.8: Best-fitting model parameters for the inverted model in comparison with initial model for the model with three different pore types.

Microstructures	Initial model	Inverted Model
α_1	0.1500	0.2130
α_2	0.0500	0.0710
α_3	0.0010	0.0003
ϕ_2	0.00250	0.00009
ϕ_3	0.00250	0.00001
Xp	1.00	1.32
Xs	1.00	1.01
$\tau_1[s]$	1×10^{-8}	9.57×10^{-7}
$\tau_2[s]$	1×10^{-8}	5.16×10^{-7}
$\tau_3[s]$	1×10^{-7}	1.3×10^{-7}

Table 3.9: Best-fitting model parameters for the inverted model in comparison with the initial model for the model with three different pore types.

Microstructures	Initial model	Inverted Model
α_1	0.09500	0.11230
α_2	0.04500	0.05390
α_3	0.00045	0.00037
ϕ_2	0.022500	0.000900
ϕ_3	0.000225	0.000014
Xp	1.000	1.460
Xs	0.900	0.981
$\tau_1[s]$	1×10^{-8}	8.57×10^{-7}
$\tau_2[s]$	1×10^{-8}	5.26×10^{-7}
$\tau_3[s]$	1×10^{-7}	1×10^{-7}

Table 3.10: Model parameters for the initial model, and inverted model for the model with four different pore types.

Microstructures	Initial model	Inverted Model
α_1	0.1500	0.2160
α_2	0.0500	0.0252
α_3	0.0010	0.0014
α_4	0.0010	0.0013
ϕ_2	0.0250	0.0050
ϕ_3	0.00050	0.00008
ϕ_4	0.00050	0.00099
Xp	1.00	1.19
Xs	1.00	0.89
$\tau_1[s]$	1×10^{-8}	5.63×10^{-8}
$\tau_2[s]$	1×10^{-8}	6.14×10^{-8}
$\tau_3[s]$	1×10^{-7}	9.57×10^{-8}
$\tau_4[s]$	1×10^{-7}	1.4×10^{-8}

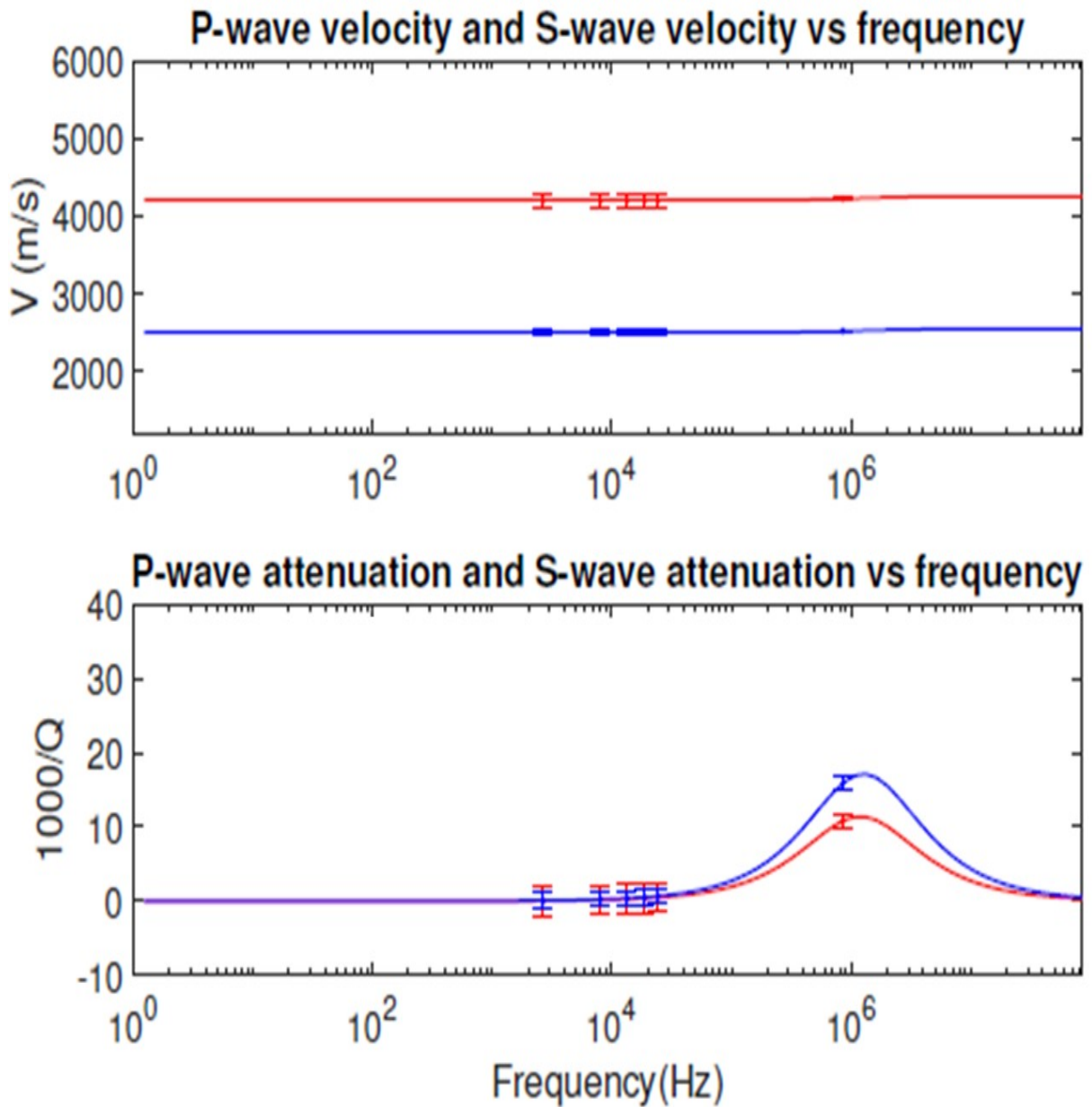


Figure 3.1: The true model of two pore-types with, and without noise. Synthetic data are plotted as dots in the middle of the errorbars, red (p-wave), blue (S-wave). The errorbars, red (p-wave), blue (S-wave) represent the probability distribution, with the median data value in the middle of it. Using the model parameters in Table 3.1.

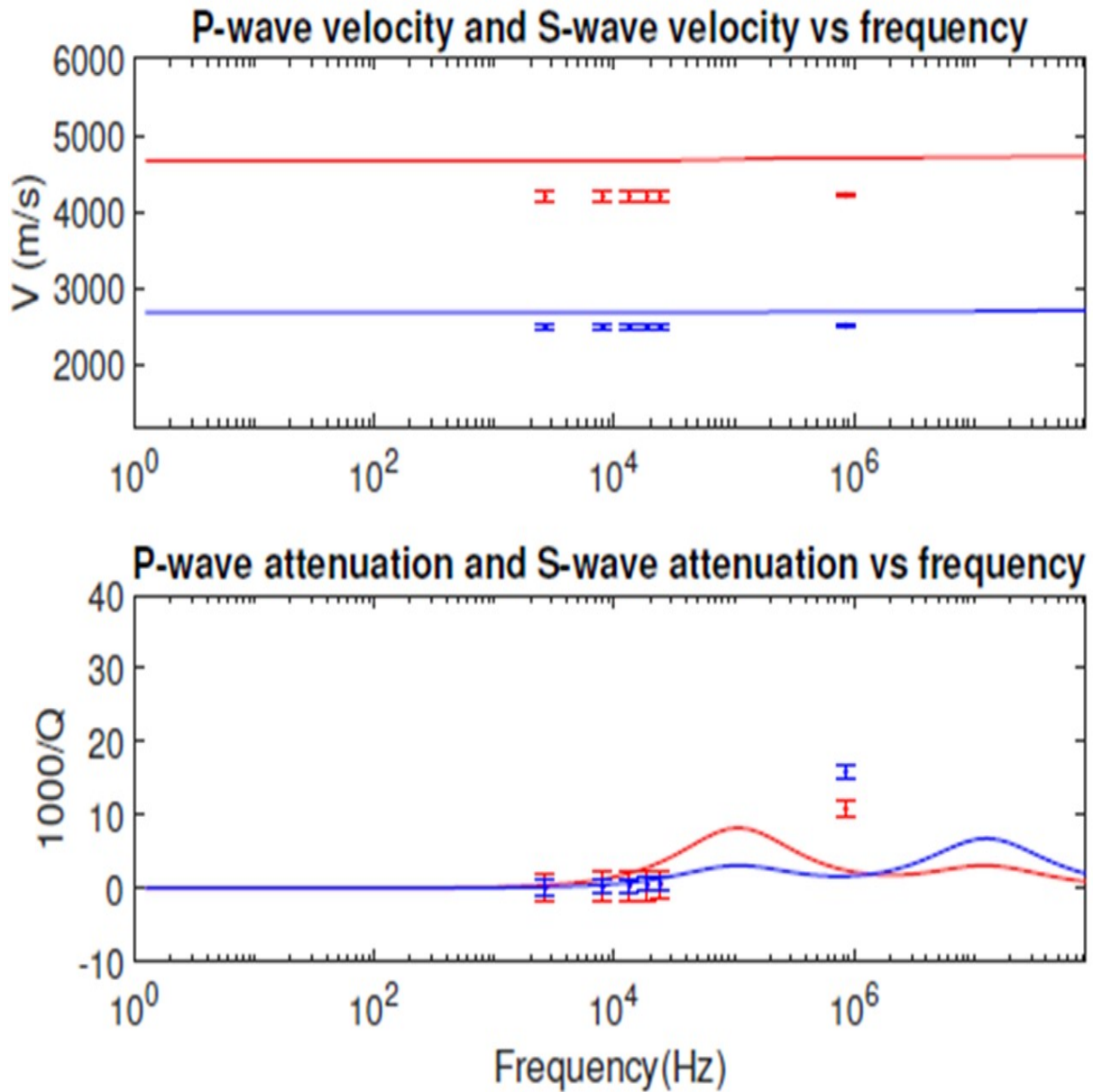


Figure 3.2: Illustration of the initial model used in the data inversion by VFSA. Synthetic data are plotted as dots in the middle of the error bars, red (p-wave), blue (S-wave). The errorbars, red (p-wave), blue (S-wave) represent the probability distribution, with the median data value in the middle of it. For the model parameters see Table 3.1.

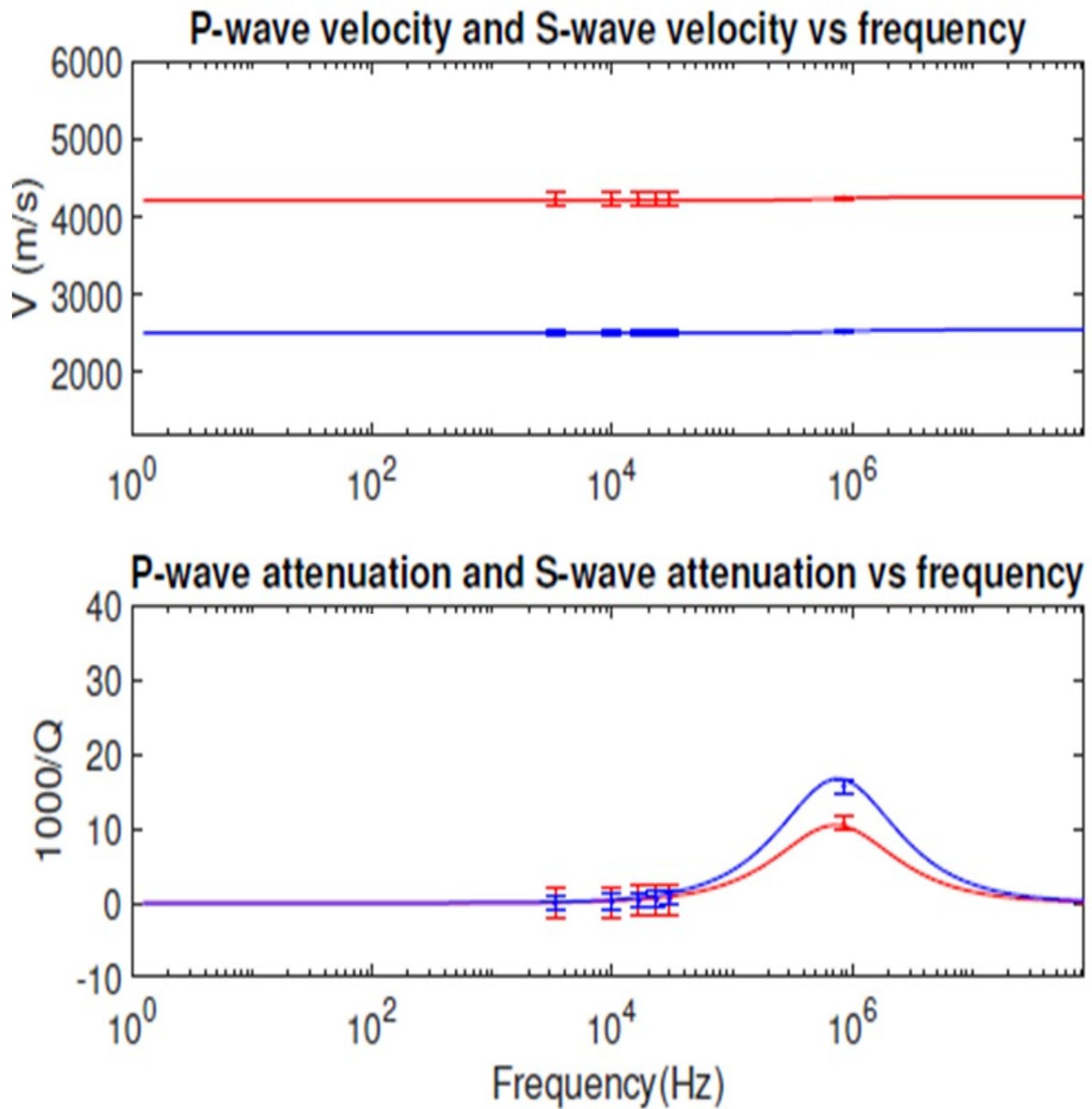


Figure 3.3: The inverted model by VFSA, for model of two pore types. Synthetic data are plotted as dots in the middle of the errorbars, red (p-wave), blue (S-wave). The errorbars, red (p-wave), blue (S-wave) represent the probability distribution, with the median data value in the middle of it. The true model is in Figure 3.1, and the initial model is in Figure 3.2, for the model parameters see Table 3.1.

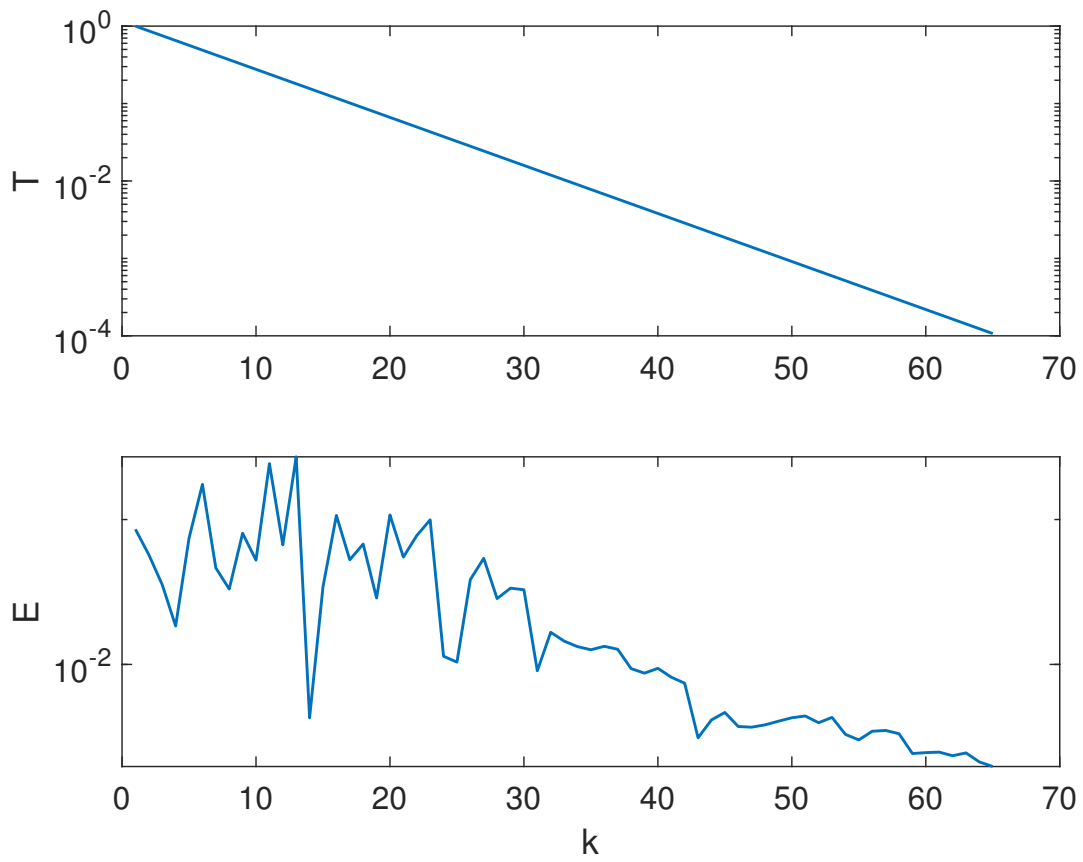


Figure 3.4: Illustration of the number of iterations and the behaviour of the objective function, and cooling process (temperature curve) for the model in Figure 3.3 above.

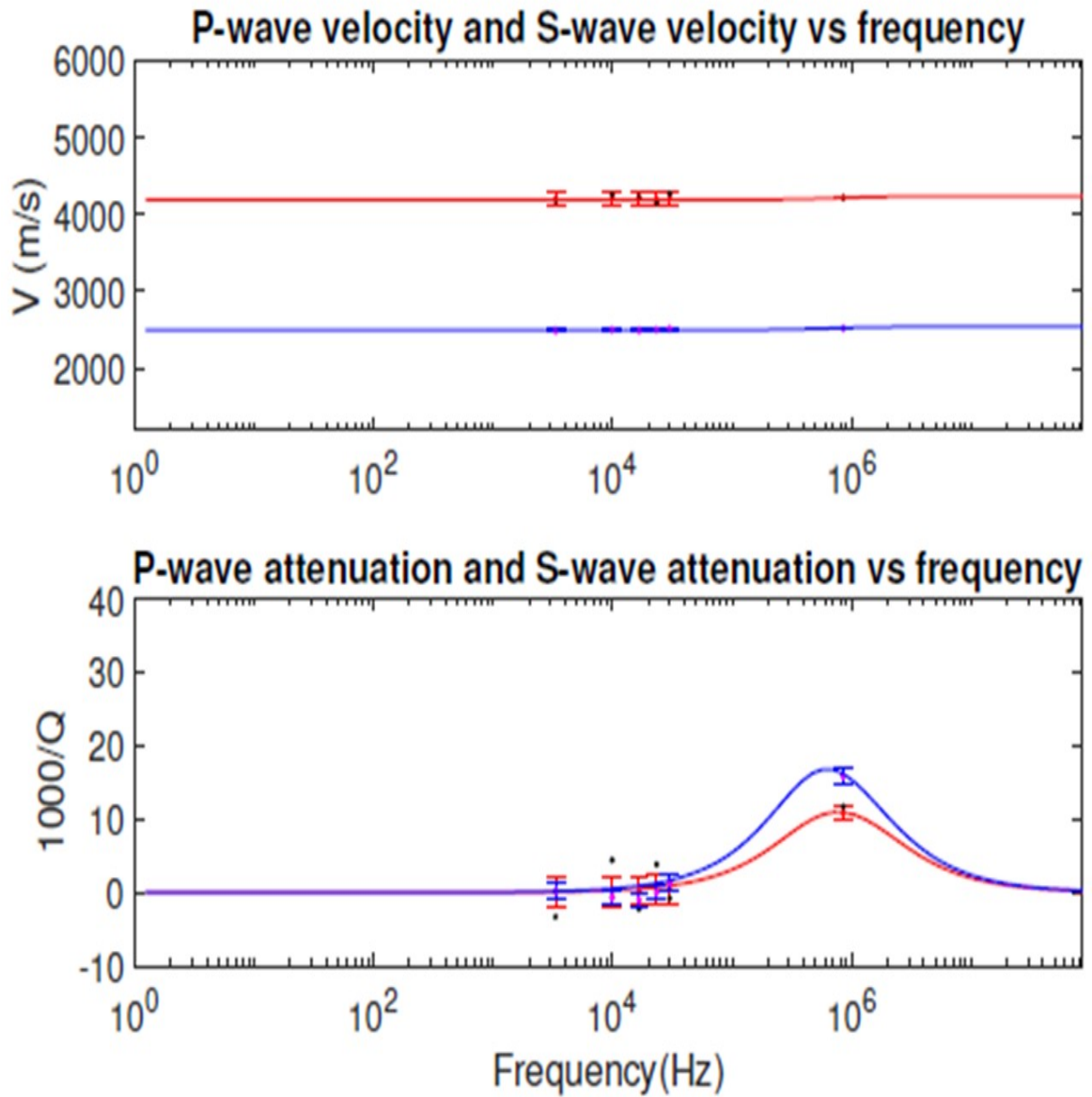


Figure 3.5: Inverted of the model with noise, for the same model in Figure 3.3. Synthetic data are plotted as dots in the middle of the error bars, red (p-wave), blue (S-wave). The errorbars, red (p-wave), blue (S-wave) represent the probability distribution, with the middle data value (data without noise) in the center of it. Here, noise realization is shown by the black and magenta dots for the P-wave and S-wave spectra, respectively, for the model parameters see Table 3.2.

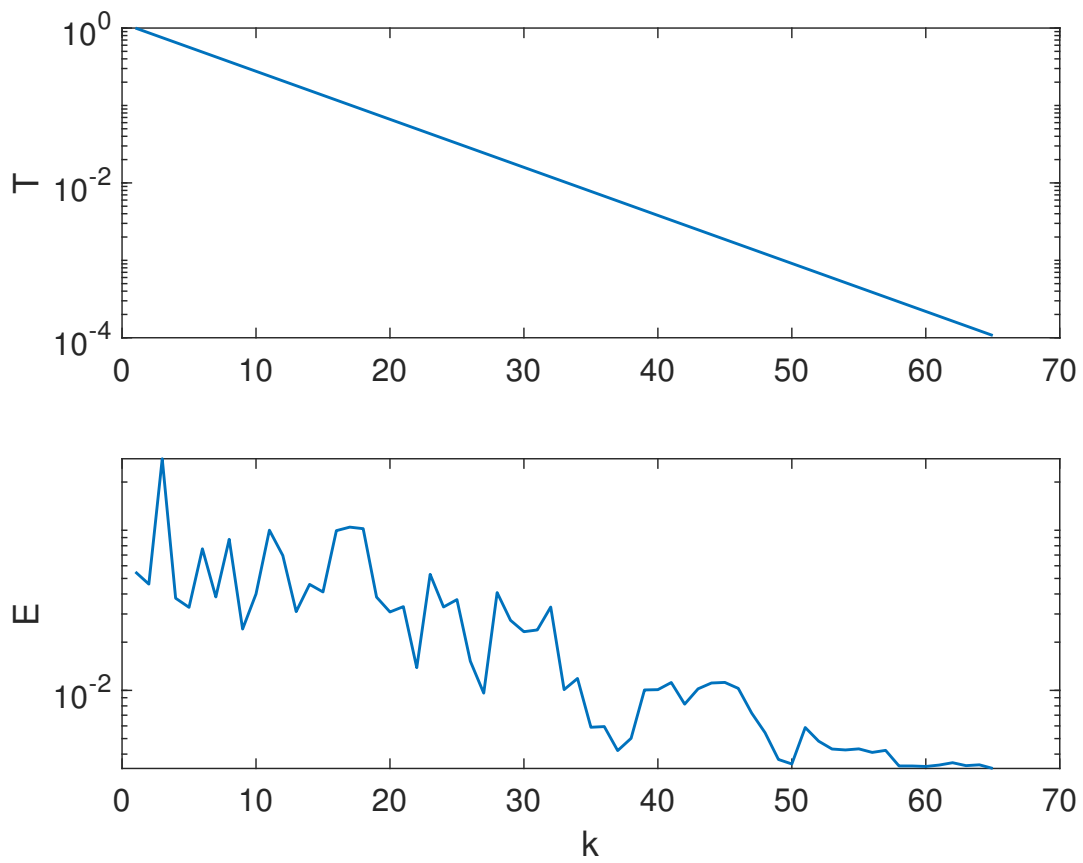


Figure 3.6: Illustration of the number of iterations and the behaviour of the objective function, and cooling process (temperature curve) for the model in Figure 3.5 above.

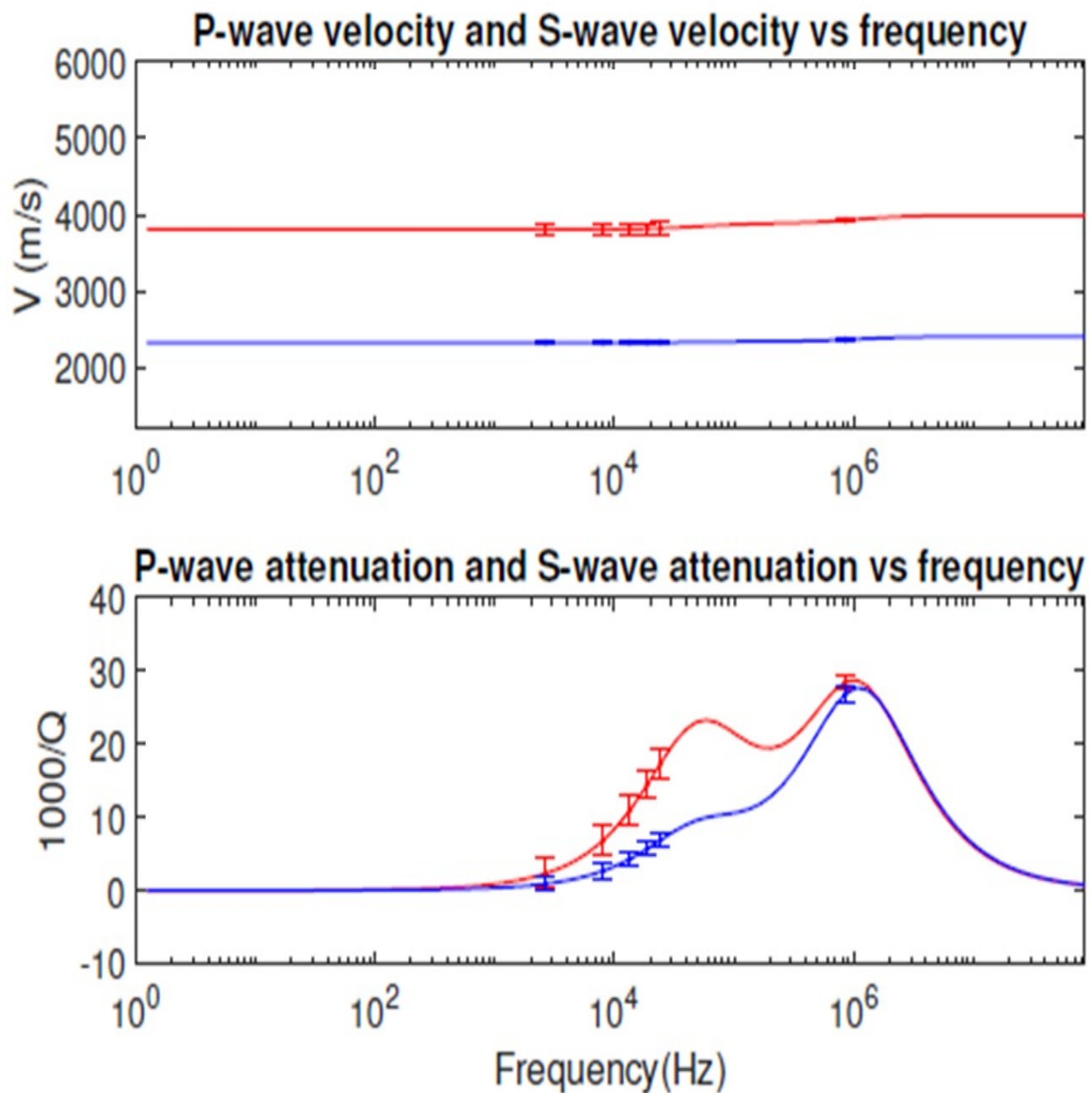


Figure 3.7: True model, the model is with three sets of pores. The errorbars, red (p-wave), blue (S-wave) represent the probability distribution, with the middle data value in the middle of it. Synthetic data are plotted as dots in the middle of the errorbars, red (p-wave), blue (S-wave). The model parameters are in Table 3.3.

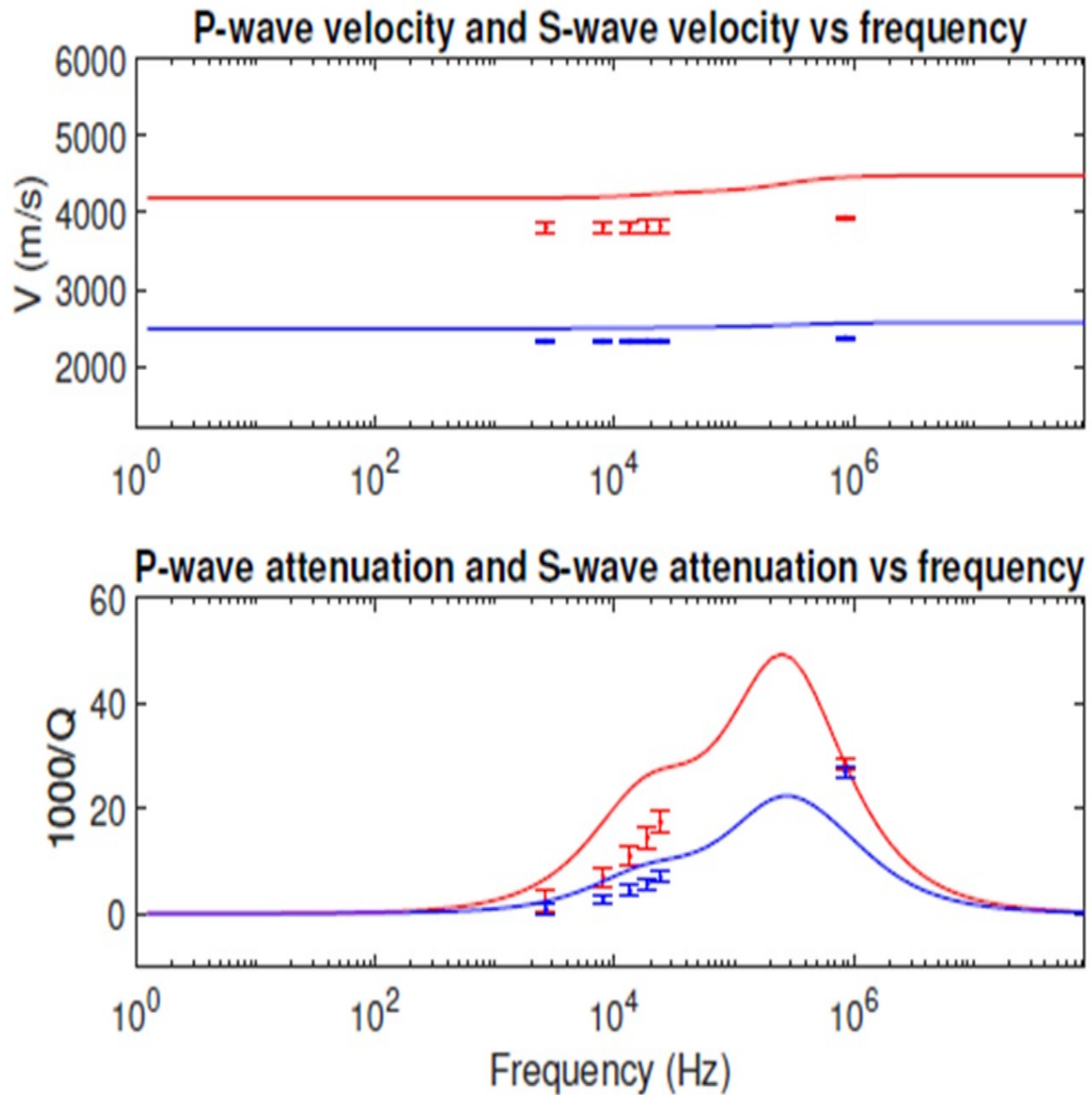


Figure 3.8: The initial model for the model with three sets of pores. Synthetic data are plotted as dots in the middle of the errorbars, red (p-wave), blue (S-wave). A comparison between synthetic data (data with errorbars) and theoretical predictions of the velocity and attenuation spectra of a rock model with three sets of pores. Model parameters are in Table 3.3.

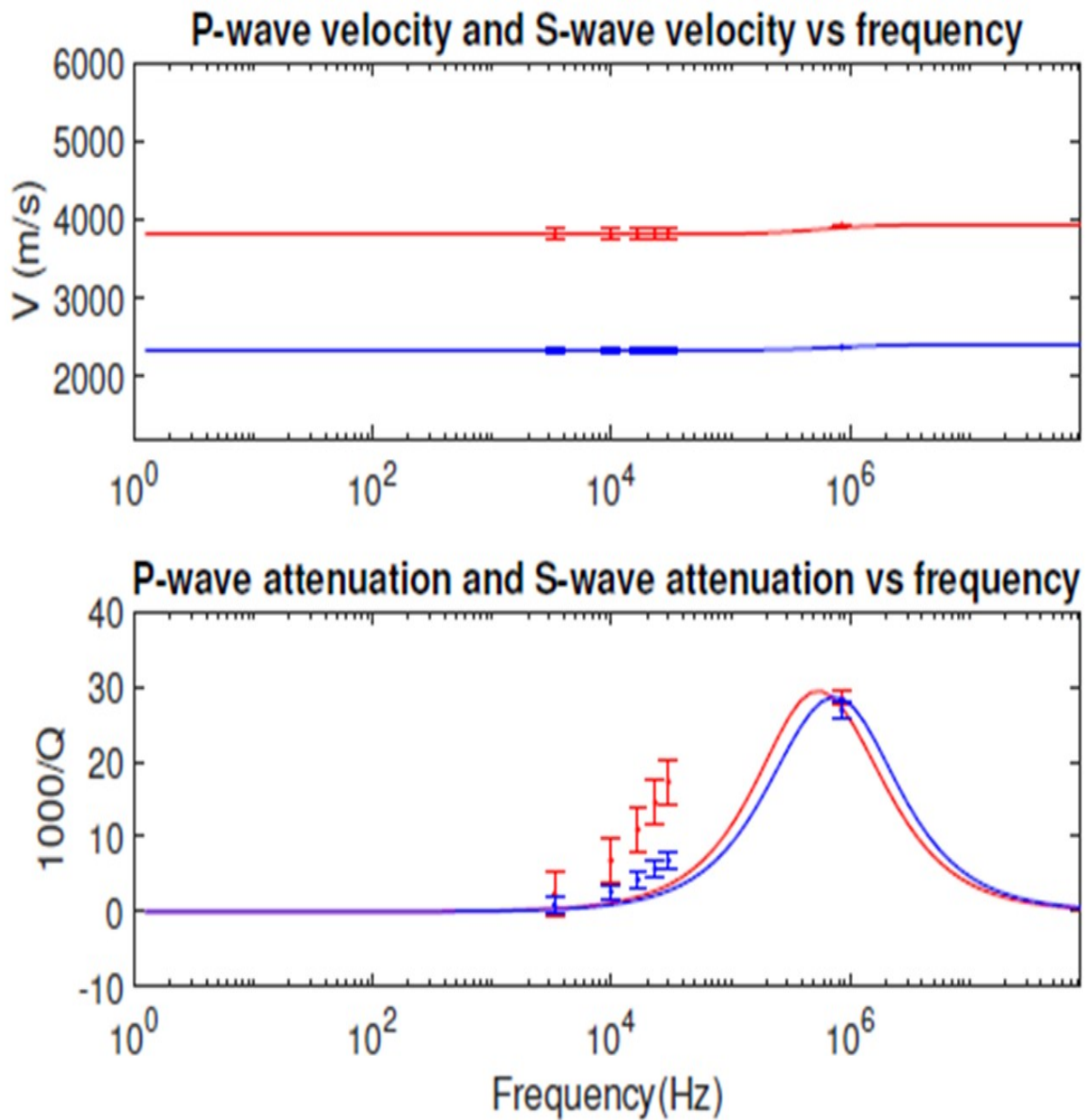


Figure 3.9: The model error estimation, when the three pore-types model inverted by model with two-pores. Synthetic data are plotted as dots in the middle of the errorbars, red (p-wave), blue (S-wave). The errorbars, red (p-wave), blue (S-wave) represent the probability distribution, with the median data value in the middle of it. The true model and initial model are in Figure 3.7, and Figure 3.8, respectively. The model parameters are in Table 3.3.

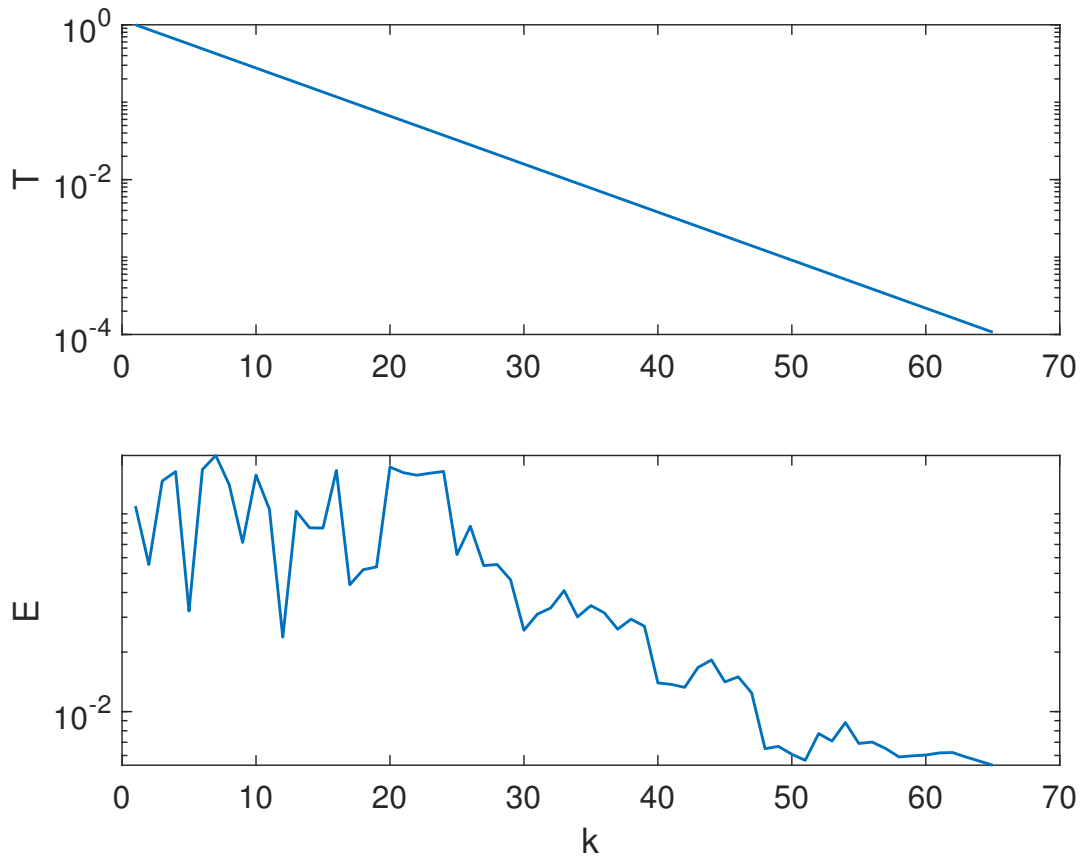


Figure 3.10: Illustration of the number of iterations needed by VFSA, the behaviour of the objective function, and cooling process (temperature curve)for the model in Figure 3.9 above.

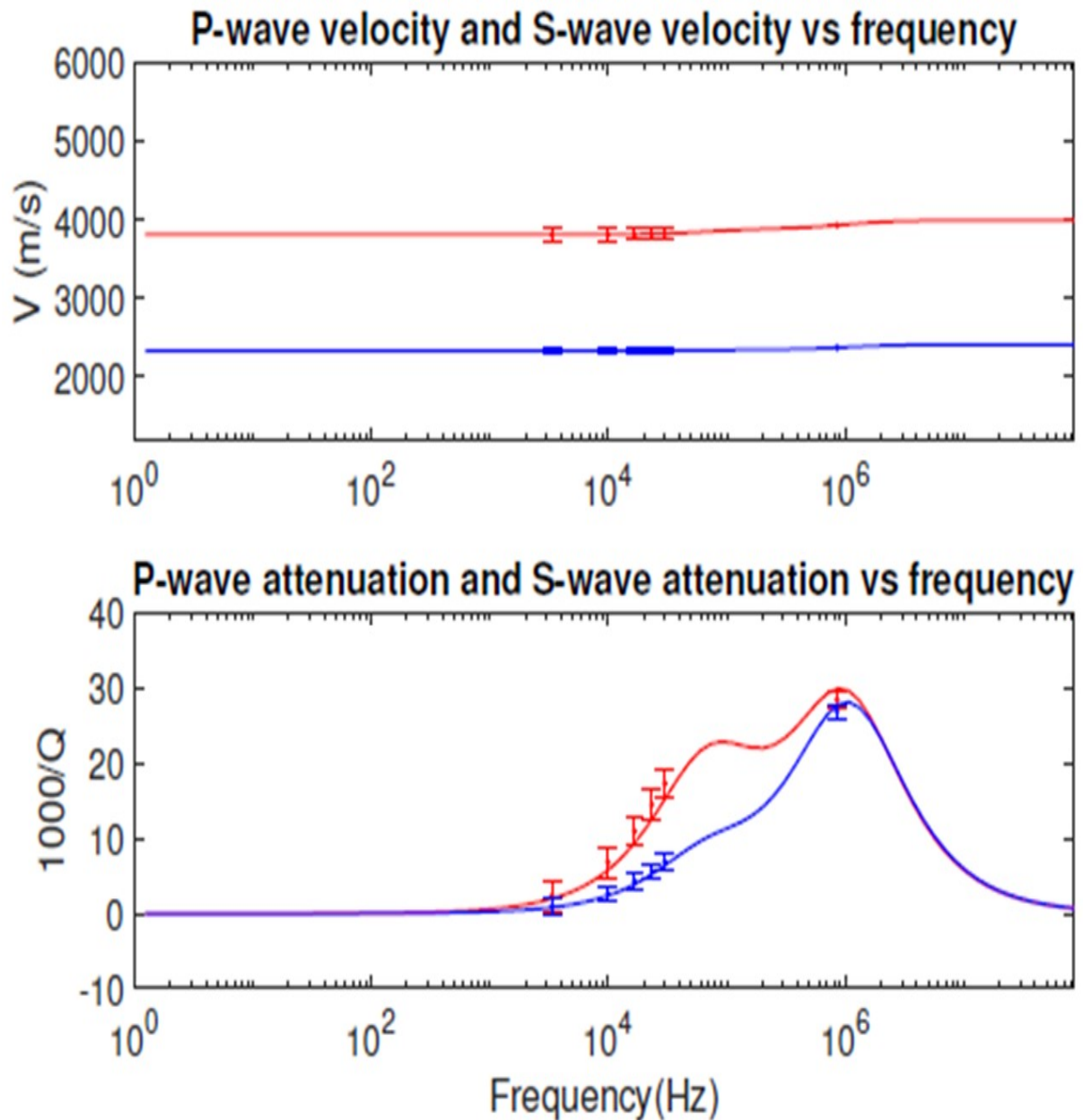


Figure 3.11: The inverted model, for model of three pore types. Using the same true model in figure 3.9. Synthetic data are plotted as dots in the middle of the errorbars, red (p-wave), blue (S-wave). The errorbars, red (p-wave), blue (S-wave) represent the probability distribution, with the median data value in the middle of it. The theoretical predictions of both models are based on a microstructural visco-elastic model of communicating cavities with different pore shapes and scales, using the model parameters in Table 3.4.

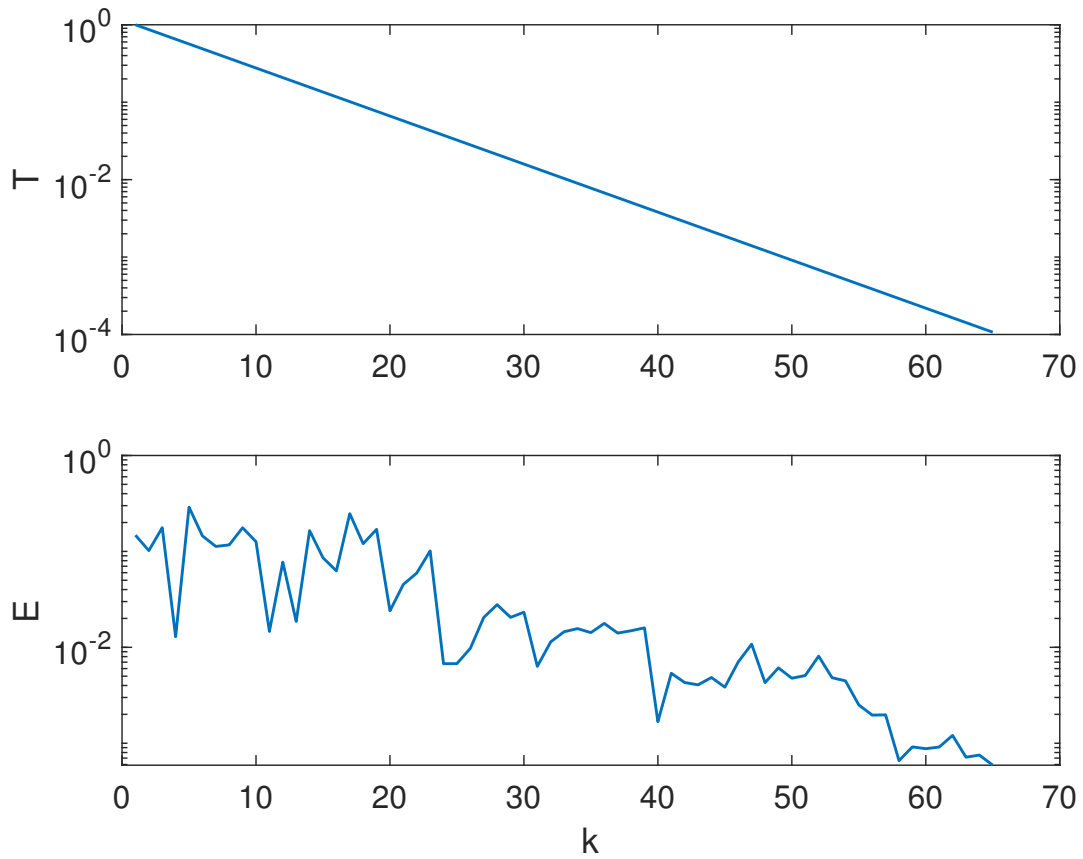


Figure 3.12: Illustration of the number of iterations needed by VFSA, the behaviour of the objective function, and cooling process (temperature curve) for the model in Figure 3.11 above.

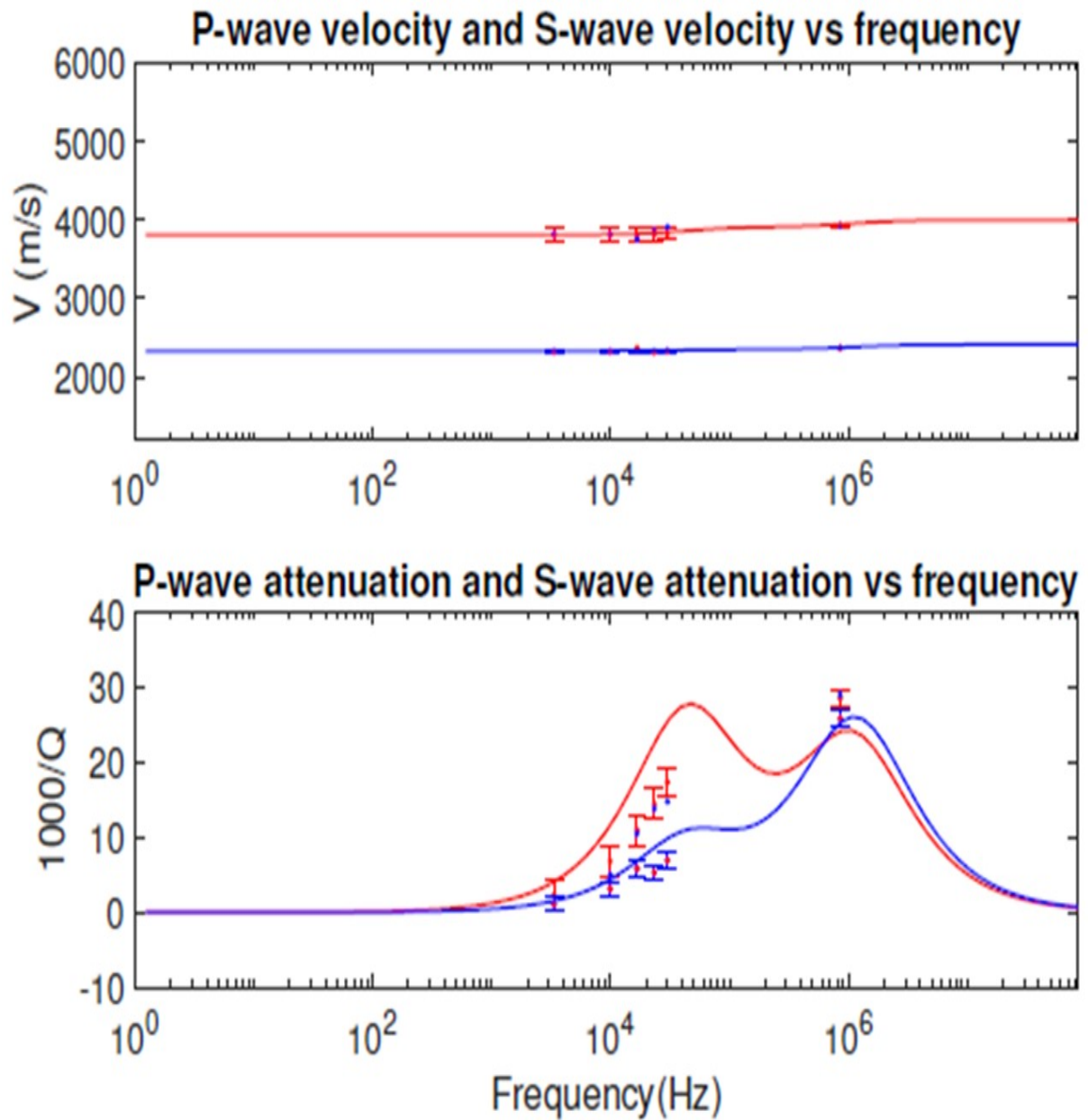


Figure 3.13: The inverted model with noise added, for the three sets of pores inverted with three sets of pores. Synthetic data are plotted as dots in the middle of the errorbars, red (p-wave), blue (S-wave). The errorbars, red (p-wave), blue (S-wave) represent the probability distribution, with the median data value (data without noise) in the middle of it. Noise realization is shown by the blue and red dots for the P-wave and S-wave spectra, respectively, for the model parameters see Table 3.5.

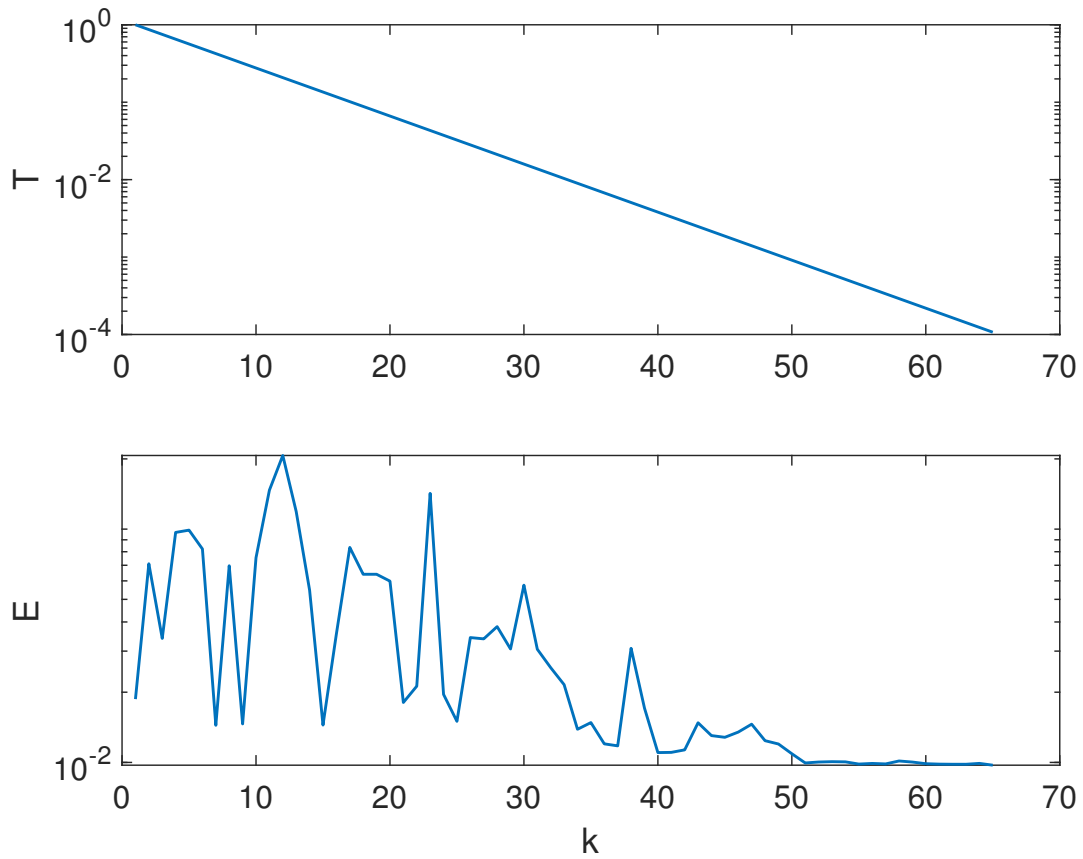


Figure 3.14: Illustration of the number of iterations needed by VFSA, the behaviour of the objective function, and cooling process (temperature curve) for the model in Figure 3.13 above.

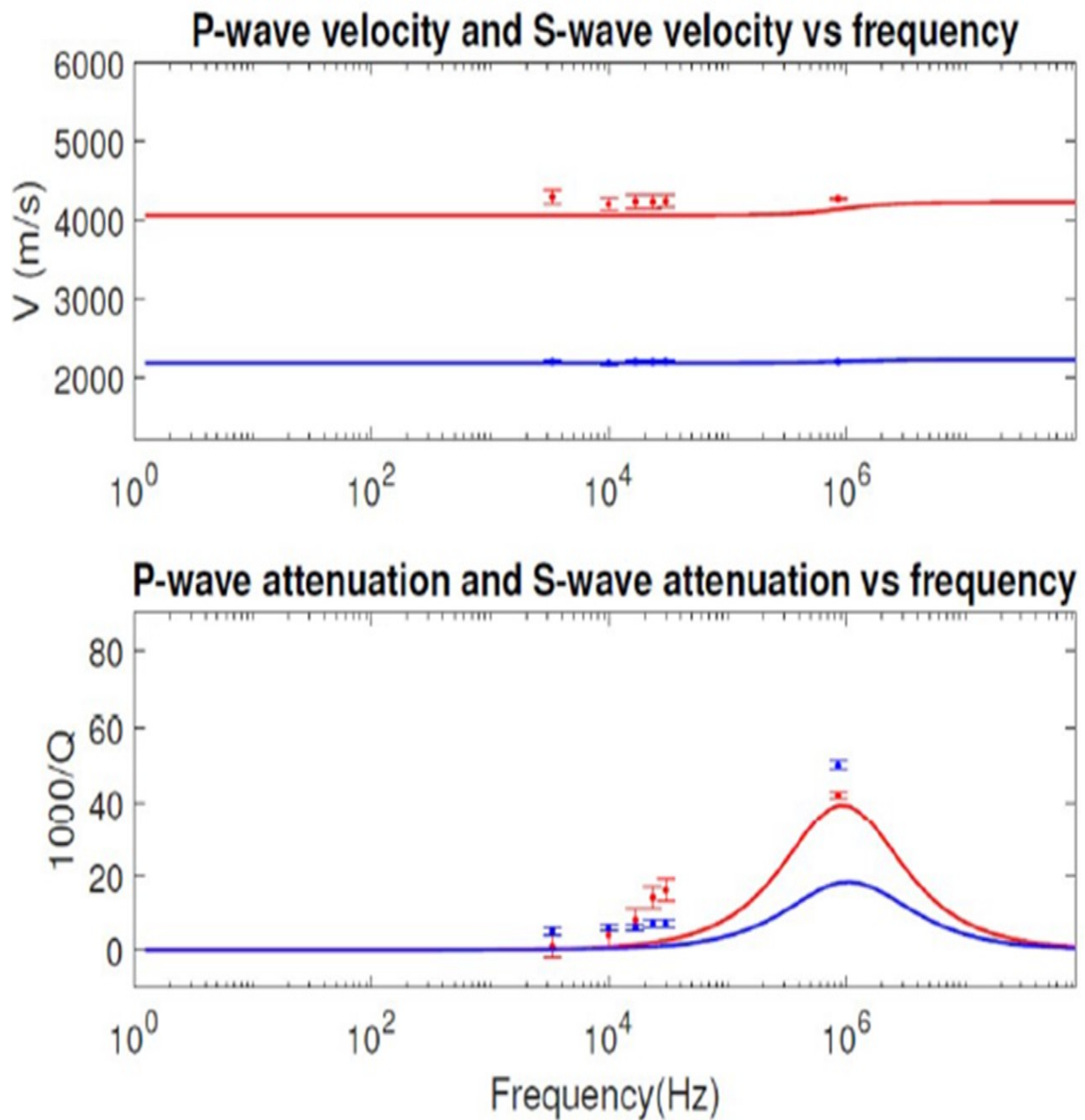


Figure 3.15: The real data inversion for the model of two sets of pores. Synthetic data are plotted as dots in the middle of the errorbars, red (p-wave), blue (S-wave). The errorbars, red (p-wave), blue (S-wave) represent the probability distribution, with the median data value in the middle of it. for the model parameters see Table 3.6.

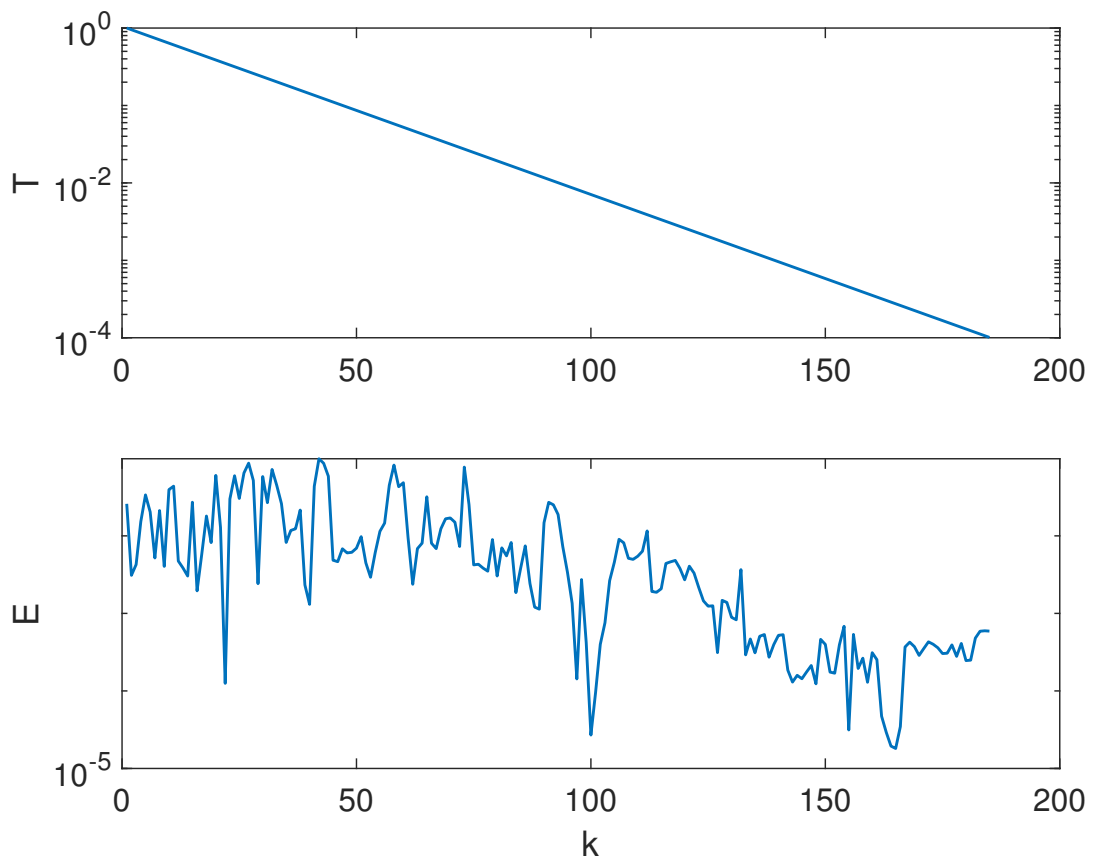


Figure 3.16: The number of iterations needed by VFSA, the behaviour of the cost function, and cooling process (temperature curve) for the model in Figure 3.15 above.

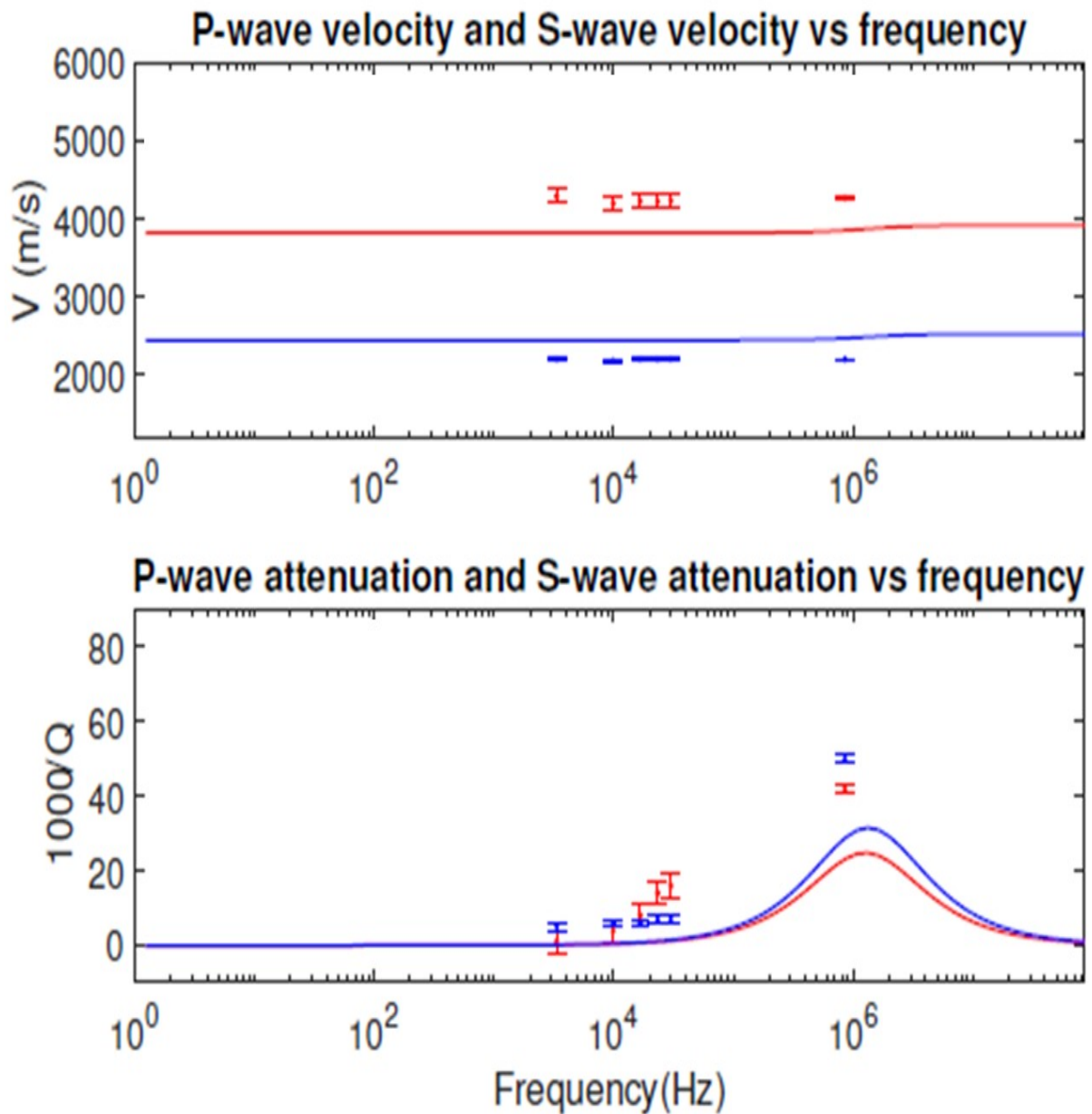


Figure 3.17: The real data inversion for the model of two sets of pores. Synthetic data are plotted as dots in the middle of the errorbars, red (p-wave), blue (S-wave). The errorbars, red (p-wave), blue (S-wave) represent the probability distribution, with the median data value in the middle of it. For the initial model and the best-fitting parameters been obtained see Table 3.7.

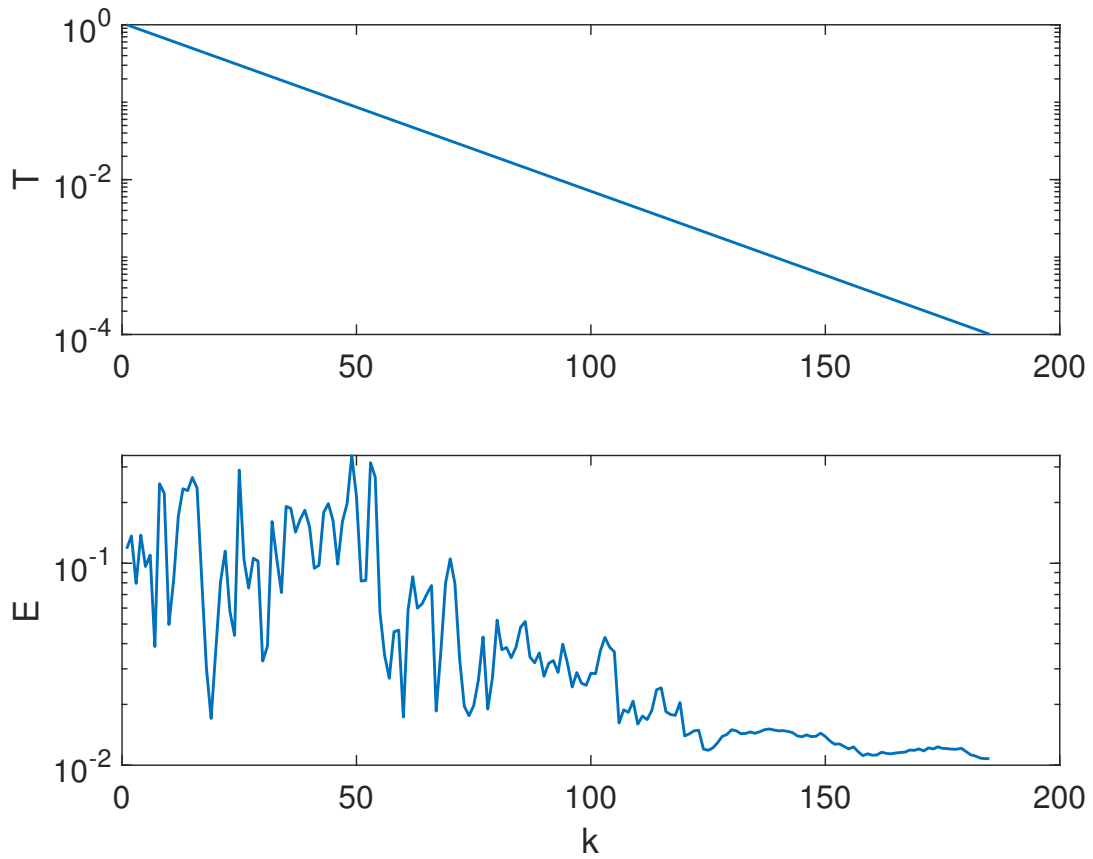


Figure 3.18: Illustration of the number of iterations needed by VFSA, the behaviour of the objective function, and cooling process (temperature curve) for the model in Figure 3.17 above.

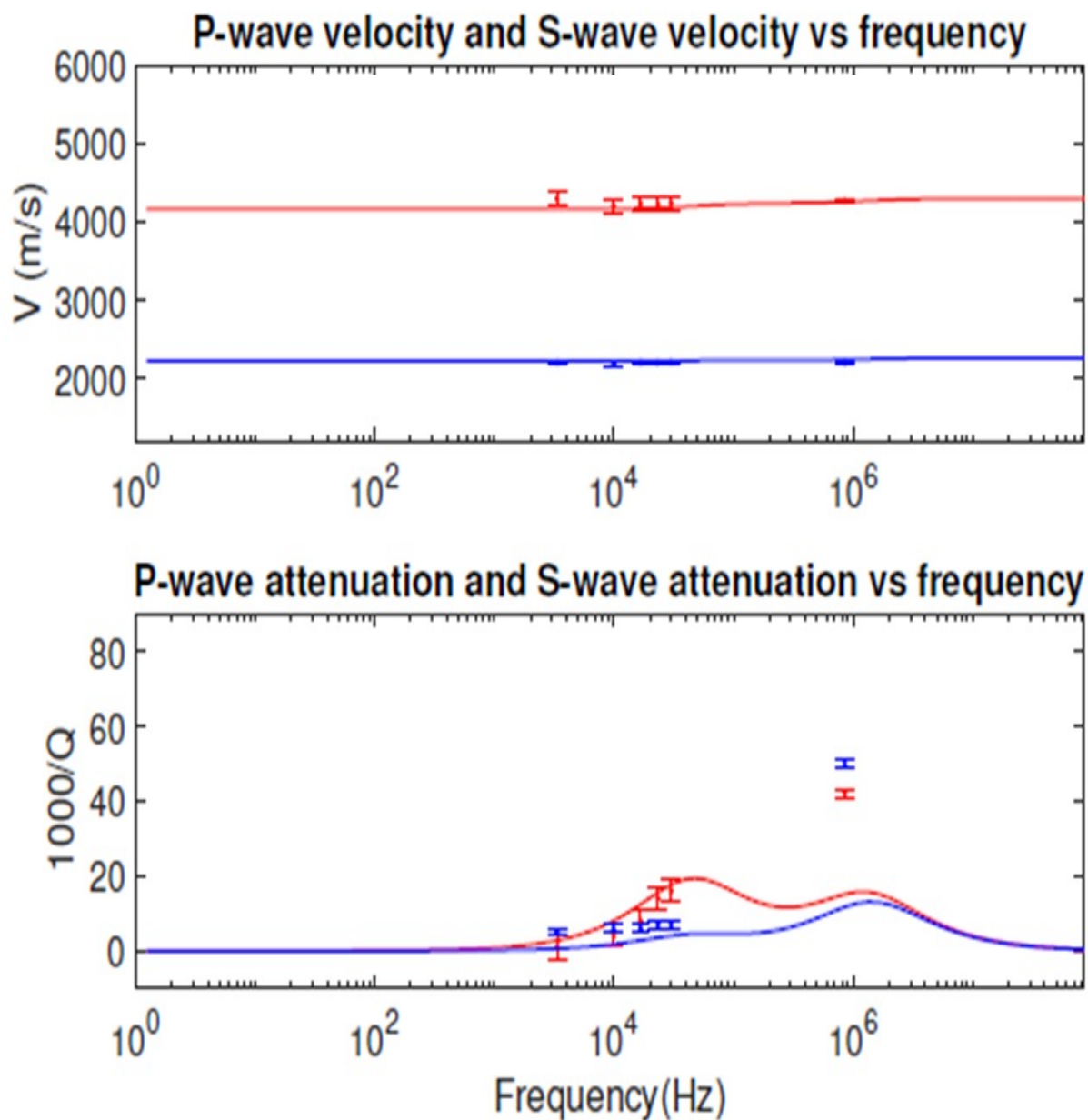


Figure 3.19: The inverted model of three sets of pores. Synthetic data are plotted as dots in the middle of the errorbars, red (p-wave), blue (S-wave). The errorbars, red (p-wave), blue (S-wave) represent the probability distribution, with the median data value in the middle of it. for the model parameters see Table 3.8.

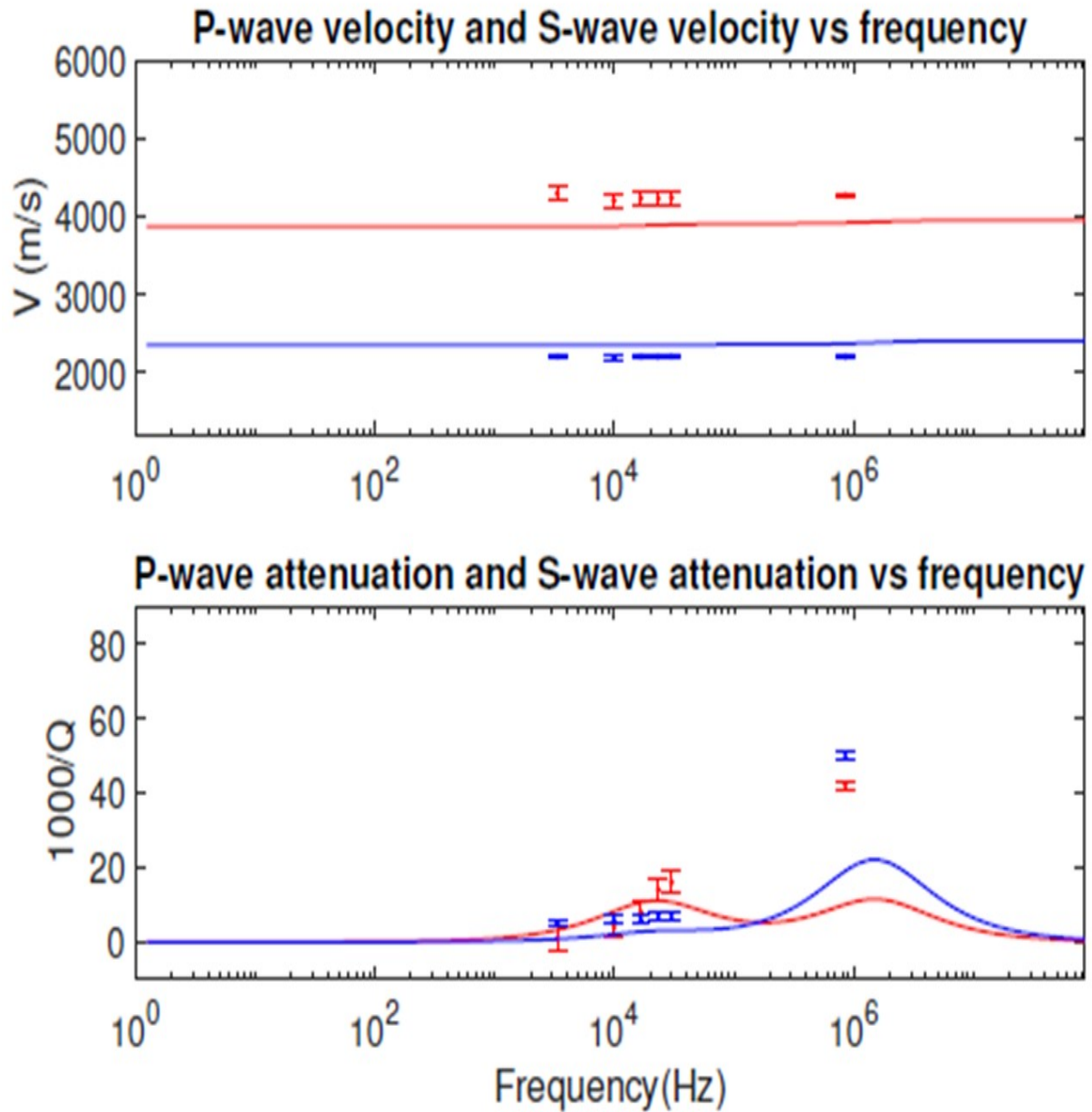


Figure 3.20: The inverted model of three sets of pores. Synthetic data are plotted as dots in the middle of the errorbars, red (p-wave), blue (S-wave). The errorbars, red (p-wave), blue (S-wave) represent the probability distribution, with the median data value in the middle of it, for the model parameters see Table 3.9.

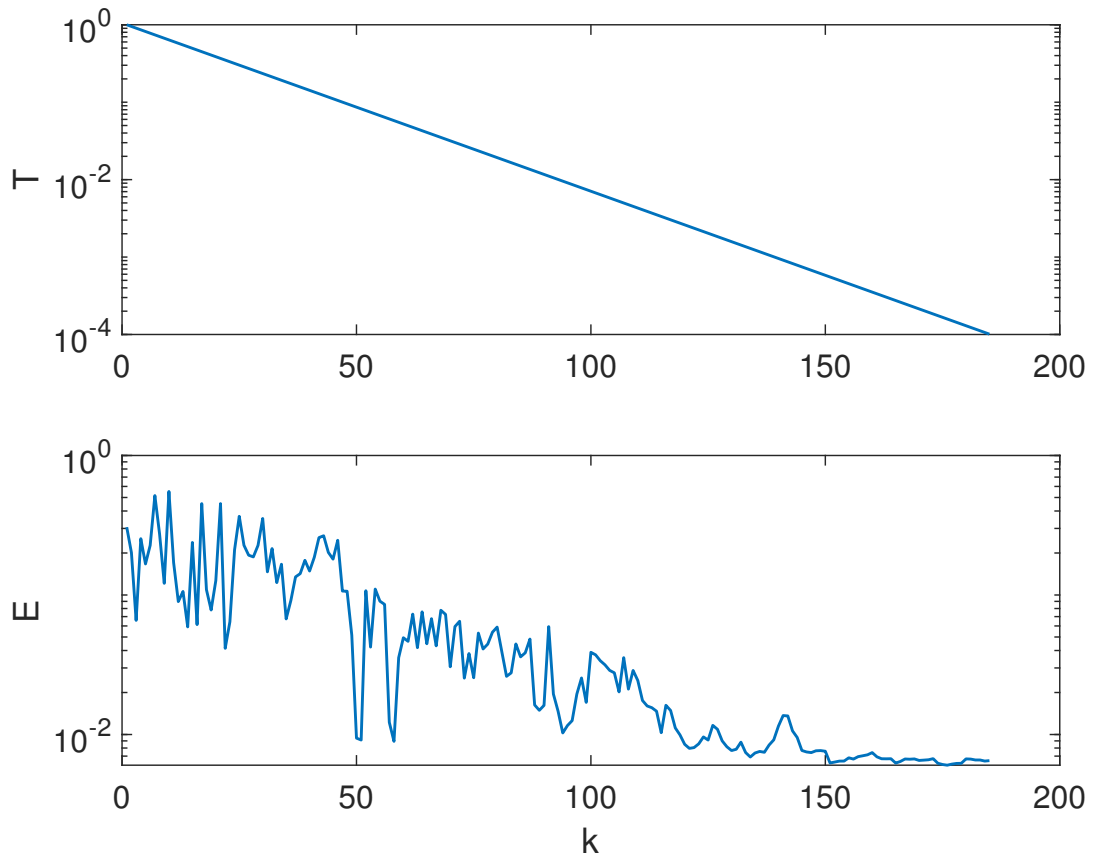


Figure 3.21: Illustration of the number of iterations needed by VFSA, the behaviour of the objective function, and cooling process (temperature curve) for the model in [Figure 3.20](#) above.

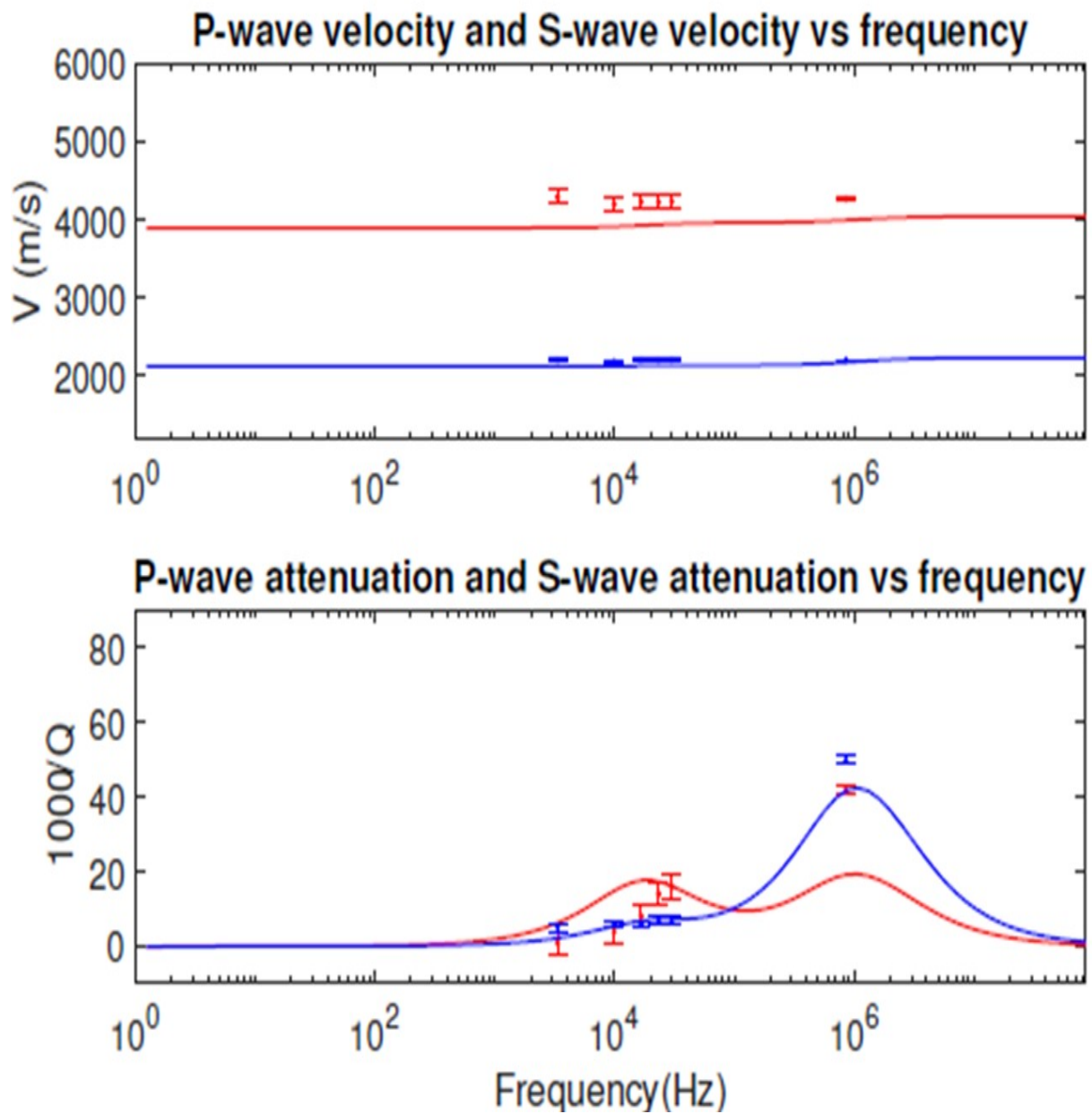


Figure 3.22: Inversion for only attenuation of the Portland limestone (top), using four different sets of pores. Synthetic data are plotted as dots in the middle of the errorbars, red (p-wave), blue (S-wave). The errorbars, red (observed p-wave), blue (observed S-wave), represent the probability distribution, with the median data value in the middle of it, for the model parameters see Table 3.10.

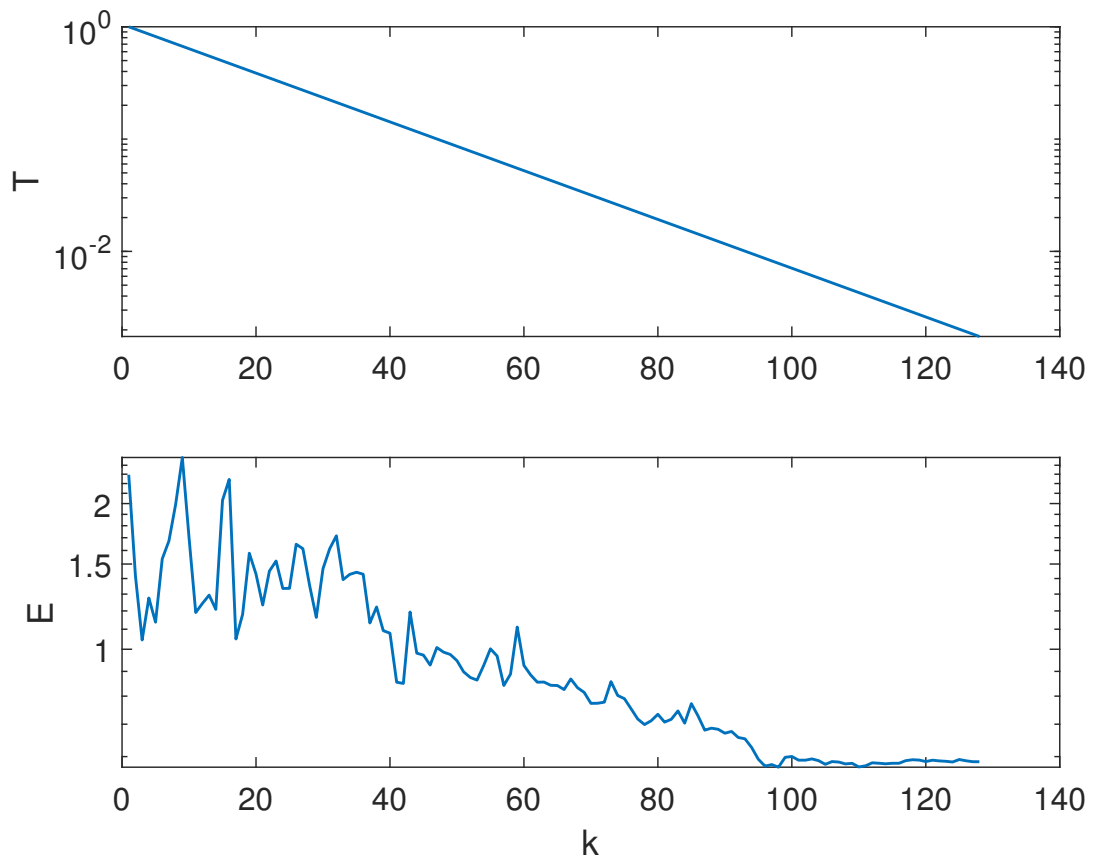


Figure 3.23: Illustration of the number of iterations needed by VFSA, the behaviour of the objective function, and cooling process (temperature curve) for the model in [Figure 3.22](#) above.

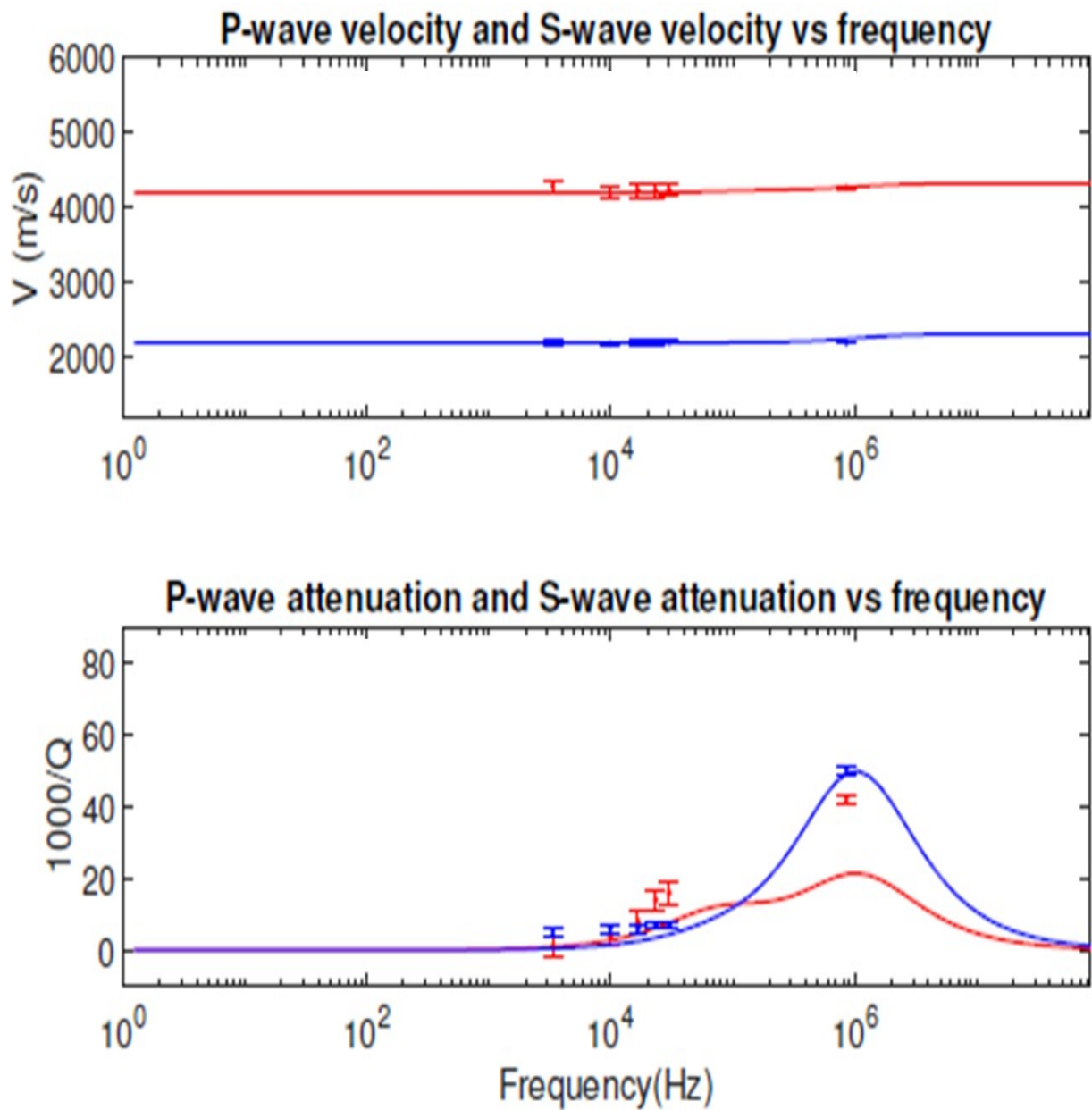


Figure 3.24: The L1-norm inverted model for the Portland limestone (top). using four different sets of pores. Synthetic data are plotted as dots in the middle of the errorbars, red (p-wave), blue (S-wave). The errorbars, red (observed p-wave), blue (observed S-wave), represent the probability distribution, with the middle data value in the middle of it, for the model parameters see Table 3.10.

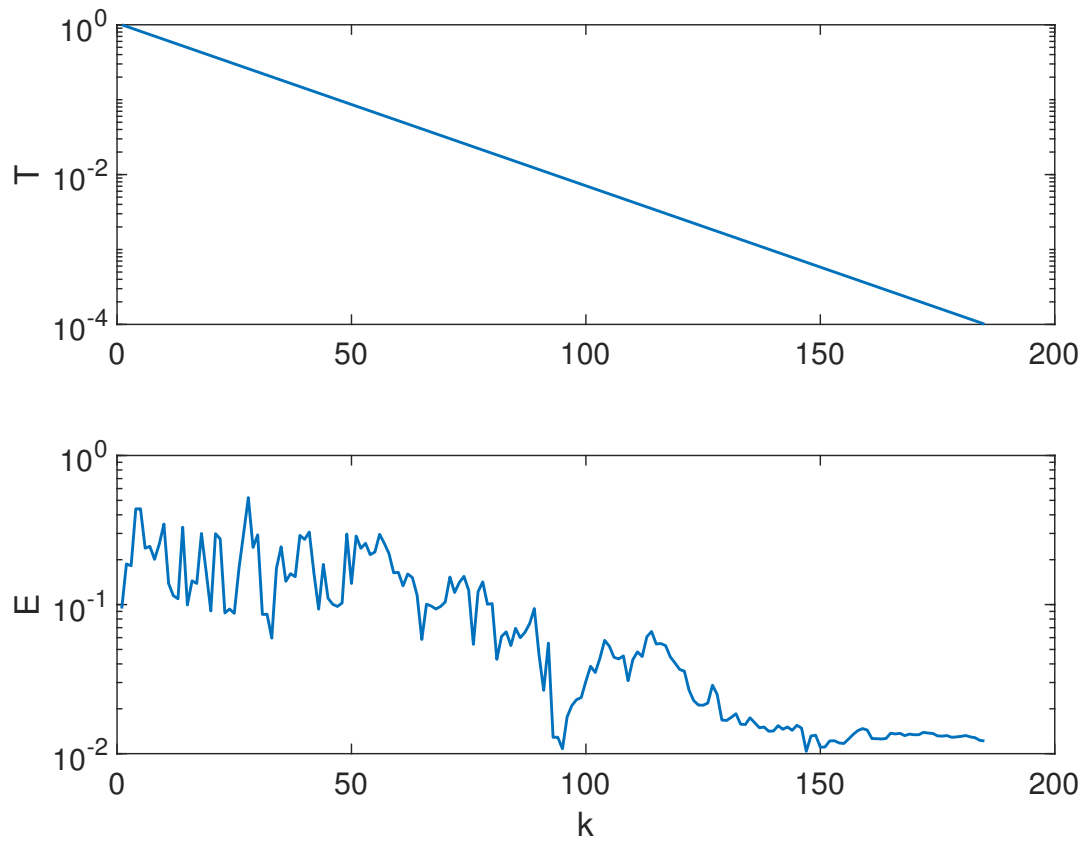


Figure 3.25: Illustration of the number of iterations needed by VFSA, the behaviour of the objective function, and cooling process (temperature curve) for the model in Figure 3.24 above.

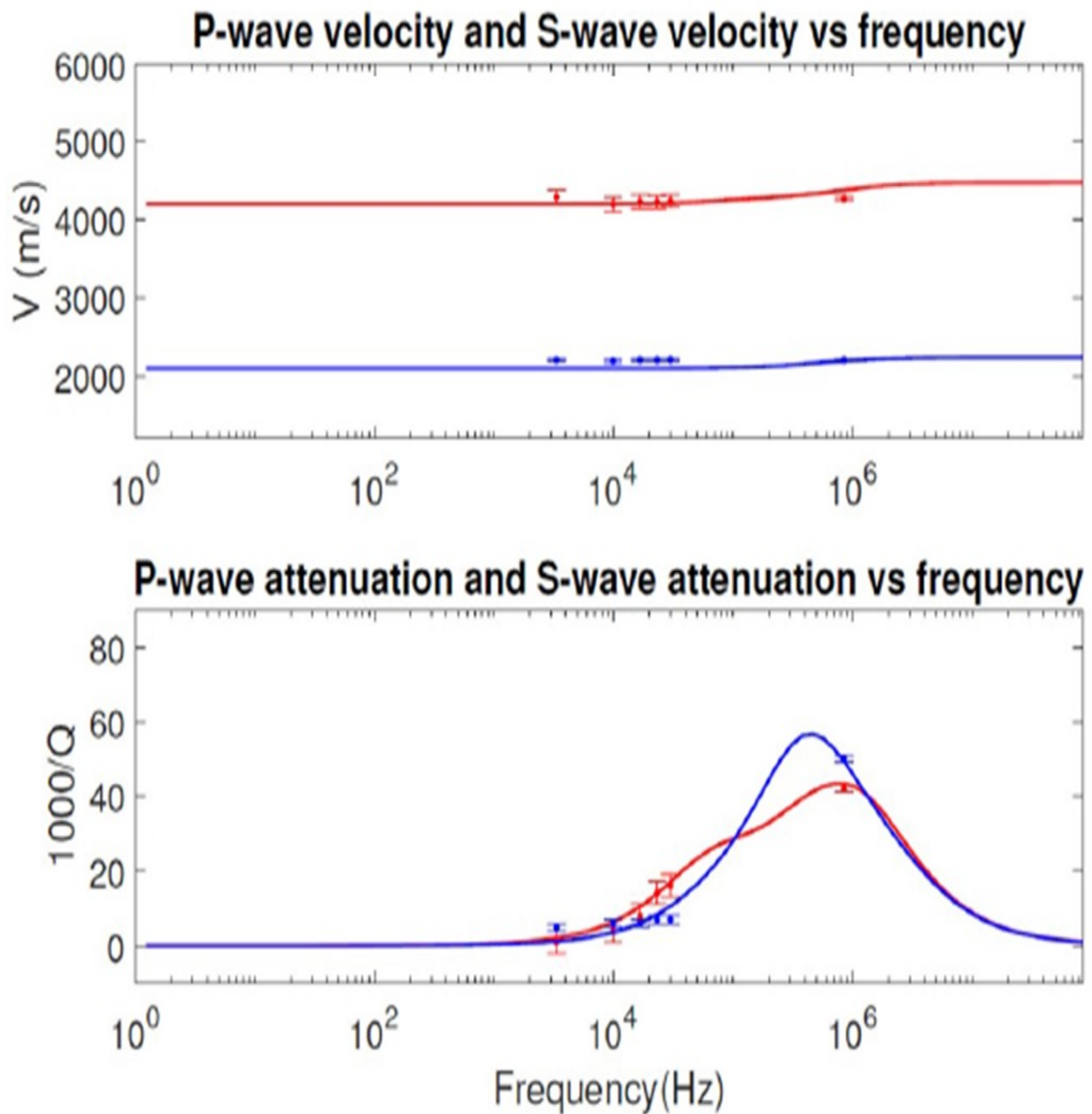


Figure 3.26: The L2-norm inverted model for the Portland limestone (top). using four different sets of pores. Synthetic data are plotted as dots in the middle of the errorbars, red (p-wave), blue (S-wave). The errorbars, red (observed p-wave), blue (observed S-wave), represent the probability distribution, with the middle data value in the middle of it, for the model parameters see Table 3.10.

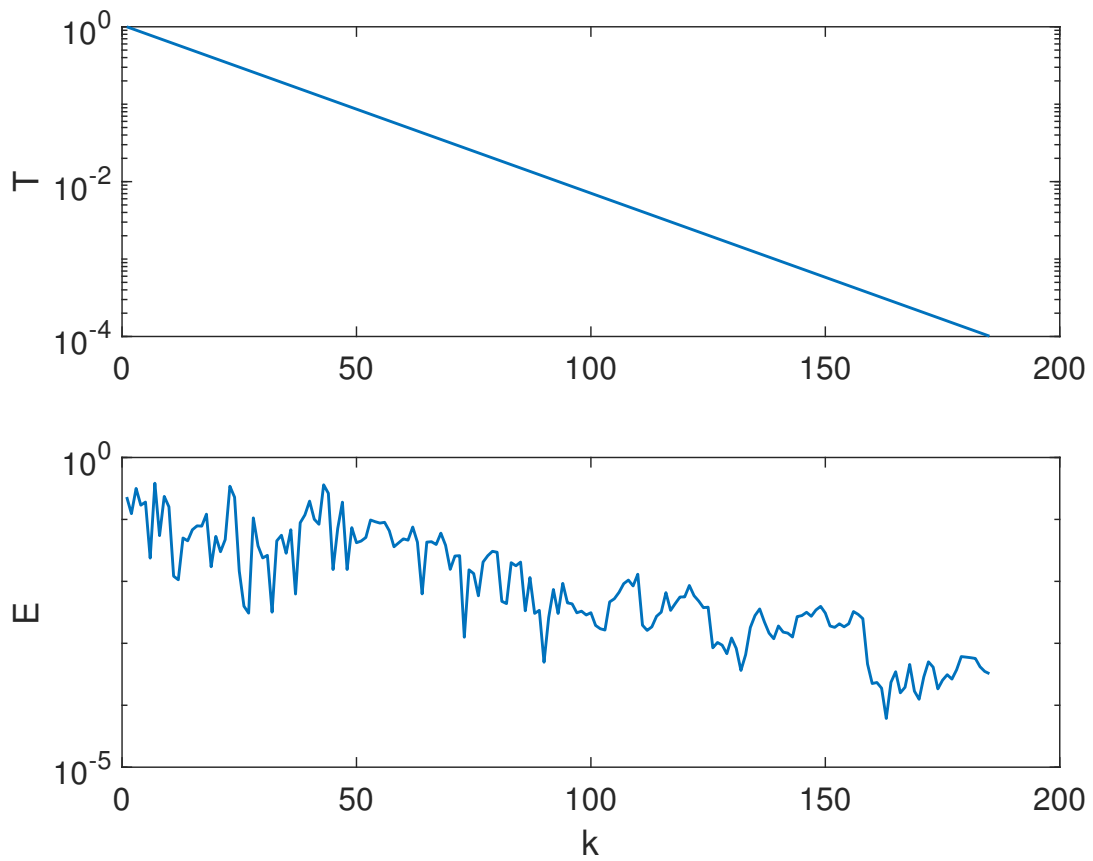


Figure 3.27: Illustration of the number of iterations needed by VFSA, the behaviour of the objective function, and cooling process (temperature curve) for the model in [Figure 3.23](#) above.

Chapter 4

Discussion, Conclusions and Suggestions for Future Work

4.1 Discussion

The main goal of this thesis was to develop a microstructural visco-elastic model that can explain the measured velocity and attenuations of P- and S-waves at sonic and ultrasonic frequencies. An important task was to investigate if it could be possible to obtain a satisfactory match between theory and experiment by using a simpler model with two and three different pore-types. The effect of visco-elastic and microstructural parameters on the measured seismic velocities as well as their effect on the attenuation of the propagating seismic waves, especially carbonate rocks, has been discussed. Throughout this thesis, the theoretical background for visco-elastic model and mechanism of squirt fluid flow, has been explained. Furthermore a beneficial and important sensitivity study, of the microstructural parameters is presented. This sensitivity study and the results from the modelling in Chapter 2, has been effectively employed in later synthetic and real data experiments discussions, in Chapter 3.

Several numerical experiment have been carried out, first, inversion of the theoretically predicted data for the model of two pore-type was performed , Section 3.3.1. Next, for the model with three pore-types, 3.3.2. The results from the synthetic inversion, in Section ?? show sufficiently match with theoritically predicted data. For example, the results of the model with two pore-types, organized in Table 3.1, and Figure 3.3 show an adequate match to the true model, shown in Figure 3.1, opposed to inversion of the real data in Section 3.4.1, nevertheless VFSA shows the ability to give the best-fitting model parameters, which are much closer to the true model than the initial model. VFSA has shown the ability to invert the model with three pore-type in a reliable way. Since the

synthetic inversion give a good match it was clear to test the models and evaluate them with different noise. In the process of finding the optimal match between the theoretical predictions and experimental measurements, applying VFSA, using the visco-elastic T-matrix approach, a non-linear RPI to the microstructural parameters is performed, this time with noise, an elegant inversion and best fitting parameters of the microstructures has been obtained. From the inversion of model with noise, shown in Figure 3.5 and the best-fitting parameters in Table 3.2, one can notice that noise effect is relatively little. Nevertheless, the ME estimation, as has been shown in Figure 3.9, give an important understanding of the unreliability of the simplified models can be extracted. The result has been obtained shows the inconsistency and how big the error can become when using such very simplified model in the inverse problems, it could, typically, when the models from sandstone have been used for carbonates and the related complex media.

Next, real data inversion was performed, starting with model of two different-type, then with three. As a conclusion, one can note that the results obtained by the real data inversion, for models with two, shown in Figure 3.15, and three, shown in Figure 3.19, pore-types, are somewhat far from the observed data, and need a lot of improvement.

Looking at the results from L1- norm, shown in Figure 3.24, L2-norm, shown in Figure ??, and The best-fitting model parameters shown in Table 3.10. The Vs attenuation gives a good match at the ultrasonic frequency, ignoring for a moment the slight under-prediction of observed data at sonic frequency. However, the Vp attenuation has shown a big miss-match at the ultra sonic frequency, while it under-predicts the observed data highly at sonic frequency. The L2-norm give much preferable results that L1-norm, using with coefficients have been selected in this work. Ultimately, a quite good much have been obtained by inversion of both velocity and attenuation, using L2-norm,. However, VFSA slightly over-predict the measured P-wave velocity at the ultrasonic frequency and the S-wave velocity at the sonic frequency.

4.2 Conclusions

To obtain the optimum developing microstructural models for carbonates, several techniques both by synthetic inversion and real data inversion, has been presented. During synthetic inversion, methods, such as ME evaluation and uncertainty estimation, has been investigated to obtain the optimal understanding of the complexity associated with carbonates, more specifically with the limestone (top) sample, which have been studied in this work. The result has been obtained by ME estimation could be used in the evaluation of inconsistency, and how significant the error can become when using such very simplified model in the inverse problems.

From comparison between result of L1-norm and L2-norm, it can be concluded that The L2-norm gives much preferable results than L1-norm, using with coefficients have been selected in this work.

An evaluation of the microstructural models with two and three pore-types have been presented, the match to the real data increases with the increase in the pore-type, in other word, the model with three pore-types gives in general beter match to the real data than the model with two pore-types. After all, the ultimate goal to obtain reliable match to the real data could not be acheived, in the work has been perform.

The real data inversion of the Portland top, using four different pore-types, shown in Figure ??, showed the ability of VFSA to give a sufficient rock physics inversion result, that explain the real data, nevertheless, that it can provide us with a quit good much of the real data model.

4.3 Suggestions for Future Work

Following [Jakobsen et al. \(2021\)](#), in this thesis the effects of global flow is ignored and only the effects of squirt flow is modelled. It is somewhat not very clear if the global flow effects can simply be negligible in the rock sample considered in this work. However, the effects of global flow assumed to be negligible, mainly because the global flow estimation in the visco-elastic T-matrix approach, used in this thesis, is not complete and reliable ([Jakobsen and Chapman, 2009](#); [Jakobsen et al., 2021](#)). Since the fluid substitution is presented in this work, the ide of inverting while fluid substitution is taking place(inversion with the wrong fluid), could have been beneficial. An inversion with the wrong fluid was performed in some of the experiments, carred out, however the results was not included, mainly because of the time limit of doing enough number of experiments. In addition to the fact that the implementation of such inversion, may requires some new assumption or selection of other types of coefficients, or it require some modifications on the VFSA algorithm, currently being used. After all, this could not be possibly done, in this thesis. To an ultimate understanding of the implications of these kind of inversion, future research could be address it properly. Some other suggestions for future research, could be to address the following:

- The effects of global flow relative to the squirt flow, for the the visco- elastic complex porous media, more specifically carbonates.
- Effect of stress and pore fluid pressure

- Applications of calibrated microstructural visco-elastic models within the context of seismic reservoir characterization and/or monitoring
- The microstructural visco-elastic models and the inversion algorithm can be extended to anisotropic visco-elastic media.

Appendices

A The G-tensor

Assuming a reference compliance ($1/\mathbf{C}^{(0)}$) tensor of $\mathbf{S}^{(0)}$, the G-tensor of phase r, $\mathbf{G}^{(r)}$ is given by (Jakobsen and Chapman, 2009; Jakobsen and Johansen, 2005; Torquato and Haslach Jr, 2002)

$$\mathbf{G}^{(r)} = -\mathbf{S}^{(r)} : \mathbf{S}^{(0)}, \quad (\text{A.1})$$

where $\mathbf{S}^{(r)}$ is the compliance Eshelby tensor of the ellipsoid. For the isotropic matrix material containing spheroidal inclusions with semiaxes $a_1^{(r)}=a_2^{(r)}=a_r^{(r)}$ and $a_3^{(r)}=b_r$ and whose symmetry axis is aligned in the x3-direction, the elliptical integrals can be evaluated analytically (Jakobsen et al., 2003a; Jakobsen and Johansen, 2005), and the components of compliance tensor, $S_{ijkl}^{(r)}$, are given by (Jakobsen and Johansen, 2005; Torquato and Haslach Jr, 2002)

$$S_{1111}^{(r)} = S_{2222}^{(r)} = \frac{3}{8(1-\nu)} \frac{a_r^2}{\alpha_r^2 - 1} + \frac{1}{4(1-\nu)} \times \left[1 - 2\nu - \frac{9}{4(\alpha_r^2 - 1)} \right] q, \quad (\text{A.2})$$

$$S_{3333}^{(r)} = \frac{1}{2(1-\nu)} \left\{ 1 - 2\nu + \frac{3\alpha_r^2 - 1}{\alpha_r^2 - 1} - \left[1 - 2\nu - \frac{3\alpha_r^2}{\alpha_r^2 - 1} \right] q \right\}, \quad (\text{A.3})$$

$$S_{1122}^{(r)} = S_{1122}^{(r)} = \frac{1}{4(1-\nu)} \left\{ \frac{\alpha_r^2}{2(\alpha_r^2 - 1)} - \left[1 - 2\nu - \frac{3}{4(\alpha_r^2 - 1)} \right] q \right\}, \quad (\text{A.4})$$

$$S_{1133}^{(r)} = S_{2233}^{(r)} = \frac{1}{2(1-\nu)} \left\{ \frac{-\alpha_r^2}{\alpha_r^2 - 1} - 0.5 \left[(1 - 2\nu) - \frac{3\alpha_r^2}{\alpha_r^2 - 1} \right] q \right\}, \quad (\text{A.5})$$

$$S_{3311}^{(r)} = S_{3322}^{(r)} = \frac{1}{2(1-\nu)} \left\{ 2\nu - 1 - \frac{1}{\alpha_r^2 - 1} - \left[1 - 2\nu - \frac{3}{2(\alpha_r^2 - 1)} \right] q \right\}, \quad (\text{A.6})$$

$$S_{1212}^{(r)} = \frac{1}{4(1-\nu)} \left\{ \frac{\alpha_r^2}{2(\alpha_r^2 - 1)} + \left[1 - 2\nu - \frac{3}{4(\alpha_r^2 - 1)} \right] q \right\}, \quad (\text{A.7})$$

$$S_{1313}^{(r)} = S_{2323}^{(r)} = \frac{1}{4(1-\nu)} \left\{ 1 - 2\nu - \frac{\alpha_r^2 + 1}{\alpha_r^2 - 1} - 0.5 \left[1 - 2\nu - \frac{3(\alpha_r^2 - 1)}{\alpha_r^2 - 1} \right] q \right\}, \quad (\text{A.8})$$

where ν denotes the Poisson ratio of the matrix, given by (Guéguen and Palciauskas, 1994)

$$\nu = \frac{3k - 2\mu}{2(3k + \mu)}, \quad (\text{A.9})$$

where k and μ are the bulk and shear moduli, respectively, of the isotropic matrix, and

$\alpha_r = b_r/a_r$ is the aspect ratio of the r th spheroid, and the constant q is given by

$$q = \frac{\alpha_r}{(1 - \alpha_r^2)^{3/2}} \left[\cos^{-1} \alpha_r - \alpha_r (1 - \alpha_r^2)^{1/2} \right], \quad (\text{A.10})$$

When $\alpha_r \leq 1$. For spheres ($\alpha_r = 1$, $q = 2/3$) the above equations can be simplified to give the compliance tensor as (Jakobsen and Johansen, 2005)

$$S_{ijkl}^{(r)} = \frac{5\nu - 1}{15(1 - \nu)} \delta_{ij} \delta_{kl} + \frac{4 - 5\nu}{15(1 - \nu)} (\delta_{ik} \delta_{jl} + \delta_{il} \delta_{jk}), \quad (\text{A.11})$$

where δ_{ij} denotes the Kronecker-delta, defined by

$$\delta_{ij} = \begin{cases} 0, & \text{if } i \neq j \\ 1, & \text{if } i = j \end{cases}. \quad (\text{A.12})$$

In the case of typical flat compliant Hudson-crack (defined with $\alpha_r \rightarrow 0$ and $q \rightarrow 0$), then the only non-zero components of the compliance tensors are given by (Jakobsen and Johansen, 2005)

$$S_{3333}^{(r)} = 1, \quad (\text{A.13})$$

$$S_{3311}^{(r)} = S_{3322}^{(r)} = \frac{\nu}{1 - \nu}, \quad (\text{A.14})$$

$$S_{1313}^{(r)} = S_{2323}^{(r)} = 0.5. \quad (\text{A.15})$$

B Orientation averaging

In this thesis an isotropic model is assumed, by taking the orientation average of the randomly oriented communicating cavities and the quasi continuous limit is considered, since it can provide an adequate theoretical platform when dealing with real rocks characterized by a discrete spectrum of cavity aspect ratios (Jakobsen et al., 2003b). Following Jakobsen et al. (2003b), a continuous spectrum of cavity orientations but a discrete spectrum of cavity aspect ratios or shape factors is assumed to perform the orientation averaging. The population of cavities is re-divided into new sets of cavities, each set labelled by $i=1, \dots, I$ and characterized by an orientation distribution function $O^i(\Omega)$, common aspect ratio α^i , and porosity ϕ^i , with all these assumptions been given the following formulas is introduced

$$\sum_{r=1}^N v^{(r)} \mathbf{A}^{(r)} \longrightarrow \sum_{i=1}^I \phi^{(i)} \mathbf{A}^{(i)} \quad (\text{B.1})$$

$$\bar{\mathbf{A}}^{(i)} = \int d\Omega O(\Omega) A(a^{(i)}, \Omega), \quad (\text{B.2})$$

where $\bar{\mathbf{A}}^{(i)}$ is the orientation average of $A(a^{(i)}, \Omega)$, $\mathbf{A}^{(r)}$ is a tensorial quantity (depends on the orientation/shape index r), Ω symbolizes the three Euler angles that determine the orientation of the cavity relative to the crystallographic axes of the material with reference stiffness tensor $\mathbf{C}^{(0)}$. [Jakobsen et al. \(2003b\)](#) give some formulas for orientation averaging in the special case of a vertical transversely isotropic medium, which are relevant for isotropic media. For details about implementing the formulas above for the general case with arbitrary orientation distribution functions, see [Jakobsen et al. \(2003b\)](#).

Bibliography

- Adam, L., Batzle, M., Lewallen, K., and van Wijk, K. (2009). Seismic wave attenuation in carbonates. *Journal of Geophysical Research: Solid Earth*, 114(B6).
- Agersborg, R., Jakobsen, M., Ruud, B., and Johansen, T. (2007). Effects of pore fluid pressure on the seismic response of a fractured carbonate reservoir. *Studia Geophysica et Geodaetica*, 51(1):89–118.
- Agersborg, R., Johansen, T. A., and Jakobsen, M. (2009). Velocity variations in carbonate rocks due to dual porosity and wave-induced fluid flow. *Geophysical prospecting*, 57(1):81–98.
- Agersborg, R., Johansen, T. A., Jakobsen, M., Sothcott, J., and Best, A. (2008). Effects of fluids and dual-pore systems on pressure-dependent velocities and attenuations in carbonates. *Geophysics*, 73(5):N35–N47.
- Assefa, S., McCann, C., and Sothcott, J. (1999). Attenuation of p-and s-waves in limestones. *Geophysical Prospecting*, 47(3):359–392.
- Aster, R. C., Borchers, B., and Thurber, C. H. (2018). *Parameter estimation and inverse problems*. Elsevier.
- Auld, B. (1990). *Acoustic fields and waves in solids*, robert e.
- Batzle, M. and Wang, Z. (1992). Seismic properties of pore fluids. *Geophysics*, 57(11):1396–1408.
- Biot, M. A. (1956a). Theory of propagation of elastic waves in a fluid-saturated porous solid. i. higher frequency range. *The Journal of the acoustical Society of america*, 28(2):168–178.
- Biot, M. A. (1956b). Theory of propagation of elastic waves in a fluid-saturated porous solid. ii. higher frequency range. *The Journal of the acoustical Society of america*, 28(2):179–191.

- Dellinger, J., Vasicek, D., and Sondergeld, C. (1998). Kelvin notation for stabilizing elastic-constant inversion. *Revue de l'Institut Français du Pétrole*, 53(5):709–719.
- Eberli, G. P., Baechle, G. T., Anselmetti, F. S., and Incze, M. L. (2003). Factors controlling elastic properties in carbonate sediments and rocks. *The Leading Edge*, 22(7):654–660.
- Guéguen, Y. and Palciauskas, V. (1994). *Introduction to the Physics of Rocks*. Princeton University Press.
- Gurevich, B., Makarynska, D., de Paula, O. B., and Pervukhina, M. (2010). A simple model for squirt-flow dispersion and attenuation in fluid-saturated granular rocks. *Geophysics*, 75(6):N109–N120.
- Ingber, L. (1989). Very fast simulated re-annealing. *Mathematical and computer modelling*, 12(8):967–973.
- Ingber, L. (1993). Simulated annealing: Practice versus theory. *Mathematical and computer modelling*, 18(11):29–57.
- Izumotani, S. and Onozuka, S. (2013). Elastic moduli and the aspect ratio spectrum of rock using simulated annealing. *Geophysical Prospecting*, 61:489–504.
- Jakobsen, M. (2004). The interacting inclusion model of wave-induced fluid flow. *Geophysical Journal International*, 158(3):1168–1176.
- Jakobsen, M. and Chapman, M. (2009). Unified theory of global flow and squirt flow in cracked porous media. *Geophysics*, 74(2):WA65–WA76.
- Jakobsen, M. and Hudson, J. A. (2003). Visco-elastic waves in rock-like composites. *Studia Geophysica et Geodaetica*, 47(4):793–826.
- Jakobsen, M., Hudson, J. A., and Johansen, T. A. (2003a). T-matrix approach to shale acoustics. *Geophysical Journal International*, 154(2):533–558.
- Jakobsen, M. and Johansen, T. A. (2005). The effects of drained and undrained loading on visco-elastic waves in rock-like composites. *International Journal of Solids and Structures*, 42(5-6):1597–1611.
- Jakobsen, M., Johansen, T. A., and McCann, C. (2003b). The acoustic signature of fluid flow in complex porous media. *Journal of applied Geophysics*, 54(3-4):219–246.
- Jakobsen, M., McCann, C., and Sothcott, J. (2019). Carbonate microstructures from measured velocity and attenuation spectra via simulated annealing. In *SEG Technical Program Expanded Abstracts 2019*, pages 3648–3652. Society of Exploration Geophysicists.

- Jakobsen, M., McCann, C., and Sothcott, J. (2021). Microstructures of carbonate rocks from velocity and attenuation data at sonic and ultrasonic frequencies. *submitted*.
- Kirkpatrick, S., Gelatt, C. D., and Vecchi, M. P. (1983). Optimization by simulated annealing. *science*, 220(4598):671–680.
- Klimentos, T. and McCann, C. (1990). Relationships among compressional wave attenuation, porosity, clay content, and permeability in sandstones. *Geophysics*, 55(8):998–1014.
- Li, B., Shen, H., Qu, S., Wang, D., and Liu, C. (2018). Tight carbonate reservoir characterization based on the modified rock physics model. *Journal of Applied Geophysics*, 159:374–385.
- McCann, C. and Sothcott, J. (1992). Laboratory measurements of the seismic properties of sedimentary rocks. *Geological Society, London, Special Publications*, 65(1):285–297.
- McCann, C. and Sothcott, J. (2009). Sonic to ultrasonic q of sandstones and limestones: Laboratory measurements at in situ pressures. *Geophysics*, 74(2):WA93–WA101.
- Metropolis, N., Rosenbluth, A. W., Rosenbluth, M. N., Teller, A. H., and Teller, E. (1953). Equation of state calculations by fast computing machines. *The journal of chemical physics*, 21(6):1087–1092.
- O’Hara, S. G. (1985). Influence of pressure, temperature, and pore fluid on the frequency-dependent attenuation of elastic waves in berea sandstone. *Physical Review A*, 32(1):472.
- Saberi, M. R. (2010). An integrated approach for seismic characterization of carbonates.
- Sen, M. K. and Stoffa, P. L. (2013). *Global optimization methods in geophysical inversion*. Cambridge University Press.
- Siqueira, T. A., Iglesias, R. S., and Ketzer, J. M. (2017). Carbon dioxide injection in carbonate reservoirs—a review of co₂-water-rock interaction studies. *Greenhouse Gases: Science and Technology*, 7(5):802–816.
- Tarantola, A. (2005). *Inverse problem theory and methods for model parameter estimation*. SIAM.
- Torquato, S. and Haslach Jr, H. (2002). Random heterogeneous materials: microstructure and macroscopic properties. *Appl. Mech. Rev.*, 55(4):B62–B63.
- Xu, S. and White, R. E. (1995). A new velocity model for clay – sand mixtures 96, 1-23. *Geophys. Prospect*, 43:91–118.